

POLITECNICO DI TORINO

**MASTER'S DEGREE in MECHANICAL
ENGINEERING**



MASTER'S DEGREE THESIS

**Uncertainty analysis of variable stiffness
laminates**

Supervisors

Prof. ALFONSO PAGANI

Prof. ALBERTO RACIONERO

Prof. MARCO PETROLO

Candidate

IGNACIO SÁNCHEZ ZÁRATE

APRIL 2021

Summary

Variable stiffness composites are fiber reinforced components manufactured by means of automated fiber placement technique. The fiber orientation angle varies within the tow path, providing the variable stiffness properties of the manufactured components. These non-conventional parts have shown better mechanical properties per unit-weight than many conventionally manufactured components. However, its fabrication process is subjected to imperfections which are prone to generate defects and undesired variability in the parts, decreasing the mechanical performance of the components. In order to avoid material waste or the application of very large safety coefficients, it is of great importance to understand the effect of manufacturing induced defects and uncertainty in variable stiffness composites.

In this work, a multi-scale sensitivity analysis is performed, in which the buckling performance at a macro-scale level is studied for composite plates affected by uncertainty effects at a micro-scale level. For the study, the macro and micro-stress fields are obtained for the static solution of two variable stiffness composites. Finite element models and theories within the Carrera Unified Formulation framework are employed in the investigation. A layer-wise approach is applied in order to model each composite layer separately, introducing uncertainty effects in the ply level, at the meso-scale.

Stochastic fields are generated to introduce variability into the fiber volume fraction at the micro-scale. This parameter affects the material properties assigned to the finite element mesh elements and are obtained from the unit cell problem resolution applying the mechanics of structure genome.

The sensitivity study is performed via Monte Carlo analyses, carrying out many deterministic linearized buckling simulations in which the fiber volume fraction value within the plies is defined by a different random field. Distribution plots of the buckling analysis outputs are obtained and statistical indicators are calculated. At the conclusion of the analysis, polynomial chaos expansion models are proposed as a time saving alternative to the full Monte Carlo analysis.

Acknowledgements

I would like to express my gratitude to Alberto Racionero for his guidance during the elaboration of this work. This could not be possible without his support. I would also like to express my gratitude to prof Alfonso Pagani and Marco Petrolo for all their mentoring during the development of this dissertation.

Particular and sincere thanks to Michele Delicata for his kind advice and for introducing MUL2 to me.

My last thought is to my family and to those who have accompanied me during my stay in Torino.

“A mi familia, el mayor regalo que Dios me ha hecho”

Table of Contents

List of Tables	VIII
List of Figures	IX
Acronyms	XIII
1 Introduction	1
1.1 Automated fiber placement technique	1
1.2 Manufacturing defects	2
1.3 Variable stiffness composites	5
1.4 Models for macro-mechanical analysis of VSC	6
1.5 Micro-scale modeling	7
1.6 Uncertainty on VSC	8
1.7 Contents of this dissertation	9
2 Layer-wise models of laminated VAT panels	11
2.1 Carrera Unified Formulation	11
2.1.1 Taylor Expansion	12
2.1.2 Lagrange Expansion	12
2.1.3 Hierarchical Legendre Expansion	13
2.2 Finite element approximation	15
2.2.1 Constitutive equations for VSC	15
2.2.2 Finite Element Formulation	18
2.2.3 Principle of virtual displacements	19
2.2.4 Static analysis	21
2.2.5 Linearized buckling analysis	21
2.3 ESL vs LW modeling techniques	22
3 Micro-mechanics	25
3.1 Unit Cells	25
3.2 Variational Asymptotic Method	27

3.3	VAM and FE methods	28
3.4	Cross-section mapping	30
3.4.1	First order mapping	31
3.4.2	Second order mapping	31
3.4.3	Blending function method	32
3.5	Equivalent stiffness properties and local field recovery	33
4	Defect uncertainty quantification	34
4.1	Multi-scale Uncertainty Analysis	34
4.2	Modeling uncertainty	35
4.2.1	Random field	36
4.2.2	Karhunen-Loeve Expansion	36
4.2.3	Latin Hypercube Sampling Method	39
4.2.4	Coupling random field and FEM	39
4.3	Monte Carlo analysis for uncertainty quantification	40
4.3.1	Polynomial Chaos Expansion	42
5	Numerical results	44
5.1	Model verification	45
5.1.1	Micro-scale verification	45
5.1.2	Macro-scale verification	47
5.1.3	Mesh convergence analysis	49
5.2	Pristine model analysis	54
5.2.1	Static solution	55
5.2.2	Buckling analysis	60
5.2.3	Micro-scale field recovery	63
5.3	Uncertainty Analysis	66
5.3.1	Material regression functions	66
5.3.2	Problem definition	68
5.3.3	Stress and strain fields	69
5.3.4	Buckling critical loads	74
5.3.5	Mode classification	77
5.3.6	Buckling Loads Correlation	78
5.3.7	Polynomial chaos expansion	82
6	Conclusions	86
	Bibliography	88

List of Tables

2.1	Taylor expansion polynomial terms	12
4.1	Askey scheme relating random variable distributions with its correspondent polynomial family for PCE. Extracted from [37]	43
5.1	Material properties of the fiber and the epoxy matrix, extracted from the example in [32]	46
5.2	Equivalent material properties for the homogenized UC	46
5.3	Geometrical properties of the VSC plate	47
5.4	F_{cr1} values obtained by Abaqus and with the LW and ESL models .	48
5.5	DOF and elapsed time of the performed buckling simulations in the mesh convergence analysis	53
5.6	Final mesh for the VSC model	54
5.7	F_{cr_i} of the pristine model of VSC A	60
5.8	F_{cr_i} of the pristine model of VSC B	61
5.9	Static solution strain field in point C, in the fiber local reference system, for VSCs A and B	63
5.10	Mean value and standard deviation (in parenthesis) for the stress field values along line s	69
5.11	Monte Carlo analysis results for VSC A	74
5.12	Monte Carlo analysis results for VSC B	74
5.13	Correlation coefficients in relation to F_{cr1}	80
5.14	PCE statistical data for VSC A	82
5.15	PCE statistical data for VSC B	82
5.16	Qualitative computational times	85

List of Figures

1.1	Gaps and overlaps induced by AFP. Extracted from [2]	3
1.2	A twisted tow on the surface of a ply. Obtained from [2]	3
1.3	Tows affected by wrinkling and unfolding. From [2]	4
1.4	Example of a fiber path definition varying linearly along the characteristic length d . Extracted from [5]	6
2.1	L9 Lagrange Expansion element geometry	13
2.2	Fiber rotation angles	17
2.3	Fiber orientation angle on VAT	18
2.4	B4 (four-node) Lagrange beam element for the longitudinal direction and its shape functions	19
2.5	Equivalent single layer assembly procedure of the stiffness matrix	22
2.6	Layer-wise assembly procedure of the stiffness matrix	23
3.1	Heterogeneous material with periodically repeated cells. Extracted from [25]	26
3.2	Unit cell consisting on a circular transverse-section fiber surrounded by a portion of epoxy matrix	27
3.3	Transformation to the global coordinate system using mapping functions. Extracted from [25]	31
3.4	Actual geometry of the cross-section achieved via BFM. Figure obtained from [25]	33
4.1	Scheme of the multi-scale problem	35
4.2	Stochastic field $\Psi_{FVF}(\alpha, \beta; \omega)$ expanded over a ply using KLE with parameters $(\bar{\Psi}_{FVF}, \sigma) = (0.6, 0.02)$	38
4.3	The stochastic field is sampled on the Gauss integration points and the values are employed for the computation of the FE matrices	40
4.4	Representation of an histogram and PDF of a normal distribution	41
5.1	FVF parameter fully defines the geometry of the UC cross-section	45

5.2	Plate with boundary conditions. F stands for free edge, C for clamped and P corresponds to the $1N$ distributed load	48
5.3	Comparison between the first deformation mode obtained with LW model and TE models for VSC A	49
5.4	Comparison between the first deformation mode obtained with LW model and TE models for VSC B	50
5.5	Convergence of F_{cr_i} when varying the number of B4-elements along the longitudinal dimension of the VSC plate A	51
5.6	F_{cr} convergence analysis varying the quantity of L9-elements in the cross-section of each ply of VSC A	52
5.7	Final mesh with six L9-elements per layer and detail of a B4-element in the longitudinal dimension of the VSC plate	54
5.8	Stress and strain fields are presented along line s	55
5.9	Stress tensor representation along line s for VCS A	56
5.10	Strain tensor representation along line s for VSC A	57
5.11	Stress tensor representation along line s for VCS B	58
5.12	Strain tensor representation along line s for VSC B	59
5.13	Buckling deformation shape modes for VSC A	60
5.14	Buckling deformation shape modes for VSC B	61
5.15	F_{cr} comparison between VSC A and B	62
5.16	The UC under investigation belongs to the top layer of the VSC. It is located in the middle point of the ply.	63
5.17	UC local stress field recovery	64
5.17	UC local stress field recovery	65
5.18	UC homogenized material properties as a function of ψ_{FVF} and polynomial fitting functions	67
5.19	Stochastic fields with $(\bar{\psi}_{FVF}, \sigma) = (0.6, 0.05)$	68
5.20	Stress tensor representation along line s for VSC A	70
5.21	Strain tensor representation along line s for VSC A	71
5.22	Stress tensor representation along line s for VSC B	72
5.23	Strain tensor representation along line s for VSC B	73
5.24	Histograms of the F_{cr} for VSC A	75
5.25	Histograms of the F_{cr} for VSC B	76
5.26	Superposing F_{cr_i} distributions for VSC A	77
5.27	MAC matrices give information about mode swapping	78
5.28	MAC matrix statistical data: mean value and standard deviation for VSC A	79
5.29	MAC matrix statistical data: mean value and standard deviation for VSC B	79
5.30	Uncertainty affecting F_{cr1} and F_{cr2} in the same way (a) and in the opposite way (b). The range limits for both loads are listed in (c)	81

5.31	F_{cr1} distributions obtained from the Monte Carlo analysis and the PCE models	83
5.32	PCE convergence analysis	84
5.33	Time employed to perform all Monte Carlo simulations (1) vs total time for performing 300 simulations and for the PCE calculations (2)	85

Acronyms

AFP

Automated Fiber Placement

BFM

Blending Function Method

CCM

Concentric Cylinder Model

CMD

Covariance Matrix Decomposition

CNC

Computer Numerical Control

COV

Coefficient Of Variation

CUF

Carrera Unified Formulation

CW

Component Wise

DLM

Defect Layer Method

DOF

Degree Of Freedom

ESL

Equivalent Single Layer

FE(M)

Finite Element (Methods)

FN

Fundamental Nuclei

FVF

Fiber Volume Fraction

GMC

Generalized Model of Cells

HFGMC

High-Fidelity Generalized Method of Cells

HLE

Hierarchical Legendre Expansion

KLE

Karhunen-Loeve Expansion

LE

Lagrange Expansion

LHS

Latin Hypercube Sampling

LW

Layer-wise

MAC

Modal Assurance Criterion

MOC

Method Of Cells

MSG
Mechanics of Structure Genome

PCE
Polynomial Chaos Expansion

PDF
Probability Density Functions

PVD
Principle of Virtual Displacements

RDO
Robust Design Optimization

RVE
Representative Volume Element

TE
Taylor Expansion

UC
Unit Cell

VAM
Variational Asymptotic Method

VAT
Variable Angle Tow

VSC
Variable Stiffness Composites

1D
One Dimension

2D
Two Dimension

3D
Three Dimension

Chapter 1

Introduction

1.1 Automated fiber placement technique

Automated fiber placement technique (AFP) is a manufacturing process which makes possible the production of fiber reinforced structures. This composite materials have two identifiable constituents: a fiber reinforcement and a epoxy resin matrix. With this technique it is possible to obtain high strength and stiffness per unit-weight parts, also high quality on both surface finish and part integrity [1]. Its weight-specific properties are great vantage over conventionally used metals, being the reason for which many AFP components are widely implemented in many industries. For example, it is of great interest for Aerospace applications where a reduction on structural weight means less fuel consumption and costs [2]. Fuselage barrels and main wing boxes are some of the parts produced in this sector by AFP [3].

The manufacturing process is normally performed by a CNC machine. A fiber placement head is mounted at the end of a robotic arm that has many degrees of freedom. Material tows, conformed by many fibers impregnated in matrix resin, are heated and then fed into the head. The robotic tool places a bunch of tows, also called a course, following a determined path while at the same time compacts them with a compaction roller. Afterwards, postprocessing operations as cure processes are carried out to obtain the final product [1].

Courses can be composed of up to 32 tows. The AFP machine controls each one of the tows, being able to cut and restart their feeding independently. Complex geometries, even with double curvature surfaces, can be produced by AFP [2]. A complete laminate is constructed by placing multiple courses, one parallel to the other along the surface [3].

Nowadays, the fiber placement technique can be totally automated providing great accuracy, process robustness and speed. The proper automation process leads

to reduced labour time and operational costs. For being economically competitive, it is important to ensure that AFP operation, machine investment and material costs do not exceed the operational costs saved (for example, fuel costs) [2]. Therefore, research is needed to improve and optimize the manufacturing process as it directly has an influence on the final product performance. Part defects emerge due to fabrication and processing constraints, and imply an increase in the labour time and material waste [1]. In the next section, the main defects affecting to the AFP manufactured parts are going to be discussed.

1.2 Manufacturing defects

With AFP it is possible to obtain high quality parts with good repeatability and accuracy. However, this manufacturing process is not exempt from limitations. Process imperfections make the actual manufactured part differ from its design. The mechanical properties of the component could be affected by this process induced defects. A brief explanation of the main issues found in the literature involving AFP are now presented:

- Angle deviation: AFP has the possibility to place fibers following a certain path which can be rectilinear or curvilinear. Normally, guiding curves are used for this. Fiber courses are oriented as such reference curves. When using curvilinear fiber paths, the angle of the course deviates from the reference one. This defect is influenced by the chosen course width. Wider fiber courses imply bigger angle deviation, but the use of narrower ones involve more manufacturing time. Therefore, a balance between quality and time is decided by selecting the proper width.
- Tow misalignment: this defect is caused by position inaccuracy on the robotic arm's deposition head due to inertial effects on the machine structure and process speed.
- Fiber waviness: it can occur both on the laminate plane (in-plane) or within the laminate thickness (out-of-plane). The first one is produced by fiber steering and complex surfaces. The second is influenced by tooling and processing and fiber steering as well. Out-of-plane waviness reduces strength and stiffness of the parts.
- Gaps and overlaps between adjacent tows: this defects are influenced by material process-ability, tow width fluctuations and machine parameters. Gaps and overlaps are most frequent on complex geometries. During fiber steering, a course width adjustment is applied. It can only be done by discrete steps resulting on non-fitting edges between courses. This adjustment follows

a coverage strategy determined by the manufacturer. The percentage of tow overlap on the course boundaries is related to this strategy. A 0% coverage strategy imply that no overlaps happen on the boundary defect areas but only gaps. Coverage percentage ranges from 0 to 100, being each value a combinations between gaps and overlaps. This kind of defects are the most frequent on AFP.

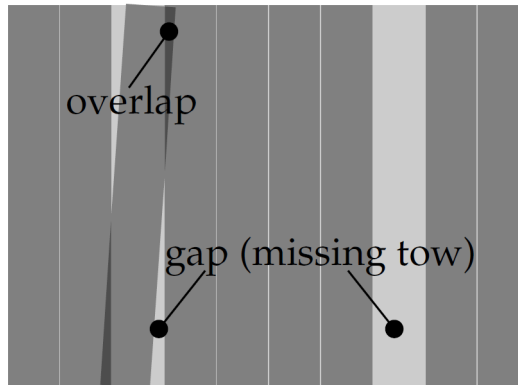


Figure 1.1: Gaps and overlaps induced by AFP. Extracted from [2]

- Twisted tows: it consists of the twist of individual tows on a ply during the fiber placement operation. This issue is not frequent thanks to the implementation of control processes and the use of high quality materials.

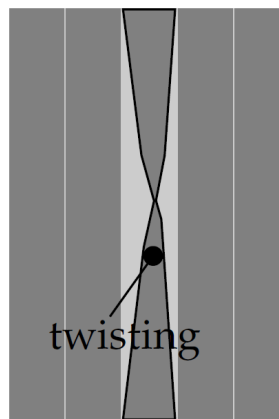


Figure 1.2: A twisted tow on the surface of a ply. Obtained from [2]

- Bridging and crowning: lack of pre-tension within the tows may cause bridging and crowning when manufacturing, respectively, concave and convex complex surfaces.

- Wrinkling and upfolding: these defects are provoked by the absence of adhesion between a tow and the surface underneath. These phenomena are related to tow compressive and tensile stresses during steering. Compressive stress generate wrinkles while tensile stress is responsible for tow upfolding. These kind of defects depend on the minimum turning radius which is related to the material.

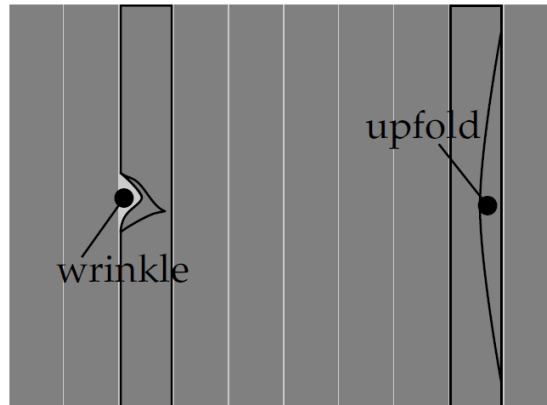


Figure 1.3: Tows affected by wrinkling and upfolding. From [2]

- Voidage and inclusions: the appearance of voids and inclusions are highly related with the quality of the employed material, its temperature conditions and the compaction force applied. Insufficient compaction force leaves a bigger amount of air entrapped inside the ply. Voids arise with the presence of gaps and overlaps. Inclusions are not common in AFP.
- Residual stresses and deformations: induced by the manufacturing process on the component.
- Fuzzballs: fuzz formation due to contact interaction between the machine and the fiber material.

Defects are inevitable during the manufacturing process. Therefore, in order to reduce their negative impact, it is need to investigate how these defects affect to the part properties. Further knowledge on these AFP defects can be found in the review by Heinecke and Willberg [2].

1.3 Variable stiffness composites

An innovative aspect of AFP manufacturing is the ability to produce non-conventional composites with variable stiffness properties. Variable stiffness composites (VSC), also known as Variable Angle Tow (VAT), are obtained placing fibers following a curvilinear path [4]. This design of the fiber stacking procedure within the ply is also known as tailoring [5]. Orienting the fibers in a favorable way positively influences the stress distribution on VSC, obtaining better buckling performance and stiffness properties than conventional composites composed of straight-path fibers [6]. Therefore, the tailoring of the plies is optimized in order to maximize the component performance. Despite many theoretical calculations, not all optimized patterns can be actually produced due to machine limitations as, for example, the minimum turning radius [4].

AFP software defines guiding lines as a reference to define the fiber placement path. VSC are constructed by shifting curvilinear courses perpendicularly to the variation direction of the reference line [3]. For the sake of simplicity, it is common to use a constant curvature line as a reference for the fiber path. In this case, the fiber orientation function is defined taking an arbitrary point A as a reference. Then, the equation of the fiber orientation, obtained from [5], between A and another point B is:

$$\theta(x') = \phi + T_0 + \frac{(T_1 - T_0)}{d} |x'| \quad (1.1)$$

in which $x' = x \cos \phi + y \sin \phi$. T_0 and T_1 indicate the fiber angle orientation at points A and B , respectively. The characteristic length d corresponds to the distance between both points and it is usually defined for square and rectangle plates as half of a side length of the laminate. Angle ϕ specifies a rotation in the axes orientation.

With constant curvature fibers it is possible to define the fiber path on a ply just by defining the values of ϕ , T_0 and T_1 and it can be expressed as:

$$[\phi < T_0, T_1 >] \quad (1.2)$$

This nomenclature is taken from the literature [5]. A \pm symbol can be added to Equation (1.2) when the layup consists of two adjacent layers with same value of T_0 and T_1 but opposed in sign. Additionally, an s on the sub-index position indicates that other laminates are added with a rotated fiber orientation in order to achieve a symmetric structure [1].

In some cases a non-linear fiber orientation functions are used. This means that the curvature radius is not constant along the fiber. Some of the methods

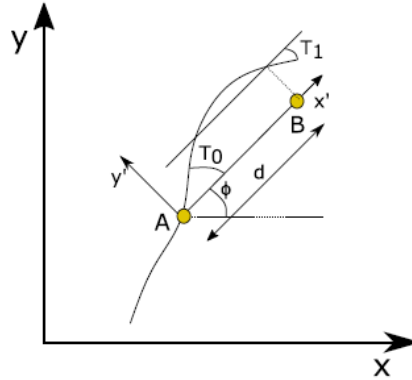


Figure 1.4: Example of a fiber path definition varying linearly along the characteristic length d . Extracted from [5]

to define path functions for non-linear cases involve Lobatto polynomials, Bezier curves or Lagrange polynomials [7]. An example from the literature of non-linear fiber orientation equation with Lagrange polynomials is:

$$\theta(x, y) = \sum_{m=0}^{M-1} \sum_{n=0}^{N-1} T_{mn} \prod_{m \neq i} \left(\frac{x - x_i}{x_m - x_i} \right) \prod_{n \neq j} \left(\frac{y - y_j}{y_n - y_j} \right) \quad (1.3)$$

The use of VSC implies vantages from the performance point of view. However, care has to be taken as fiber steering is prone to generate defects on the structure, being gaps and overlaps on the course boundary the most frequent ones [4].

1.4 Models for macro-mechanical analysis of VSC

Many authors have carried out investigations in order to understand how the mechanical performance of VSC is affected by manufacturing induced defects. Virtual tests applying Finite Element Methods (FEM) were performed for macro-mechanical analysis of VAT composites, including in the model some defects as fiber misalignment, tow-angle discontinuities, gaps and overlaps. These two lasts are the most commonly studied in the literature.

Authors as Blom *et al.* [3] modelled defective areas for gaps and overlaps by using a very refined meshing in order to fully capture the size of the defects. However, this method implied a high computational cost due to the big amount of elements. Other authors as August Noever and Craig Collier [8], applied a methodology in which the thickness of the model elements was adapted to include the effect of gaps and overlaps. This procedure, however, overestimated the VSC strength when studying overlaps. Another approach, applied by Cairns *et al.* in [9], doubled the

stiffness of overlaps areas and assigned the material properties of the matrix resin to gap areas.

In the work of Fayazbakhsh *et al.* [6], Matlab routines were implemented to detect gap and overlap areas over the composite layers. These defects were introduced in the model using the Defect Layer Method (DLM), which was computationally more efficient than previous works. DLM alters the properties of the elements of the model depending on its defect percentage area. For overlaps, the thickness of the model is increased proportionally to this area while gaps are modelled by scaling the material properties of the element. The performed analysis concluded that overlaps could benefit VSC performance whereas gaps reduce its strength. Further work was undertaken by Nik *et al.* [4] to study the effect of manufacturing parameters on this defective areas.

Authors O. Falcó *et al.* [10] and A. Pagani and A.R. Sanchez-Majano [5, 11] performed analysis being able to include defects at a meso-scale level, modeling each layer independently. In the former, X-ray tomography was used to analyze defects as fiber angle discontinuities, gaps and overlaps. The performed work analyzed failure mechanisms in notched and unnotched VSCs coming to the conclusion that gap effect has more incidence for unnotched plates. On the other hand, in [5, 11], Carrera Unified Formulation was implemented by the authors for modeling the VSC. The composite was defined using layer-wise (LW) theories which are able to model each layer independently introducing details at the meso-scale, for instance, fabrication induced imperfections. The approach was implemented to investigate the influence of fiber missalignments in VSC tows on its buckling performance and failure mechanisms. At the conclusion it is stated that LW models are compulsory to fully account the effect of meso-scale flaws.

1.5 Micro-scale modeling

The study of VSCs at the micro-scale level is motivated by the necessity to obtain its effective properties based on the fiber-matrix arrangement and the volume fraction of the two constituent phases [12].

Many models have been developed to study the fiber-matrix microstructure and obtain the material properties which can be applied in the macro-scale analysis.

Hashin and Rotem, proposed the Concentric Cylinder Model (CCM) in [13]. This analytical model derived the effective elastic moduli for parallel hollow circular fibers, contained in a cylindrical portion of composite, by a variational method. The procedure was able to develop the expressions of some of the effective elastic moduli.

Other semi-analytical works were able to provide not only the elastic moduli, but also the local fields at the constituent level. In many of these studies, a

representative volume element (RVE) is defined, which is a specific portion of material repeated along the VSC structure. Then, numerical methods are employed to estimate the material properties of the homogenized RVE.

This is the case of the models developed by Aboudi [14] and Aboudi *et al.* [15, 16]. In the prior, the author presented the Method of cells (MOC). It consisted in the study of a periodic square array divided in four subcells. One corresponding to the fiber and the other to the matrix. The model was capable to predict accurately the inelastic response of composites. In the other works of the author, the MOC was extended to the generalized method of cells (GMC), see [15], and the high-fidelity generalized method of cells (HFGMC), in [16]. These further developed theories resolved the local fields at the cell level, computed the effective material properties of the homogenized RVE and were able to obtain accurate results for non-linear and failure analysis. In [17], Williams developed the Elasticity based Cell method (ECM). It discretized cells in eight subregions and approximated the displacement field by truncated eigenfunctions of 5th order.

Other authors as Sun and Vaidya, predicted the composite properties from the RVE employing FEM, Gauss theorem and strain equivalence principles [18]. Kaleel *et al.* employed the Carrera Unified Formulation to develop a component-wise approach for the study of RVE. The method can be exploited to accurately obtain 3D-fields and displacements within the cell by means of interpolating the cross-section behaviour of the structure employing Lagrangian-type polynomials as expansion functions. Similarly, the works of A.G de Miguel *et al.* employ models based on the Carrera Unified Formulation altogether with the mechanics of the structure genome. This approach was capable to capture the effective properties of the homogenized cell and to compute the fields at the micro-scale level by implementing the variational asymptotic method. This least, minimizes the lost of information between the heterogeneous and the resulting homogenized cell. More information about micro-scale models for the study of composites can be found in [12].

1.6 Uncertainty on VSC

Most of the efforts to develop and study VSC use a deterministic approach which do not take into account the presence of uncertainties in composites [7]. However, composite materials are susceptible to space-dependent uncertainties consequence of the fabrication process and environmental factors [19]. This uncertainties may affect in a variety of forms. For instance, missalignments, waviness, aspect ratio or volume fraction are some of the fiber properties affected by it. With the deterministic perspective, the presence of uncertainty is mitigated by applying high safety factors, which may fall between 8 and 10 in some cases, obtaining

very conservative designs. Instead of big safety factors, taking into consideration uncertainties in the analysis enables to achieve robust and reliable designs. The optimization process to design relatively insensitive to uncertainty components is also named robust design optimization (RDO) [7].

As uncertainties generate a variability on the VSC properties which is difficult to control, space dependent random fields are usually used and methods based on stochastic simulations with random data sets are applied. Guimarães *et al.* [19] used a random field to model uncertainty on the material properties of VSC. In this case, the studied property was the Fiber Volume Fraction within the Fiber-Matrix structure. Uncertainty was propagated using Karhunen-Loeve Expansions (KLE) and affected space-variable mass and stiffness of the composites. Zhou *et al.* [7] introduced variability on the loading conditions, which were considered as random variables following a normal distribution. Scarth *et al.* [20], proposed a random field whose covariance function was based on the geodesic distance between points in curved surfaces. This random field defined the point-wise varying material properties of their model, which was subjected to a buckling analysis. Other works of Zhou *et al.* [21] applied stochastic finite element methods as well to model material properties and fiber angle variation. Pagani and Sánchez-Majano [5] employed the Covariance Matrix Decomposition (CMD) technique in order to obtain a random field to model fiber missalignment while investigating the buckling performance of VSC.

In many of the works [5, 19, 20, 21], uncertainty quantification was carried out by means of Monte Carlo simulation technique. This method calculates results many times using for each simulation a different set of stochastic values. Then, output data can be analyzed in order to obtain statistical parameters of the results and probability distributions which may help to understand uncertainty effects on the investigated factors.

1.7 Contents of this dissertation

The first part of this paper explains the formulation employed and the equations involved in the performed analyses. Chapter 2 presents the Carrera Unified Formulation and the constitutive equations which rule the finite element analyses for the VSCs. Later, Chapter 3 introduces the micro-mechanics theory employed in the study of the VSCs, which will allow to obtain the material properties for the finite element analysis and the recovery of the micro-scale fields. Then, Chapter 4 shows how uncertainty effects on the fiber volume fraction have been modeled and introduced in the analysis. Monte Carlo analysis and Polynomial chaos expansion are presented as tools for the study of the buckling performance of VSCs affected by uncertainty. Chapter 5 includes the verification stage for the models developed

in this study and the numerical results for both the static and buckling response of the VSCs. Macro and micro-scale analysis outcomes are included. Finally, Chapter 6 contains the conclusions which were deduced from the results obtained in this work.

Chapter 2

Layer-wise models of laminated VAT panels

2.1 Carrera Unified Formulation

Carrera Unified Formulation (CUF) is an approach which allows FE matrices to be written in a compacted way in terms of fundamental nuclei (FN). This framework can be applied for structural 1D, 2D and 3D problems [22]. On this dissertation, special attention will be paid to 1D models which are going to be applied to model VAT composite laminates. In 1D CUF formulation, the nodal displacement vector for any generic point in the three dimensional space can be defined as:

$$\mathbf{u}(x, y, z) = F_\tau(x, z)\mathbf{u}_\tau(y), \quad \tau = 1, 2, \dots, M \quad (2.1)$$

In this equation, the term F_τ corresponds to an expansion function of the cross-section which varies along the longitudinal direction y , and approximates the displacement values of the cross-section of the VSC. The \mathbf{u}_τ term is known as the generalized displacement unknown vector and M stands for the number of terms employed in the expansion. The accuracy of the approximation is ruled by this parameter, reaching more precision when increasing M value. Einstein notation is adopted in CUF, hence repeated subindexes imply summation of terms. Many different expansions F_τ can be used to define the behaviour of the cross-section. Some commonly used are based on the Taylor Expansion (TE), Lagrange Expansion (LE) or Hierarchical Legendre Expansion (HLE). These three models are going to be now explained but a review on other CUF beam theories using different expansions can be found in [23].

2.1.1 Taylor Expansion

TE is obtained making use of 2D series of the type $x^l z^m$ in which l and m are positive integers ranging between zero and the maximum polynomial order, N . The values of the F_τ functions and M can be expressed as function of N as it is shown in Table 2.1, which is obtained from the literature [22].

order	M	F_τ
0	1	$F_1 = 1$
1	3	$F_2 = x \quad F_3 = z$
2	6	$F_4 = x^2 \quad F_5 = xz \quad F_6 = z^2$
3	10	$F_7 = x^3 \quad F_8 = x^2z \quad F_9 = xz^2 \quad F_{10} = z^3$
\vdots	\vdots	\vdots
N	$\frac{(N+1)(N+2)}{2}$	$F_{(N^2+N+2)/2} = x^N \dots F_{(N+1)(N+2)/2} = z^N$

Table 2.1: Taylor expansion polynomial terms

For instance, using this type of expansion, a third order model can be expressed as follows:

$$\begin{aligned}
 u_x &= u_{x_1} + xu_{x_2} + zu_{x_3} + x^2u_{x_4} + xzu_{x_5} + z^2u_{x_6} + x^3u_{x_7} + x^2zu_{x_8} + xz^2u_{x_9} + z^3u_{x_{10}} \\
 u_y &= u_{y_1} + xu_{y_2} + zu_{y_3} + x^2u_{y_4} + xzu_{y_5} + z^2u_{y_6} + x^3u_{y_7} + x^2zu_{y_8} + xz^2u_{y_9} + z^3u_{y_{10}} \\
 u_z &= u_{z_1} + xu_{z_2} + zu_{z_3} + x^2u_{z_4} + xzu_{z_5} + z^2u_{z_6} + x^3u_{z_7} + x^2zu_{z_8} + xz^2u_{z_9} + z^3u_{z_{10}}
 \end{aligned} \tag{2.2}$$

This includes 30 generalized displacement unknowns in the cross-section. TE can achieve higher accuracy by adding higher order terms into the equations. In this case, the kinematics of the system are derived from constant ($N = 0$), linear ($N = 1$), parabolic ($N = 2$) and cubic terms ($N = 3$). Some classical beam theories, as Euler-Bernoulli and Timoshenko, can be obtained by selecting only some constant and linear terms of the TE [24].

2.1.2 Lagrange Expansion

LE models make use of Lagrange polynomials for the F_τ expansion functions. In the framework of CUF, when using LE approach the cross-section is divided into sub-domains in which 2D polynomials are employed to interpolate the unknowns over the transverse section. There are many different types of polynomials, including three-noded linear (L3), four-noded bilinear (L4), nine-noded quadratic (L9) or

sixteen-noded (L16). As L9 interpolation functions are going to be implemented in this work, its equations are here included:

$$\begin{aligned}
 F_\tau &= \frac{1}{4}(r^2 + rr_\tau)(s^2 + ss_\tau), \quad \tau = 1,3,5,7, \\
 F_\tau &= \frac{1}{2}s_\tau^2(s^2 + ss_\tau)(1 - r^2) + \frac{1}{2}r_\tau^2(r^2 + rr_\tau)(1 - s^2), \quad \tau = 2,4,6,8 \\
 F_\tau &= (1 - r^2)(1 - s^2) \quad \tau = 9
 \end{aligned} \tag{2.3}$$

in which r and s are normalized coordinates defined in the interval $[-1, 1] \times [-1, 1]$. Terms s_τ and r_τ correspond to the location of the roots of the polynomial functions. A Jacobian transformation has to be implemented to transform normalized geometry of the subdomains into their actual geometry [25].

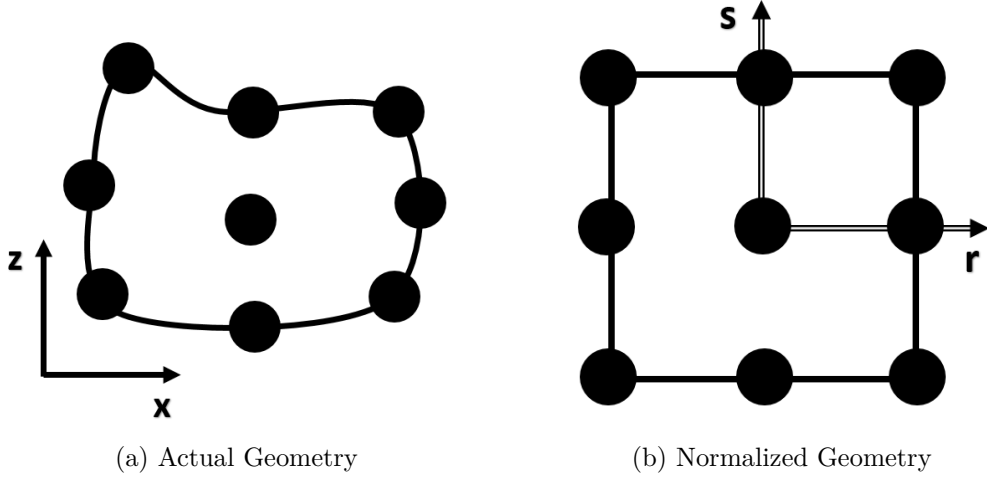


Figure 2.1: L9 Lagrange Expansion element geometry

More precision can be obtained by adopting higher order Lagrange polynomials or by refining the cross-section with a combination of multiple subdomains.

2.1.3 Hierarchical Legendre Expansion

HLE employs a hierarchical set of Legendre-like functions. This approach is based on an orthogonal basis of functions, which can be defined as:

$$\begin{aligned}
 L_0 &= 1 \\
 L_1 &= x \\
 L_p &= \frac{2p-1}{p}xL_{p-1}(x) - \frac{p-1}{p}L_{p-2}(x), \quad p = 2,3,\dots
 \end{aligned} \tag{2.4}$$

where p is the degree of the Legendre polynomial. For a 1D space a set of interpolated functions \tilde{L}_i can be obtained as follows

$$\begin{aligned}\tilde{L}_1(r) &= \frac{1}{2}(1-r) \\ \tilde{L}_2(r) &= \frac{1}{2}(1+r) \\ \tilde{L}_i(r) &= \phi_{i-1}(r), \quad i = 3, 4, \dots, p+1\end{aligned}\tag{2.5}$$

where $\phi_j(r)$ is defined as

$$\phi_j(r) = \sqrt{\frac{2j-1}{j}} \int_{-1}^r L_{j-1}(x) dx, \quad j = 2, 3, 4, \dots\tag{2.6}$$

\tilde{L}_i functions for $i = 1$ and $i = 2$ correspond to linear modes whose values fall within the range $[0, 1]$ along the domain $[-1, 1]$. For any other higher order these functions vanish on the edges of the interval and are known as internal modes [25]. The set of Legendre-like functions have inherent orthogonal properties. Therefore, the following expression applies to them:

$$\int_{-1}^1 \frac{d\tilde{L}_i}{dr} \frac{d\tilde{L}_j}{dr} dx = \delta_{ij}, \quad \text{for } i \geq 3 \text{ and } j \geq 1 \text{ or } i \geq 3 \text{ and } j \geq 1\tag{2.7}$$

in which δ_{ij} is known as Kronecker's delta whose values are given by:

$$\delta_{ij} = \begin{cases} 1 & \text{if } i = j \\ 0 & \text{if } i \neq j \end{cases}\tag{2.8}$$

The two-dimensional set of equations used for the expansion F_τ is obtained expanding the already explained formulation into a quadrilateral domain whose domain is $[-1, 1] \times [-1, 1]$. Three type of modes are therefore derived: nodal, edge and internal. There are four nodal modes and they are exactly as first order Lagrange quadrilateral polynomials [24]. These equations vanish on all nodes except for one and are expressed as

$$F_\tau = \frac{1}{4} (1 - r_\tau r) (1 - s_\tau s) \quad \tau = 1, 2, 3, 4\tag{2.9}$$

Secondly, there are four edge modes for each polynomial degree $p \geq 2$. In this case, their edge values differ from zero just for one of the four edges of the 2D-domain. The expansion equations which define these modes are

$$\begin{aligned}F_\tau(r, s) &= \frac{1}{2}(1-s)\phi_p(r) \quad \tau = 5, 9, 13, 18, \dots \\ F_\tau(r, s) &= \frac{1}{2}(1+r)\phi_p(s) \quad \tau = 6, 10, 14, 19, \dots \\ F_\tau(r, s) &= \frac{1}{2}(1+s)\phi_p(r) \quad \tau = 7, 11, 15, 20, \dots \\ F_\tau(r, s) &= \frac{1}{2}(1-r)\phi_p(s) \quad \tau = 8, 14, 16, 21, \dots\end{aligned}\tag{2.10}$$

Internal expansions result from the product of 1D internal modes. A total of $(p-2)(p-3)/2$ polynomials of this type are obtained for $p \geq 4$. The following formulas are an example of internal expansions for $p = 6$:

$$\begin{aligned} F_{28}(r, s) &= \phi_4(r)\phi_2(s) \\ F_{29}(r, s) &= \phi_3(r)\phi_3(s) \\ F_{30}(r, s) &= \phi_2(r)\phi_4(s) \end{aligned} \tag{2.11}$$

The precision of the F_τ Legendre-like polynomials can be increased by adopting higher p values.

2.2 Finite element approximation

2.2.1 Constitutive equations for VSC

According to classical elasticity and due to symmetric properties, the stress and strain tensors in reference to the global reference system (x, y, z) can be described each with a six-term vector following the Voigt notation as:

$$\begin{aligned} \sigma^T &= \left\{ \sigma_{xx} \quad \sigma_{yy} \quad \sigma_{zz} \quad \sigma_{xz} \quad \sigma_{yz} \quad \sigma_{xy} \right\} \\ \varepsilon^T &= \left\{ \varepsilon_{xx} \quad \varepsilon_{yy} \quad \varepsilon_{zz} \quad \varepsilon_{xz} \quad \varepsilon_{yz} \quad \varepsilon_{xy} \right\} \end{aligned} \tag{2.12}$$

The relationship between the strain tensor and the displacements can be written as:

$$\begin{aligned} \begin{pmatrix} \varepsilon_{xx} \\ \varepsilon_{yy} \\ \varepsilon_{zz} \\ \varepsilon_{xz} \\ \varepsilon_{yz} \\ \varepsilon_{xy} \end{pmatrix} &= \begin{bmatrix} \frac{\partial}{\partial x} & 0 & 0 \\ 0 & \frac{\partial}{\partial y} & 0 \\ 0 & 0 & \frac{\partial}{\partial z} \\ \frac{\partial}{\partial z} & 0 & \frac{\partial}{\partial x} \\ 0 & \frac{\partial}{\partial z} & \frac{\partial}{\partial y} \\ \frac{\partial}{\partial y} & \frac{\partial}{\partial x} & 0 \end{bmatrix} \begin{pmatrix} u_x \\ u_y \\ u_z \end{pmatrix} \end{aligned} \tag{2.13}$$

which can be expressed in a compact notation by

$$\boldsymbol{\varepsilon} = \mathbf{D}\mathbf{u} \tag{2.14}$$

being D the linear differential operator. In composite laminates the mechanical properties are dependent on the fiber orientation angle. By adopting a material reference system with axes $(1, 2, 3)$, it is possible to obtain the following equation given by Hooke's law:

$$\sigma_m = \mathbf{C}\varepsilon_m \tag{2.15}$$

where subindex m indicates the use of the material reference system and \mathbf{C} corresponds to the stiffness matrix of the material, which is defined as:

$$\mathbf{C} = \begin{bmatrix} C_{33} & C_{23} & C_{13} & 0 & 0 & 0 \\ C_{23} & C_{22} & C_{12} & 0 & 0 & 0 \\ C_{13} & C_{12} & C_{11} & 0 & 0 & 0 \\ 0 & 0 & 0 & C_{44} & 0 & 0 \\ 0 & 0 & 0 & 0 & C_{55} & 0 \\ 0 & 0 & 0 & 0 & 0 & C_{66} \end{bmatrix} \quad (2.16)$$

In this work, two kind of materials are going to be presented:

- Isotropic materials: These materials have identical elastic properties in all directions of the 3D-space. In this case, the terms of matrix \mathbf{C} are computed as follows:

$$\begin{aligned} C_{11} &= C_{22} = C_{33} = \frac{(1-\nu)E}{(1+\nu)(1-2\nu)} \\ C_{12} &= C_{13} = C_{23} = C_{21} = C_{31} = C_{32} = \frac{\nu E}{(1+\nu)(1-2\nu)} \\ C_{44} &= C_{55} = C_{66} = \frac{E}{2(1+\nu)} \end{aligned} \quad (2.17)$$

For isotropic materials all coefficients of \mathbf{C} are function of only two elastic constants, E and ν , known respectively as Young modulus and Poisson ratio.

- Orthotropic materials: The elastic properties of this type of materials exhibit two symmetry planes. In order to fully define the material, nine elastic constants are needed. These are three Young moduli (E_1, E_2, E_3), three shear moduli (G_{12}, G_{13}, G_{23}) and three Poisson ratios ($\nu_{12}, \nu_{13}, \nu_{23}$). Then, \mathbf{C} coefficients are obtained with the following formulae:

$$\begin{aligned} C_{11} &= \frac{E_1(1-\nu_{23}\nu_{32})}{\beta}, & C_{12} &= \frac{E_1(\nu_{21}+\nu_{23}\nu_{31})}{\beta}, & C_{13} &= \frac{E_1(\nu_{31}+\nu_{21}\nu_{32})}{\beta} \\ C_{21} &= \frac{E_2(\nu_{12}+\nu_{13}\nu_{32})}{\beta}, & C_{22} &= \frac{E_2(1-\nu_{13}\nu_{31})}{\beta}, & C_{23} &= \frac{E_2(\nu_{32}+\nu_{12}\nu_{31})}{\beta} \\ C_{31} &= \frac{E_3(\nu_{13}+\nu_{12}\nu_{23})}{\beta}, & C_{32} &= \frac{E_3(\nu_{23}+\nu_{13}\nu_{21})}{\beta}, & C_{33} &= \frac{E_3(1-\nu_{12}\nu_{21})}{\beta} \\ C_{44} &= G_{21}, & C_{55} &= G_{31}, & C_{66} &= G_{23} \end{aligned} \quad (2.18)$$

where the parameter β is obtained by the following relation:

$$\beta = 1 - \nu_{12}\nu_{21} - \nu_{23}\nu_{32} - \nu_{13}\nu_{31} - 2\nu_{21}\nu_{32}\nu_{13} \quad (2.19)$$

Due to the orthogonal symmetric properties the following relations are satisfied:

$$\frac{\nu_{ij}}{E_i} = \frac{\nu_{ji}}{E_j} \quad \text{imply} \quad C_{12} = C_{21}, \quad C_{13} = C_{31}, \quad C_{23} = C_{32} \quad (2.20)$$

In both above-explained cases, the stiffness matrix is defined using material reference system. To translate the matrix into the global reference frame two angles are necessary, θ and ϕ . These angles correspond to the rotation of the material axes in relation to the global axes, as in Figure 2.2. In this work, material axis 3 is defined always parallel to the fiber orientation while 1 and 2 define the out-of-plane and in-plane directions of the fiber transverse section. Stress and strain vectors can be translated from one reference frame to another using a transformation matrix \mathbf{T} :

$$\begin{aligned}\boldsymbol{\sigma} &= \mathbf{T}\boldsymbol{\sigma}_m \\ \boldsymbol{\varepsilon} &= \mathbf{T}\boldsymbol{\varepsilon}_m\end{aligned}\quad (2.21)$$

in which the coefficients terms of matrix \mathbf{T} are function of angles θ and ϕ . Matrix \mathbf{T} is not reported herein, but can be found in the book by Reddy [26]. Finally, Hooke's law in the global coordinate system can be expressed as:

$$\boldsymbol{\sigma} = \mathbf{TCT}^T\boldsymbol{\varepsilon} = \tilde{\mathbf{C}}\boldsymbol{\varepsilon}\quad (2.22)$$

Each coefficient of $\tilde{\mathbf{C}}$ is computed with the elastic constants of the material and is function of the fiber orientation angles, θ and ϕ . $\tilde{\mathbf{C}}_{ij}$ expressions are here omitted for the sake of brevity, but can be found in the paper by Carrera and Filippi [27].

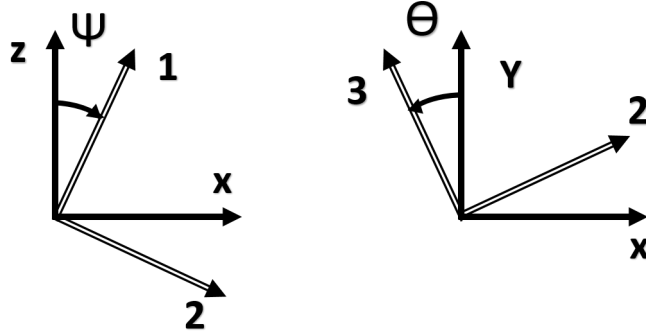


Figure 2.2: Fiber rotation angles

In the case of VSC, the fiber orientation angle varies point-wise within the ply. Therefore, the fiber angle can be expressed as a function of the in-plane cartesian coordinates, $\theta(x, y)$, as it is shown in Figure 2.3. For this reason, the rotation matrix \mathbf{T} is dependent on the point coordinates as well. Equation (2.22) is redefined as:

$$\boldsymbol{\sigma} = \mathbf{T}(x, y)\mathbf{C}\mathbf{T}^T(x, y)\boldsymbol{\varepsilon} = \tilde{\mathbf{C}}(x, y)\boldsymbol{\varepsilon}\quad (2.23)$$

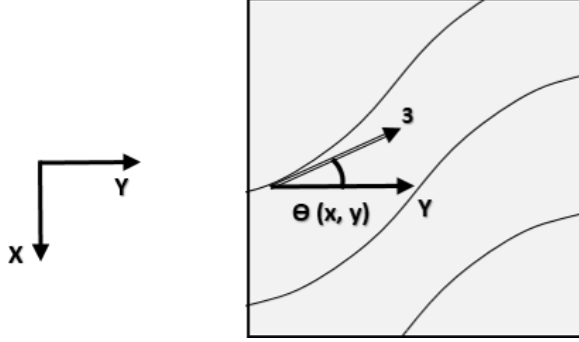


Figure 2.3: Fiber orientation angle on VAT

2.2.2 Finite Element Formulation

On this dissertation, Finite Elements (FE) formulation has been chosen for the analysis of VSC structures. It has been proven that the coupling of FE and 1D CUF-based theories constitute a powerful analysis tool for VAT composite laminates [11, 28, 29, 30]. Using FEM, the generalized displacement at any point of the 1D axis can be described as

$$\mathbf{u}_\tau(y) = N_i(y)\mathbf{u}_{\tau i}, \quad i = 1, 2, \dots, n_e, \quad (2.24)$$

where N_i is a 1D shape function, n_e is the number of nodes per element and the unknown nodal vector $\mathbf{u}_{\tau i}$ is defined as

$$\mathbf{u}_{\tau i} = \left\{ u_{x\tau i} \quad u_{y\tau i} \quad u_{z\tau i} \right\}^T \quad (2.25)$$

To define the shape functions applied on the longitudinal axis, also named beam axis, Lagrange beam elements are usually employed. The polynomials which describe this kind of elements are obtained by the formula

$$N_i(\xi) = \prod_{j=1, j \neq i}^{r_b} \frac{\xi - \xi_j}{\xi_i - \xi_j} \quad \text{with} \quad \begin{cases} j = 1, \dots, n_e \\ -1 \leq \xi \leq 1 \end{cases} \quad (2.26)$$

in which r_b is the order of the Lagrange polynomial. An important property of these polynomials is that its roots (ξ_i) are equidistant. Lagrange shape functions for two-node (B2), three-node (B3) and four-node (B4) beam elements can be found in [22]. Cubic element B4 formulation is here included as it will be employed on the case analysis of the present work:

$$\begin{aligned} N_1 &= -\frac{9}{16} \left(\xi + \frac{1}{3} \right) \left(\xi - \frac{1}{3} \right) (\xi - 1), & N_2 &= \frac{9}{16} \left(\xi + \frac{1}{3} \right) \left(\xi - \frac{1}{3} \right) (\xi + 1), \\ N_3 &= +\frac{27}{16} (\xi + 1) \left(\xi - \frac{1}{3} \right) (\xi - 1), & N_4 &= -\frac{27}{16} (\xi + 1) \left(\xi + \frac{1}{3} \right) (\xi - 1), \end{aligned} \quad (2.27)$$

Finally, introducing Equation (2.24) into Equation (2.1), the displacement field results:

$$\mathbf{u}(x, y, z) = F_\tau(x, z)N_i(y)\mathbf{u}_{\tau i}, \quad \tau = 1, 2, \dots, M \quad i = 1, 2, \dots, n_e \quad (2.28)$$

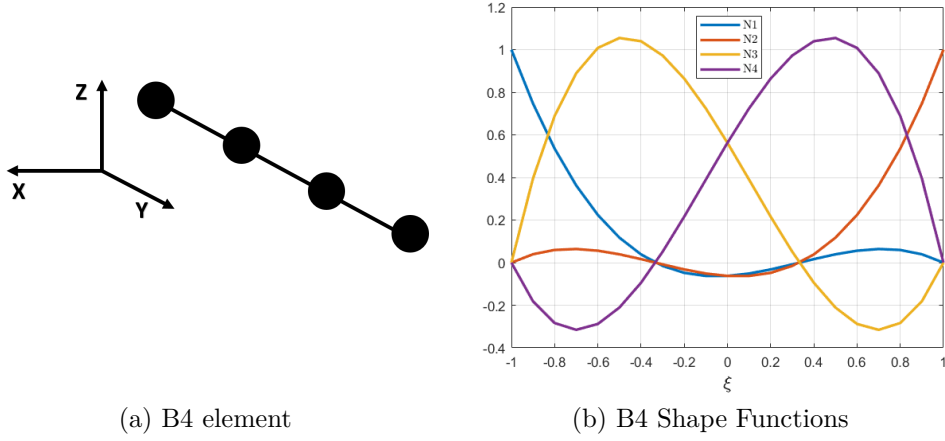


Figure 2.4: B4 (four-node) Lagrange beam element for the longitudinal direction and its shape functions

2.2.3 Principle of virtual displacements

The equations that govern the FE problem are obtained by means of the principle of virtual displacements (PVD). PVD states that it is a necessary condition for the equilibrium of a structure that the virtual variation of the internal work has to be equal to the virtual variation of the work of external forces and the virtual variation of inertial volume forces. This equality is stated as:

$$\delta L_{\text{int}} = \delta L_{\text{ext}} + \delta L_{\text{ine}} \quad (2.29)$$

All terms of Equation (2.29) can be written in a compacted notation as follows:

$$\begin{aligned} \delta L_{\text{int}} &= \delta \mathbf{u}_{s_j}^T \mathbf{K}^{\tau s i j} \mathbf{u}_{\tau i}, \\ \delta L_{\text{ine}} &= -\delta \mathbf{u}_{s_j}^T \mathbf{M}^{i j \tau s} \ddot{\mathbf{u}}_{\tau i}, \quad \tau, s = 1, 2, \dots, M \quad i, j = 1, 2, \dots, n_e \\ \delta L_{\text{ext}} &= \delta \mathbf{u}_{s_j}^T \mathbf{P}^{s j} \end{aligned} \quad (2.30)$$

where $\mathbf{K}^{\tau sij}$ is a 3 x 3 matrix that constitutes the FN of the stiffness matrix, $\mathbf{M}^{ij\tau s}$ corresponds to the FN of the mass matrix of the FE, and \mathbf{P}^{sj} is a vector which contains the components of external forces concentrated on each element and $\ddot{u}_{\tau i}$ is the vector of nodal acceleration values. It is important to state that $\mathbf{K}^{\tau sij}$ terms are independent from the type and the order of the structural theory chosen, being this one of the main advantages of the appliance of CUF. For the sake of completeness, the equations to obtain the coefficients of the FN stiffness matrix for an orthotropic material are here included:

$$\begin{aligned}
 K_{xx}^{\tau sij} &= \tilde{C}_{22} I_{ij} E_{\tau, xs, x} + \tilde{C}_{44} I_{ij} E_{\tau, zs, z} + \tilde{C}_{26} I_{ij, y} E_{\tau, xs} + \tilde{C}_{26} I_{i, yj} E_{\tau s, x} + \tilde{C}_{66} I_{i, yj, y} E_{\tau s} \\
 K_{xy}^{\tau sij} &= \tilde{C}_{23} I_{ij, y} E_{\tau s, x} + \tilde{C}_{45} I_{ij} E_{\tau, zs, z} + \tilde{C}_{26} I_{ij} E_{\tau, xs, x} + \tilde{C}_{36} I_{i, yj, y} E_{\tau s} + \tilde{C}_{66} I_{i, yj} E_{\tau s, x} \\
 K_{xz}^{\tau sij} &= \tilde{C}_{12} I_{ij} E_{\tau, xs, z} + \tilde{C}_{44} I_{ij} E_{\tau, zs, x} + \tilde{C}_{45} I_{ij, y} E_{\tau, zs} + \tilde{C}_{16} I_{i, yj} E_{\tau s, z} \\
 K_{yx}^{\tau sij} &= \tilde{C}_{23} I_{i, yj} E_{\tau s, x} + \tilde{C}_{45} I_{ij} E_{\tau, zs, z} + \tilde{C}_{26} I_{ij} E_{\tau, xs, x} + \tilde{C}_{36} I_{i, yj, y} E_{\tau s} + \tilde{C}_{66} I_{ij, y} E_{\tau, xs} \\
 K_{yy}^{\tau sij} &= \tilde{C}_{33} I_{i, yj, y} E_{\tau s} + \tilde{C}_{55} I_{ij} E_{\tau, zs, z} + \tilde{C}_{36} I_{ij, y} E_{\tau, xs} + \tilde{C}_{36} I_{i, yj} E_{\tau s, x} + \tilde{C}_{66} I_{ij} E_{\tau, xs, x} \\
 K_{yz}^{\tau sij} &= \tilde{C}_{13} I_{i, yj} E_{\tau s, z} + \tilde{C}_{55} I_{ij, y} E_{\tau, zs} + \tilde{C}_{45} I_{ij} E_{\tau, zs, x} + \tilde{C}_{16} I_{ij} E_{\tau, xs, z} \\
 K_{zx}^{\tau sij} &= \tilde{C}_{12} I_{ij} E_{\tau, zs, x} + \tilde{C}_{44} I_{ij} E_{\tau, xs, z} + \tilde{C}_{45} I_{i, yj} E_{\tau s, z} + \tilde{C}_{16} I_{i, yj} E_{\tau, z s} \\
 K_{zy}^{\tau sij} &= \tilde{C}_{13} I_{ij, y} E_{\tau, zs} + \tilde{C}_{55} I_{i, yj} E_{\tau s, z} + \tilde{C}_{45} I_{ij} E_{\tau, xs, z} + \tilde{C}_{16} I_{ij} E_{\tau, z s, x} \\
 K_{zz}^{\tau sij} &= \tilde{C}_{11} I_{ij} E_{\tau, zs, z} + \tilde{C}_{44} I_{ij} E_{\tau, xs, x} + \tilde{C}_{55} I_{i, yj, y} E_{\tau s} + \tilde{C}_{45} I_{ij, y} E_{\tau, xs} + \tilde{C}_{45} I_{i, yj} E_{\tau s, x}
 \end{aligned} \tag{2.31}$$

where E and I terms are computed by resolving the following integral equations:

$$\begin{aligned}
 E_{\tau, xs, x} &= \int_{\Omega} F_{\tau, x} F_{s, x} d\Omega, & E_{\tau, zs, z} &= \int_{\Omega} F_{\tau, z} F_{s, z} d\Omega, & E_{\tau s} &= \int_{\Omega} F_{\tau} F_s d\Omega, \\
 E_{\tau, xs, z} &= \int_{\Omega} F_{\tau, x} F_{s, z} d\Omega, & E_{\tau, zs, x} &= \int_{\Omega} F_{\tau, z} F_{s, x} d\Omega, & E_{\tau, xs} &= \int_{\Omega} F_{\tau, x} F_s d\Omega, \\
 E_{\tau s, x} &= \int_{\Omega} F_{\tau} F_{s, x} d\Omega, & E_{\tau, z s} &= \int_{\Omega} F_{\tau, z} F_s d\Omega, & E_{\tau s, z} &= \int_{\Omega} F_{\tau} F_{s, z} d\Omega,
 \end{aligned} \tag{2.32}$$

$$\begin{aligned}
 I_{ij} &= \int_l N_i N_j dy & I_{ij, y} &= \int_l N_i N_{j, y} dy \\
 I_{i, yj} &= \int_l N_{i, y} N_j dy & I_{i, yj, y} &= \int_l N_{i, y} N_{j, y} dy
 \end{aligned} \tag{2.33}$$

being l the plate's length on the longitudinal direction. On the other hand, the mass matrix is diagonal, which means that only terms on the diagonal are not null. This diagonal coefficients can be computed with the formula:

$$\mathbf{M}_{xx}^{ij\tau s} = \mathbf{M}_{yy}^{ij\tau s} = \mathbf{M}_{zz}^{ij\tau s} = \rho \int_l N_i N_j dy \int_{\Omega} F_{\tau} F_s d\Omega \tag{2.34}$$

Only constant density (ρ) components are going to be here considered.

Finally, by substituting Equation (2.30) in Equation (2.29) the following expression is obtained:

$$\delta u_{sj}^T \mathbf{M}^{ij\tau s} \ddot{u}_{\tau i} + \delta u_{sj}^T \mathbf{K}^{\tau sij} u_{\tau i} = \delta \mathbf{u}_{sj}^T \mathbf{P}^{sj} \quad (2.35)$$

2.2.4 Static analysis

The static analysis is the first FE problem which is going to be here considered. The equilibrium state of the structure implies that the nodal acceleration vector, $\ddot{u}_{\tau i}$, is null. Taking this into consideration, the FE problem governing Equation (2.35) can be written as:

$$\delta u_{sj}^T \mathbf{K}^{\tau sij} u_{\tau i} = \delta \mathbf{u}_{sj}^T \mathbf{P}^{sj} \quad (2.36)$$

in which \mathbf{u}_{sj}^T term can be omitted from both sides, obtaining the following equation:

$$\mathbf{K}^{\tau sij} u_{\tau i} = \mathbf{P}^{sj} \quad (2.37)$$

The unknowns of the analysis are the displacements $u_{\tau i}$. These can be obtained by simply resolving the system:

$$u_{\tau i} = \mathbf{K}^{\tau sij^{-1}} \mathbf{P}^{sj} \quad (2.38)$$

2.2.5 Linearized buckling analysis

The second analysis here presented is a linearized buckling analysis. The equations that govern this analysis are also obtained from the PVD. The following expression is obtained from the L_{int} term of Equation (2.30):

$$\delta^2 (L_{int}) = \delta \mathbf{u}_{sj}^T \mathbf{K}_T^{ij\tau s} \delta \mathbf{u}_{\tau i} \quad (2.39)$$

where $\mathbf{K}_T^{ij\tau s}$ corresponds to the tangent stiffness matrix of the structure under investigation. In order to get to the buckling problem solution it is needed to seek for bifurcations and limit points of the equilibrium state [5]. In other words, it is resolved by solving the following problem:

$$|\mathbf{K}_T| = 0 \quad (2.40)$$

The problem is here linearized, obtaining the following equation:

$$\delta^2 (L_{int}) \cong \delta \mathbf{u}_{sj}^T \left(\mathbf{K}_0^{ij\tau s} + \mathbf{K}_\sigma^{ij\tau s} \right) \delta \mathbf{u}_{\tau i} \quad (2.41)$$

in which $\mathbf{K}_0^{ij\tau s}$ and $\mathbf{K}_\sigma^{ij\tau s}$ are respectively the FN of the linear and the geometric stiffness matrix or pre-stress stiffness. The equations needed to compute the

coefficients of the later, can be found in [31]. Finally, applying the linearized approach the buckling problem is defined as follows:

$$|\mathbf{K}_T + \lambda_{cr}\mathbf{K}_\sigma| = 0 \quad (2.42)$$

The resolution of the system provide the critical buckling loads, λ_{cr} . Later in this paper, the effect of uncertainty factors on these critical loads will be investigated.

2.3 ESL vs LW modeling techniques

In this section two different approaches are going to be presented for modeling the composite structure. The first one is known as Equivalent single layer (ESL). When applying ESL, the composite is modelled as a single layer whose stiffness matrix of the structure is computed by summing the contributions of all the plies. Therefore, it results in a unique layer with homogenized variables over its cross-section. A representation of CUF application for ESL is shown in Figure 2.5.

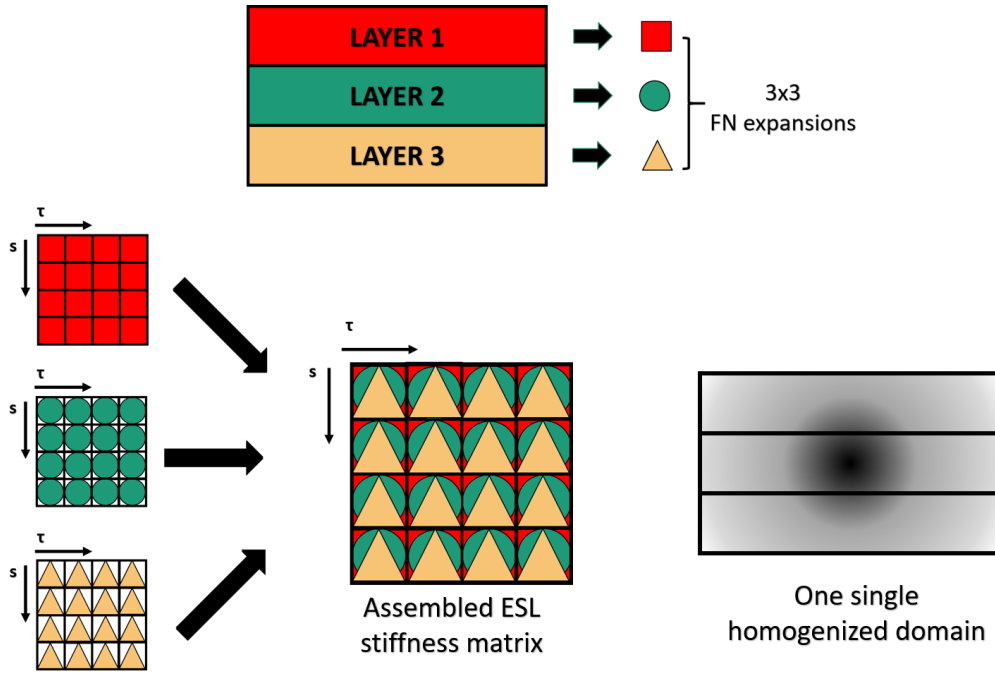


Figure 2.5: Equivalent single layer assembly procedure of the stiffness matrix

The material coefficients can be computed for the ESL approach with the

following formula:

$$E_{\tau_{(x),(z)}s_{(x),(z)}} = \sum_{k=1}^{n_k} \tilde{C}^k(x, y) \int_b \int_{z_b^k}^{z_t^k} F_{\tau_{(x),(z)}} F_{s_{(x),(z)}} dz dx \quad (2.43)$$

where n_k is the number of layers on the composite, z_b^k and z_t^k are respectively the z coordinates of the bottom and the top of the layer k and b is the layer width. Finally, eventual partial derivatives are indicated by the subindexes between brackets.

The second approach corresponds to the Layer-Wise (LW) modeling. In this case, the variables of all layers are studied separately. Also the contribution of each layer to the structure stiffness matrix is considered independently. Then, a condition of continuity on the displacement field between layers is imposed as:

$$u_{top}^k = u_{bottom}^{k+1} \quad (2.44)$$

where k is again referred to the layer numbering. This relation establishes that the displacement values of the points in a common side of two adjacent plies are equal. A representation of the LW approach is described in Figure 2.6:

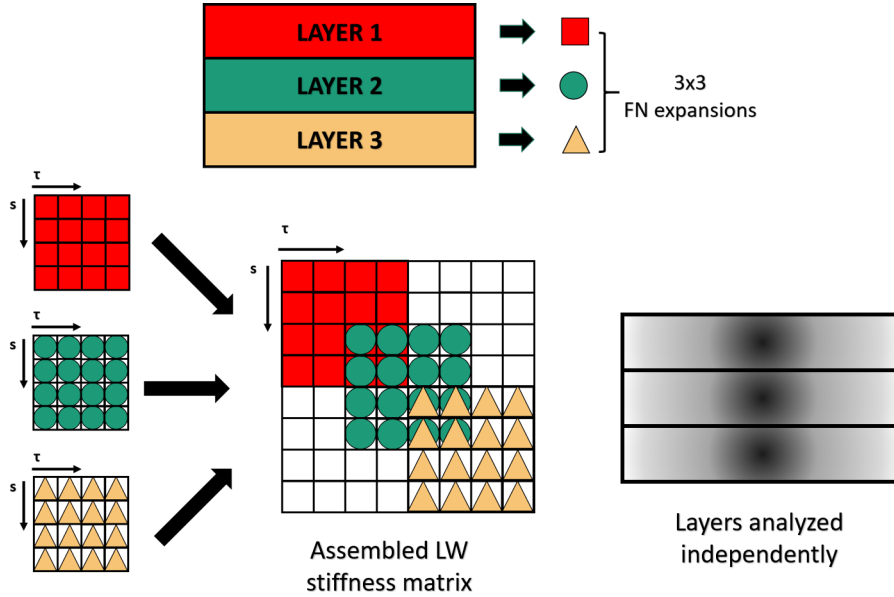


Figure 2.6: Layer-wise assembly procedure of the stiffness matrix

The following formula, included as an example, allows the computation of the matrix stiffness coefficients when applying LW approach based on LE for the

cross-section expansion:

$$E_{\tau(x)(,z)s(x)(,z)}^k = \tilde{C}^k(x, y) \int_{-1}^1 \int_{-1}^1 F_{\tau(r)(s)} F_{s(r)(s)} |\mathbf{J}_{\Omega_k}| dr ds \quad (2.45)$$

in which J_{Ω_k} corresponds to the Jacobian transformation matrix for the subdomain Ω_k . This matrix allows the transformation between expansion natural coordinates (r, s) into cartesian (x, z) system.

Despite the fact that both approaches can be modelled using TE, LE and HLE (among others) expansions, for practical reasons, TE is preferred for ESL while LE and HLE are usually employed for LW. The application of LE and HLE in LW is more convenient due to the cross-section division into subdomains, which allow the layer-wise modeling for the analysis. The application of the ESL approach allows the resolution of the FE problem with a low computational cost as it just considers one single layer for the analysis. However, the main disadvantage of the method is the lack of capability to describe intrinsic effects of each layer specifically, due to the homogenization process. For this reason, LW approach is preferred, as it allows us to model each layer independently, with its own characteristics, defects or other factors of interest.

Chapter 3

Micro-mechanics

VSCs are complex structures which are normally affected by factors and defects on its microstructure. Variability on the fiber volume fraction (FVF), void content on the material or the presence of multiple phases in the composition are some examples of factors affecting the structure on a micro-scale level. The analysis performed in this work aims to take into account microstructure details and their effect on the global structure. For this purpose, the approach of the mechanics of structure genome (MSG) is herein adopted, where the global structure is divided into structure genomes. These are the smallest mathematical building blocks which can be defined within the structure.

MSG micromechanics theory allows a precise resolution of the unit cell (UC) problem, decoupling the multi-scale of the problem into global and local analyses. The main goals pursued in the microstructure's study are two:

1. Obtain the stiffness properties of the homogenized UC, which can be later applied for the global analysis of the structure.
2. Recover the local fields of displacements, stress or strain over the volume of the UC from the outputs of the global solution.

In the following section, the UC selected for our VSC is going to be presented, together with its formulation.

3.1 Unit Cells

A unit cell (UC) is defined as the minimum geometrical arrangement of the materials that is repeated all over the structure. It must contain all the necessary information as to be able to identify the material properties at the macro-scale. In order to find the proper UC which defines VSC, special attention is payed into the fiber and epoxy matrix distribution along the layers of the composite. Then, an assumption

is made for which the fibers follow a regular and periodic pattern, allowing the identification of the UC, which in the case of VSC coincides with the structure genome. Figure 3.1 shows an example of a structure with a heterogeneous composition and periodically repeated cells from which a UC has been identified.

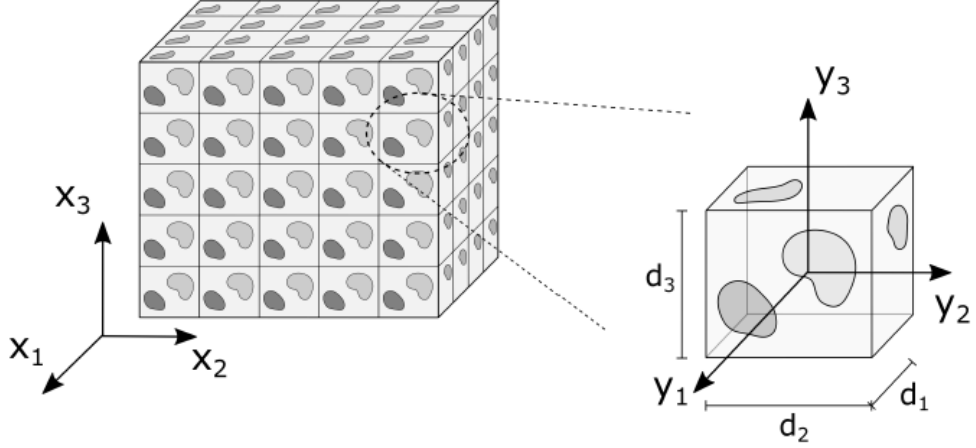


Figure 3.1: Heterogeneous material with periodically repeated cells. Extracted from [25]

In order to proceed with the multi-scale analysis it is necessary to define the coordinate systems for the global coordinate system, from now on named $\mathbf{x} = \{x_1, x_2, x_3\}$, and the local reference system for the UC, $\mathbf{y} = \{y_1, y_2, y_3\}$. Both coordinate systems are related to each other through a scaling parameter δ , characteristic of the UC dimension, as follows:

$$y_i = \frac{x_i}{\delta} \quad (3.1)$$

An important property is that the average of the local values over the UC volume correspond with the values obtained from the global solution. Therefore, it is possible to write:

$$\frac{1}{V} \int_V \phi_i(\mathbf{x}, \mathbf{y}) dV = \bar{\phi}_i(\mathbf{x}) \quad i = 1, 2, 3, \quad (3.2)$$

where ϕ represents a generic field from the solutions of the studied problem, V is the volume of the UC and $\bar{\phi}$ is the field average value over the volume. The connection between the different neighbouring UC is defined by periodic boundary

conditions whose mathematical expressions are:

$$\begin{aligned} \phi_i \left(x_1, x_2, x_3; \frac{d_1}{2}, y_2, y_3 \right) &= \phi_i \left(x_1 + d_1, x_2, x_3; -\frac{d_1}{2}, y_2, y_3 \right) \\ \phi_i \left(x_1, x_2, x_3; y_1, \frac{d_2}{2}, y_3 \right) &= \phi_i \left(x_1, x_2 + d_2, x_3; y_1, -\frac{d_2}{2}, y_3 \right) \\ \phi_i \left(x_1, x_2, x_3; y_1, y_2, \frac{d_3}{2} \right) &= \phi_i \left(x_1, x_2, x_3 + d_3; y_1, y_2, -\frac{d_3}{2} \right) \end{aligned} \quad (3.3)$$

in which d_1 , d_2 and d_3 define the dimensions of the studied UC, as shown in Figure 3.1. For the VSCs of this study, the UC consists of a square pack microstructure as it can be seen in Figure 3.2. The UC lay-up is a cubic domain of epoxy that contains in its center the fiber reinforcement, which has a circular cross-section.

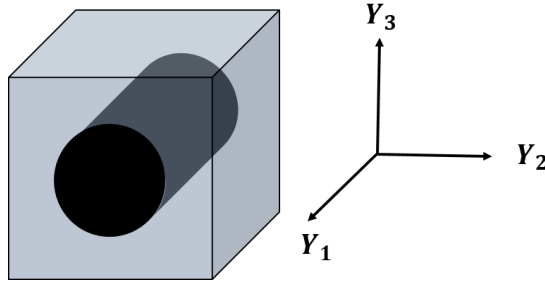


Figure 3.2: Unit cell consisting on a circular transverse-section fiber surrounded by a portion of epoxy matrix

3.2 Variational Asymptotic Method

MSG applies the variational asymptotic method (VAM) in order to solve the structural problem of the UCs. This method computes stationary points of a functional given a certain variational statement. In our case, this functional of the stationary problem which has to be minimized, denoted as Π , corresponds to the difference between the strain energies of the UC and the equivalent homogenized material. Functional Π can be expressed with the following formulation:

$$\Pi = \frac{1}{V} \int_V \frac{1}{2} \mathbf{C}_{ijkl} \varepsilon_{ij} \varepsilon_{kl} dV - \frac{1}{2} \mathbf{C}_{ijkl}^* \bar{\varepsilon}_{ij} \bar{\varepsilon}_{kl} = \left\langle \frac{1}{2} C_{ijkl} \varepsilon_{ij} \varepsilon_{kl} \right\rangle - \frac{1}{2} C_{ijkl}^* \bar{\varepsilon}_{ij} \bar{\varepsilon}_{kl} \quad (3.4)$$

where the first term of the equation corresponds to the heterogeneous microstructure strain energy average and the second is the strain energy of the equivalent homogenized material. From now on, the volume average integral $\frac{1}{V} \int_V \bullet dV$ will be denoted as $\langle \bullet \rangle$. The other parameters correspond to the elastic tensors (C_{ijkl}),

strain tensors (ε) and global strains ($\bar{\varepsilon}$). Then, local displacements can be written as:

$$u_i(\mathbf{x}; \mathbf{y}) = \bar{u}_i(\mathbf{x}) + \delta \chi_i(\mathbf{x}; \mathbf{y}) \quad (3.5)$$

in which χ_i are local fluctuation functions. These are multiplied by the scaling parameter δ . After applying derivatives to Equation (3.5) and neglecting smaller terms the local strain function is derived as:

$$\varepsilon_{ij}(\mathbf{x}; \mathbf{y}) = \bar{\varepsilon}_{ij}(\mathbf{x}) + \chi_{(i,j)}(\mathbf{x}; \mathbf{y}) \quad (3.6)$$

Then, the following constraints are applied:

$$\bar{u}_i = \langle u_i \rangle \quad \bar{\varepsilon}_{ij} = \langle \varepsilon_{ij} \rangle \quad \langle \chi_i \rangle = 0 \quad \langle \chi_{(i,j)} \rangle = 0 \quad (3.7)$$

Therefore, considering the homogenized structure as invariable, the functional can be written as:

$$\Pi_1 = \frac{1}{2} \langle C_{ijkl} (\bar{\varepsilon}_{ij} + \chi_{(i,j)}) (\bar{\varepsilon}_{kl} + \chi_{(k,l)}) \rangle \quad (3.8)$$

Then, the MSG problem consists on finding the χ functions that minimize Π_1 .

3.3 VAM and FE methods

To resolve the UC-problem, FE methods and CUF-based theories are again applied. For that purpose, the local coordinate axes are defined as in Figure 3.2. The fluctuation unknowns are expanded over the UC cross-section using expansion functions, F_τ , as follows:

$$\boldsymbol{\chi}(\mathbf{x}; y_1, y_2, y_3) = F_\tau(y_2, y_3) \boldsymbol{\chi}_\tau(\mathbf{x}; y_1) \quad \tau = 1, 2, \dots, M \quad (3.9)$$

in which $\boldsymbol{\chi}_\tau$ stands for the vector of generalized unknowns along y_1 -direction. The analysis is performed from a component wise (CW) perspective, modeling independently the kinematics of the two materials: fiber reinforcement and matrix resin. The expansion over the plane y_2y_3 uses HLE polynomials. Therefore, the cross-section is divided into subdomains. On the other hand, the discretization of the longitudinal axis employs Lagrangian beam elements as the ones employed in Chapter 2. For that reason, the χ_τ are interpolated along the beam direction in the following way:

$$\boldsymbol{\chi}_\tau(\mathbf{x}; y_1) = N_i(y_1) \boldsymbol{\chi}_{\tau i}(\mathbf{x}) \quad i = 1, 2, \dots, n \quad (3.10)$$

where $\chi_{\tau i}$ and n are respectively the vector of nodal unknowns and the number of Lagrangian beam nodes. For the beam element, the following geometrical relations apply:

$$\boldsymbol{\varepsilon} = \bar{\boldsymbol{\varepsilon}} + \mathbf{D}\boldsymbol{\chi} \quad (3.11)$$

where the global strains are:

$$\bar{\boldsymbol{\varepsilon}}^T = \left\{ \bar{\varepsilon}_{11} \quad \bar{\varepsilon}_{22} \quad \bar{\varepsilon}_{33} \quad 2\bar{\varepsilon}_{23} \quad 2\bar{\varepsilon}_{13} \quad 2\bar{\varepsilon}_{12} \right\} \quad (3.12)$$

and \mathbf{D} is a differential operator which can be described as:

$$\mathbf{D} = \begin{bmatrix} \frac{\partial}{\partial y_1} & 0 & 0 \\ 0 & \frac{\partial}{\partial y_2} & 0 \\ 0 & 0 & \frac{\partial}{\partial y_3} \\ 0 & \frac{\partial}{\partial y_3} & \frac{\partial}{\partial y_2} \\ \frac{\partial}{\partial y_3} & 0 & \frac{\partial}{\partial y_1} \\ \frac{\partial}{\partial y_2} & \frac{\partial}{\partial y_1} & 0 \end{bmatrix} \quad (3.13)$$

After introducing the FE formulation, the functional described in Equation (3.8) can be written now as:

$$\Pi_1^* = \frac{1}{2} \int_V (\bar{\boldsymbol{\varepsilon}} + \mathbf{D}\boldsymbol{\chi})^T \tilde{\mathbf{C}} (\bar{\boldsymbol{\varepsilon}} + \mathbf{D}\boldsymbol{\chi}) dV \quad (3.14)$$

The periodic boundary conditions presented on Equation (3.3) imply:

$$\chi_{\tau 1} = \chi_{\tau n} \quad \tau = 1, 2, \dots, M \quad (3.15)$$

being 1 and n the first and last nodes. An important aspect of this implementation is that the problem solutions are constant along the beam axis, which means that a B2 Lagrange element is enough for the interpolation in the Y_1 -direction, without suffering a loss of accuracy. Finally, the functional Π_1^* can be rewritten as:

$$\Pi_1^* = \frac{1}{2} \left(\boldsymbol{\chi}_{sj}^T \mathbf{E}^{\tau sij} \boldsymbol{\chi}_{\tau i} + 2\boldsymbol{\chi}_{sj}^T \mathbf{D}_{h\varepsilon}^{\tau i} \bar{\boldsymbol{\varepsilon}} + \bar{\boldsymbol{\varepsilon}}^T \mathbf{D}_{\varepsilon\varepsilon} \bar{\boldsymbol{\varepsilon}} \right) \quad (3.16)$$

where $\mathbf{E}^{\tau sij}$ and $\mathbf{D}_{h\varepsilon}^{sj}$ are respectively 3×3 and 3×6 matrices which constitute the fundamental nuclei of the UC-problem. $\mathbf{D}_{\varepsilon\varepsilon}$ is a 6×6 matrix that corresponds to the effective stiffness matrix of the material by volume average. The expressions of these matrices can be written as:

$$\begin{aligned} \mathbf{E}^{\tau sij} &= \int_l \int_{\Omega} (\mathbf{D} (F_{\tau} N_i \mathbf{I}))^T \tilde{\mathbf{C}} \mathbf{D} (F_s N_j \mathbf{I}) d\Omega dy_1 \\ \mathbf{D}_{h\varepsilon}^{\tau i} &= \int_l \int_{\Omega} (\mathbf{D} (F_{\tau} N_i \mathbf{I}_3))^T \tilde{\mathbf{C}} d\Omega dy_1 \\ \mathbf{D}_{\varepsilon\varepsilon} &= \int_l \int_{\Omega} \tilde{\mathbf{C}} d\Omega dy_1 \end{aligned} \quad (3.17)$$

where l stands for the length of the UC on the beam axis and I is a 3×3 identity matrix. Here, the coefficient expressions of matrix $\mathbf{E}^{\tau sij}$ are equal to the ones of matrix $\mathbf{K}^{\tau sij}$, introduced in Chapter 2. On the other hand, the formulas to obtain the terms of matrix $\mathbf{D}_{h\bar{\varepsilon}}^{\tau i}$ are the following:

$$\begin{aligned}
 D_{h\bar{\varepsilon}11}^{\tau i} &= \tilde{\mathbf{C}}_{11} \int_l N_{i,y_1} dy_1 \int_{\Omega} F_{\tau} d\Omega & D_{h\bar{\varepsilon}12}^{\tau i} &= \tilde{\mathbf{C}}_{12} \int_l N_{i,y_1} dy_1 \int_{\Omega} F_{\tau} d\Omega \\
 D_{h\bar{\varepsilon}13}^{\tau i} &= \tilde{\mathbf{C}}_{13} \int_l N_{i,y_1} dy_1 \int_{\Omega} F_{\tau} d\Omega & D_{h\bar{\varepsilon}14}^{\tau i} &= 0 \\
 D_{h\bar{\varepsilon}15}^{\tau i} &= \tilde{\mathbf{C}}_{55} \int_l N_i dy_1 \int_{\Omega} F_{\tau,z} d\Omega & D_{h\bar{\varepsilon}16}^{\tau i} &= \tilde{\mathbf{C}}_{66} \int_l N_i dy_1 \int_{\Omega} F_{\tau,x} d\Omega \\
 D_{h\bar{\varepsilon}21}^{\tau i} &= \tilde{\mathbf{C}}_{12} \int_l N_i dy_1 \int_{\Omega} F_{\tau,x} d\Omega & D_{h\bar{\varepsilon}22}^{\tau i} &= \tilde{\mathbf{C}}_{22} \int_l N_i dy_1 \int_{\Omega} F_{\tau,x} d\Omega \\
 D_{h\bar{\varepsilon}23}^{\tau i} &= \tilde{\mathbf{C}}_{23} \int_l N_i dy_1 \int_{\Omega} F_{\tau,x} d\Omega & D_{h\bar{\varepsilon}24}^{\tau i} &= \tilde{\mathbf{C}}_{44} \int_l N_i dy_1 \int_{\Omega} F_{\tau,z} d\Omega \\
 D_{h\bar{\varepsilon}25}^{\tau i} &= 0 & D_{h\bar{\varepsilon}26}^{\tau i} &= \tilde{\mathbf{C}}_{66} \int_l N_{i,y_1} dy_1 \int_{\Omega} F_{\tau} d\Omega \\
 D_{h\bar{\varepsilon}31}^{\tau i} &= \tilde{\mathbf{C}}_{13} \int_l N_i dy_1 \int_{\Omega} F_{\tau,z} d\Omega & D_{h\bar{\varepsilon}32}^{\tau i} &= \tilde{\mathbf{C}}_{23} \int_l N_i dy_1 \int_{\Omega} F_{\tau,z} d\Omega \\
 D_{h\bar{\varepsilon}33}^{\tau i} &= \tilde{\mathbf{C}}_{33} \int_l N_i dy_1 \int_{\Omega} F_{\tau,z} d\Omega & D_{h\bar{\varepsilon}34}^{\tau i} &= \tilde{\mathbf{C}}_{44} \int_l N_i dy_1 \int_{\Omega} F_{\tau,x} d\Omega \\
 D_{h\bar{\varepsilon}25}^{\tau i} &= \tilde{\mathbf{C}}_{55} \int_l N_{i,y_1} dy_1 \int_{\Omega} F_{\tau} d\Omega & D_{h\bar{\varepsilon}26}^{\tau i} &= 0
 \end{aligned} \tag{3.18}$$

Finally, the expression which gives the minimum value of the functional is obtained. Taking into account that $\chi_{\tau i}$ is a linear function of $\bar{\varepsilon}$, the linear system of equations can be written as:

$$\mathbf{E}^{\tau sij} \chi_{\tau i 0} = -\mathbf{D}_{h\bar{\varepsilon}}^{\tau i} \tag{3.19}$$

in which the fluctuation solutions are found in the 3×6 matrix $\chi_{\tau i 0}$.

3.4 Cross-section mapping

Occasionally, standard isoparametric elements which are used to define the cross-section fail to define curved geometries. One advantage of employing HLE as F_{τ} is the ability to represent curved boundaries by means of non-isoparametric techniques. In our case, it is of great importance to properly define the geometry of the UC, which contains curved boundaries for the fiber reinforcement (Figure 3.2), in order to precisely apply the CW approach. The correct representation of the geometry can be achieved with the help of mapping functions, \mathbf{Q} , whose role is to define the curved boundaries when transforming the domain from the normalized (r, s) to the global coordinates (x, z) , as shown in Figure 3.3. Therefore, cross-section coordinates can be written as:

$$\begin{aligned}
 x &= \mathbf{Q}_x(r, s) \\
 z &= \mathbf{Q}_z(r, s)
 \end{aligned} \tag{3.20}$$

A review on some possible mapping techniques is going to be now presented:

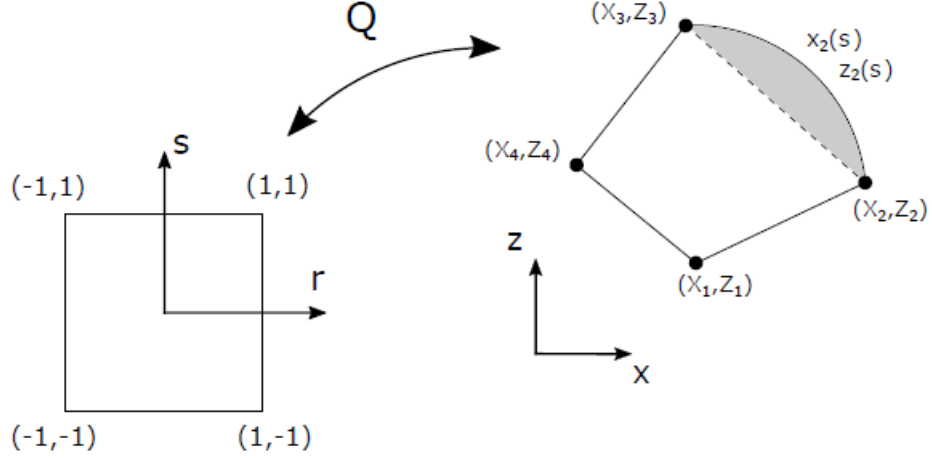


Figure 3.3: Transformation to the global coordinate system using mapping functions. Extracted from [25]

3.4.1 First order mapping

These mapping functions make use of linear expansion functions. Boundaries are approximated using piece-wise linear curves. The following expressions correspond to a first order mapping of a four node subdomain:

$$\begin{aligned}
 x = Q_x(r, s) &= \frac{1}{4}(1-r)(1-s)X_1 + \frac{1}{4}(1+r)(1-s)X_2 \\
 &\quad + \frac{1}{4}(1+r)(1+s)X_3 + \frac{1}{4}(1-r)(1+s)X_4 \\
 z = Q_z(r, s) &= \frac{1}{4}(1-r)(1-s)Z_1 + \frac{1}{4}(1+r)(1-s)Z_2 \\
 &\quad + \frac{1}{4}(1+r)(1+s)Z_3 + \frac{1}{4}(1-r)(1+s)Z_4
 \end{aligned} \tag{3.21}$$

where (X_i, Z_i) indicate the vertex of the subdomain. This kind of mapping is not suitable for representing curved boundaries.

3.4.2 Second order mapping

Second order mapping employs quadratic Lagrangian polynomials as mapping functions. By using a parabolic approximation the error when representing curved lines is reduced. The description of the Lagrangian polynomials can be found in Chapter 2 of this dissertation.

3.4.3 Blending function method

The last mapping technique which is presented is the blending function method (BFM). This method is able to reproduce the exact geometry of the cross-section by generating non-isoparametric HLE domains. For this purpose, a pair of parametric functions are defined for each edge of the domain. For example, taking the geometry of Figure 3.3, the domain edge $(\overline{X_2X_3}, \overline{Z_2Z_3})$ is described by functions $x = x_2(s)$ and $z = z_2(s)$ for defining the curved feature. This equations can be read as:

$$\begin{aligned} x_2(s) &= a_x + b_x s + c_x s^2 + d_x s^3 \\ z_2(s) &= a_z + b_z s + c_z s^2 + d_z s^3 \end{aligned} \quad (3.22)$$

where the following conditions are imposed:

$$\begin{aligned} x_2(-1) &= X_2, & x_2(1) &= X_3 \\ z_2(-1) &= Z_2, & z_2(1) &= Z_3 \end{aligned} \quad (3.23)$$

leading to the following expressions:

$$\begin{aligned} x &= Q_x(r, s) = F_\tau(r, s)X_\tau + \left(x_2(s) - \left(\frac{1-s}{2}X_2 + \frac{1+s}{2}X_3 \right) \right) \frac{1+r}{2} \\ z &= Q_z(r, s) = F_\tau(r, s)Z_\tau + \left(z_2(s) - \left(\frac{1-s}{2}Z_2 + \frac{1+s}{2}Z_3 \right) \right) \frac{1+r}{2} \end{aligned} \quad (3.24)$$

where F_τ corresponds to the first-order mapping and $(1+r)/2$ is named blending function. This last term imposes the vanishing of the transformation on the opposite edge of the domain. Finally, applying this formulation to all domain edges results in:

$$\begin{aligned} x &= Q_x(r, s) = \frac{1}{2}(1-s)x_1(r) + \frac{1}{2}(1+r)x_2(s) + \frac{1}{2}(1+s)x_3(r) \\ &\quad + \frac{1}{2}(1-r)x_4(s) - F_\tau(r, s)X_\tau \\ z &= Q_z(r, s) = \frac{1}{2}(1-s)z_1(r) + \frac{1}{2}(1+r)z_2(s) + \frac{1}{2}(1+s)z_3(r) \\ &\quad + \frac{1}{2}(1-r)z_4(s) - F_\tau(r, s)Z_\tau \end{aligned} \quad (3.25)$$

Therefore, the actual geometry of the domain is captured as shown in Figure 3.4. The accuracy of the method relies on the order of the polynomials. It is decided to employ BFM in this work with the aim of describing the microstructure geometry of VSCs unit cells.

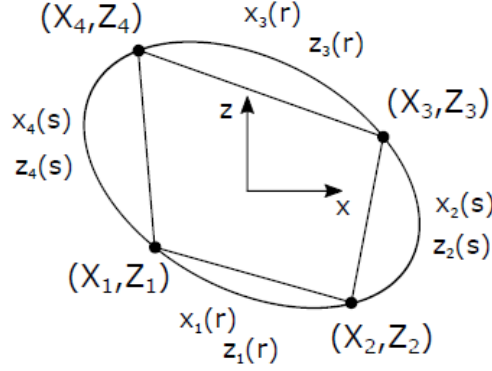


Figure 3.4: Actual geometry of the cross-section achieved via BFM. Figure obtained from [25]

3.5 Equivalent stiffness properties and local field recovery

One important aspect of the UC-problem is that allows one to obtain the effective properties or equivalent properties of an homogenized UC. By imposing equal values of energy stored in the heterogeneous material as in the homogenized one, the following equation is obtained:

$$\tilde{\mathbf{C}}^* = \frac{1}{V} \left(\boldsymbol{\chi}_{sj0}^T \mathbf{D}_{h\epsilon}^{sj} + \mathbf{D}_{\epsilon\epsilon} \right) \quad (3.26)$$

where matrix $\tilde{\mathbf{C}}^*$ stands for the stiffness matrix of the equivalent homogenized volume.

Once the structural stationary problem is solved, local stresses can be computed from Hooke's law, $\boldsymbol{\sigma} = \tilde{\mathbf{C}}^* \boldsymbol{\epsilon}$, by introducing the local strains with the fluctuation solutions:

$$\boldsymbol{\epsilon} = \bar{\boldsymbol{\epsilon}} + \mathbf{D} (F_\tau N_i \boldsymbol{\chi}_{\tau i 0} \bar{\boldsymbol{\epsilon}}) \quad (3.27)$$

Further knowledge about the implementation of the microstructure formulation developed in this chapter can be found in the works by A.G. de Miguel *et al.* [25, 32].

Chapter 4

Defect uncertainty quantification

4.1 Multi-scale Uncertainty Analysis

All manufacturing processes are affected by small variations that can introduce uncertainty into the final properties and characteristics of the manufactured components. AFP is not an exception and VSCs are not exempt from uncertainty issues. However, uncertainty detrimental effects can be reduced by taking them into account during the design stage of the components. Therefore, it is of great importance to introduce uncertainty in the design analysis in order to obtain robust designs, which are relatively insensitive to it.

Uncertainties may affect VSCs in many different ways. In this work, special attention is paid to manufacturing induced variability at a micro-scale level, affecting the FVF. As it was explained in Chapter 3, this parameter governs the cross-section fiber-matrix proportion of the UC defined for the our VSCs in Figure 3.2. Different values of FVF lead to different mechanical and material properties of the homogenized UC, which later affects the properties of the global structure.

The procedure applied in this study is the following:

- Firstly, uncertainty affecting the micro-scale parameter FVF within each ply is modelled as a random field.
- Secondly, expressions of the material and mechanical properties for the homogenized UC are obtained by applying regression methods to the UC-problem. It allows the computation of the UC homogenized properties as a regression function only of the FVF parameter.
- FVF random field is sampled on the Gauss integration points of the ply.

Properties in each of the points are calculated employing the above-mentioned regression functions and these values are used to compute the FE matrices.

- The procedure is repeated for each VSC ply separately. At the end, the layer-wise modelled final structure is obtained, with the micro-scale uncertainty effects integrated in the FE matrices.
- Then, a Monte Carlo analysis is performed in order to characterise the linearized buckling response. VSC macro-scale buckling response data is gathered and uncertainty effects investigated.
- Finally, the local fields at the micro-scale are recovered from the static solution of the global problem.

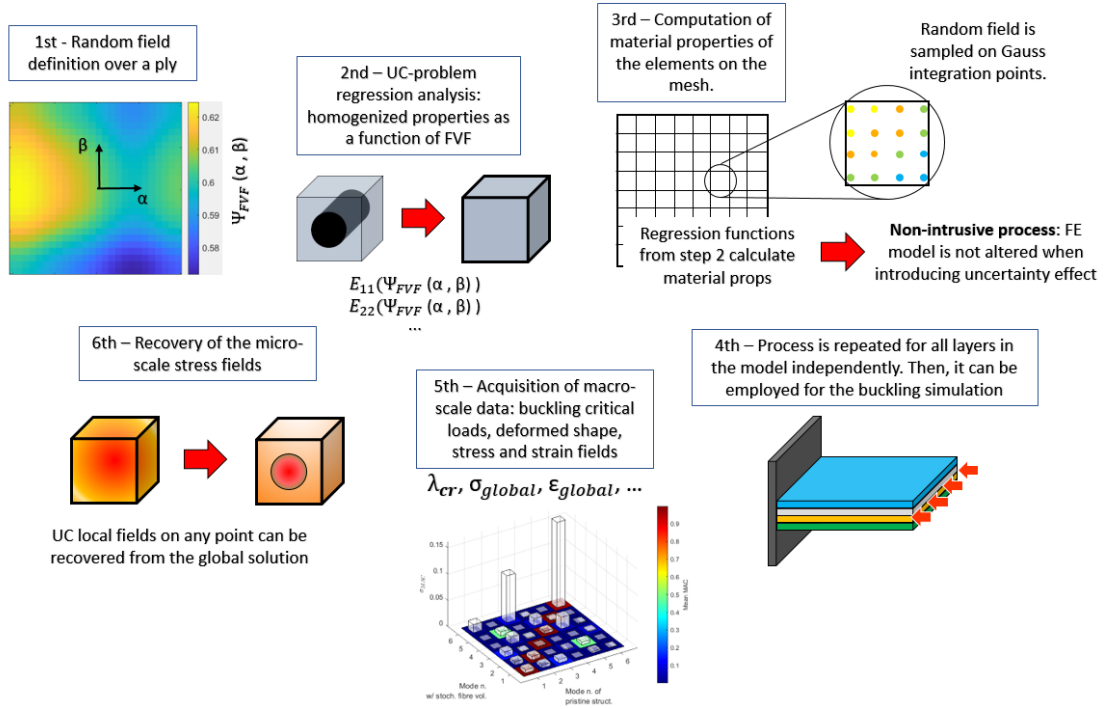


Figure 4.1: Scheme of the multi-scale problem

4.2 Modeling uncertainty

Due to the nature of uncertainty, it is practically impossible to predict exactly how it will affect the component. For this reason, a common way of modeling it is by means of stochastic or random fields. These fields generate random variations

on the parameters which are later spread over the ply surface. There are many different ways to generate stochastic fields [33]. In this work, a similar procedure as one from the literature is reproduced. The formulation herein applied is therefore based on the work by Guimarães *et al.* [19].

4.2.1 Random field

Random fields are developed to define FVF values all over the VSC plies. In this study, the generated stochastic field is intended to behave as a normal distribution with mean value μ and standard deviation σ . The μ value corresponds to the expected nominal value of FVF, which is defined during the design. On the other hand, σ regulates the field dispersion. This last parameter has to be defined according to the dispersion level of the actual manufacturing process variability.

A new reference system is employed to model random fields. To obtain the new coordinates (α, β) , it is necessary to transform the global coordinates of the ply points, (x, y) , making them dimensionless. Parameters α and β are defined as:

$$\alpha = 2x/a \quad \text{and} \quad \beta = 2y/b \quad (4.1)$$

where a and b are the side lengths of the VSC plate. The new dimensionless coordinate system origin is placed at the center of the plate geometry. Therefore, all VSC plate points are contained in the domain $[-1,1] \times [-1,1]$. According to this new reference system, the FVF stochastic field can be expressed as:

$$\Psi_{FVF}(\alpha, \beta; \omega) = \bar{\Psi}_{FVF} + \sigma \Delta \Psi_{FVF}(\alpha, \beta; \omega) \quad (4.2)$$

in which ω is a variable associated to each stochastic experiment of the space of random events Ω . The first term, $\bar{\Psi}_{FVF}$, corresponds to the gaussian mean value μ or expected FVF nominal value. The second one, $\Delta \Psi_{FVF}(\alpha, \beta; \omega)$ is a random zero-mean Gaussian, which introduces variability on the field Ψ_{FVF} as a function of the geometrical position (α, β) of each point inside the VSC plate.

4.2.2 Karhunen-Loeve Expansion

To model the space-distributed random field, the Karhunen-Loeve Expansion (KLE) is employed. According to this approach, Ψ_{FVF} values are approximated by means of the eigenvalues and eigenfunctions of the covariance function $\rho(\mathbf{X}_1, \mathbf{X}_2)$, in which $\mathbf{X}_1 = (\alpha, \beta)$ and $\mathbf{X}_2 = (\alpha', \beta')$ are two generic points of the plate. By definition, $\rho(\mathbf{X}_1, \mathbf{X}_2)$ is a bounded, symmetric and positive definite function which can be expressed as its spectral decomposition:

$$\rho(\mathbf{X}_1, \mathbf{X}_2) = \sum_{i=0}^{\infty} \lambda_i h_i(\mathbf{X}_1) h_i(\mathbf{X}_2) \quad (4.3)$$

where λ_i and h_i are respectively the eigenvalues and eigenfunctions of the covariance kernel which can be obtained by solving the following integral eigenvalue problem:

$$\int_{\mathbf{D}} \rho(\mathbf{X}_1, \mathbf{X}_2) h(\mathbf{X}_2) d\mathbf{X}_2 = \lambda h(\mathbf{X}_1) \quad (4.4)$$

which is a second kind homogeneous Fredholm integral. With KLE, the term of Equation (4.2), $\Delta\Psi_{FVF}(\alpha, \beta, \omega)$, can be written as:

$$\Delta\Psi_{FVF}(\alpha, \beta; \omega) = \sum_{i=1}^{\infty} \xi_i(\omega) \sqrt{\lambda_i} h_i(\alpha, \beta) \quad (4.5)$$

By truncating the series to the K^{th} term of the expansion, the integral problem of Equation (4.4), on the dimensionless domain previously defined, can be expressed as:

$$\int_{-1}^1 \int_{-1}^1 \rho(\alpha, \beta, \alpha', \beta') h_i(\alpha', \beta') d\alpha' d\beta' = \lambda_i h_i(\alpha, \beta) \quad i = 1, 2, \dots, K \quad (4.6)$$

and Equation (4.5) can be approximated as:

$$\Delta\Psi_{FVF}(\alpha, \beta; \omega) = \sum_{i=1}^K \xi_i(\omega) \sqrt{\lambda_i} h_i(\alpha, \beta) \quad (4.7)$$

Here, K is the number of terms on the truncated KLE and ξ_i corresponds to a set of K random numbers obtained from a Gaussian zero-mean normal.

There are many possible function types which can be selected as covariance function. Exponential functions are usually employed on the literature for this purpose. In this work, the following exponential function, obtained from [19], is applied:

$$\rho(\alpha, \beta, \alpha', \beta') = \exp\left(-\frac{|\alpha - \alpha'|}{\bar{l}_x} - \frac{|\beta - \beta'|}{\bar{l}_y}\right) \quad (4.8)$$

in which

$$\bar{l}_x = l_x/a, \quad \bar{l}_y = l_y/b \quad (4.9)$$

where \bar{l}_x and \bar{l}_y are the dimensionless correlation distance parameters. It is important to state that in this study, the correlation distance value is equal for both x and y dimensions. This results in an isotropic variation of the random field. The use of the correlation equation implies that high correlated points, which are the ones that are close to each other, will have similar field values, whereas points being far apart will have a larger field value difference.

Finally, the stochastic field for the FVF, employing KLE, can be written as:

$$\Psi_{FVF}(\alpha, \beta; \omega) = \bar{\Psi}_{FVF} + \sigma \sum_{i=1}^K \xi_i(\omega) \sqrt{\lambda_i} h_i(\alpha, \beta) \quad (4.10)$$

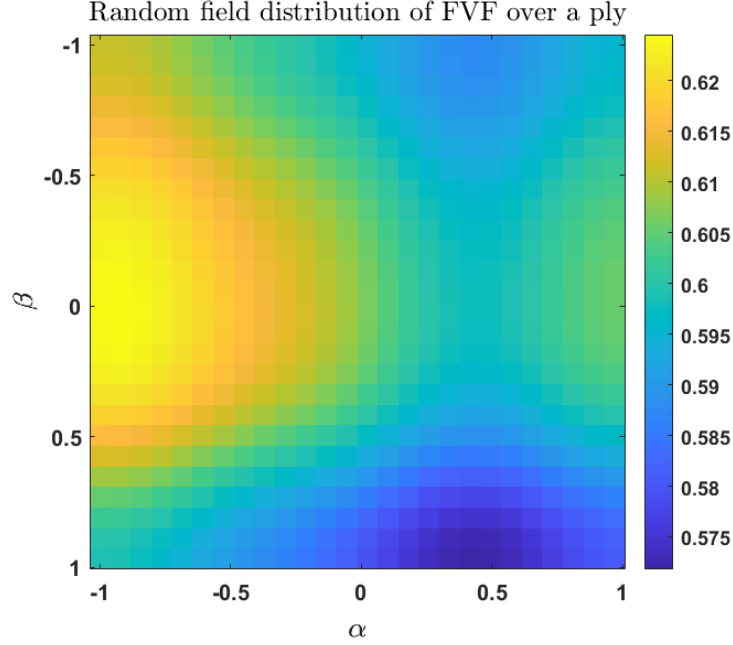


Figure 4.2: Stochastic field $\Psi_{FVF}(\alpha, \beta; \omega)$ expanded over a ply using KLE with parameters $(\bar{\Psi}_{FVF}, \sigma) = (0.6, 0.02)$

The random field is therefore described by the following parameters:

- $\bar{\Psi}_{FVF}$: corresponds to the expected nominal value of FVF. It can also be named μ as it coincides with the mean value of the gaussian field.
- σ : this parameter regulates the dispersion level of the field. It has to be selected by the designer based on experience.
- λ and $h(\alpha, \beta)$: respectively, eigenvalues and eigenfunctions calculated from the Fredholm integral, see Equation (4.4).
- ξ_i : a set of K random values sampled from $N(0, 1)$ gaussian distributions.

Further knowledge about KLE can be found in the book by Ghanem and Spanos [34].

4.2.3 Latin Hypercube Sampling Method

As it was presented in the previous section, ξ_i vector is a set of K values sampled from a $N(0,1)$ normal distribution. In order to ensure that the sampling process is properly and efficiently done, Latin Hypercube Sampling (LHS) is applied.

LHS divides the probability space of the uncertain parameter ξ into N_T segments with equal probability. N_T is equal to the sample size, which in our case coincides with K , the number of terms of the KLE. Therefore, the probability of each segment is $1/K$.

ξ_i values are computed by sampling once on each of the equally-probable range segments. Additionally, pairing methods are applied in order to obtain LHS schemes with the proper stochastic correlation. Otherwise sampled values could be linearly correlated.

The use of LHS is motivated by its capability to provide, in comparison to classical random sampling methods, a more accurate description of the employed input probability density function (PDF) tails and for yielding statistic estimators which present lower standard deviation [35].

4.2.4 Coupling random field and FEM

Once the stochastic field is designed, it is possible to generate a random distribution of FVF over the ply. Ψ_{FVF} is a function of the in-plane ply dimensionless coordinates (α, β) . The random variability effect is introduced in the FE model when computing the material and stiffness matrices for each element in the model mesh. For this purpose, equations which describe the variation of the homogenized orthotropic material properties with the FVF of each point within a laminate are obtained via regression analysis of the UC-problem. A polynomial fitting process is applied, obtaining the now point-wise varying material properties.

Regression functions

$$\begin{array}{ccc}
 E_{11}(\psi_{FvF}) & & E_{11}(\alpha, \beta) \\
 E_{22}(\psi_{FvF}) & \text{with } \psi_{FVF}(\alpha, \beta) \implies & E_{22}(\alpha, \beta) \\
 G_{12}(\psi_{FvF}) & & G_{12}(\alpha, \beta) \\
 \vdots & & \vdots
 \end{array} \quad (4.11)$$

These expressions are used to couple the random field and the FE analysis. When the stiffness matrices of the elements are computed, the material properties are obtained evaluating the mentioned equations in the Gauss integration points and are employed in the calculation process of the matrices.

This method has the ability to introduce the modifications of the properties of the element without having to modify the model mesh or the formulation of

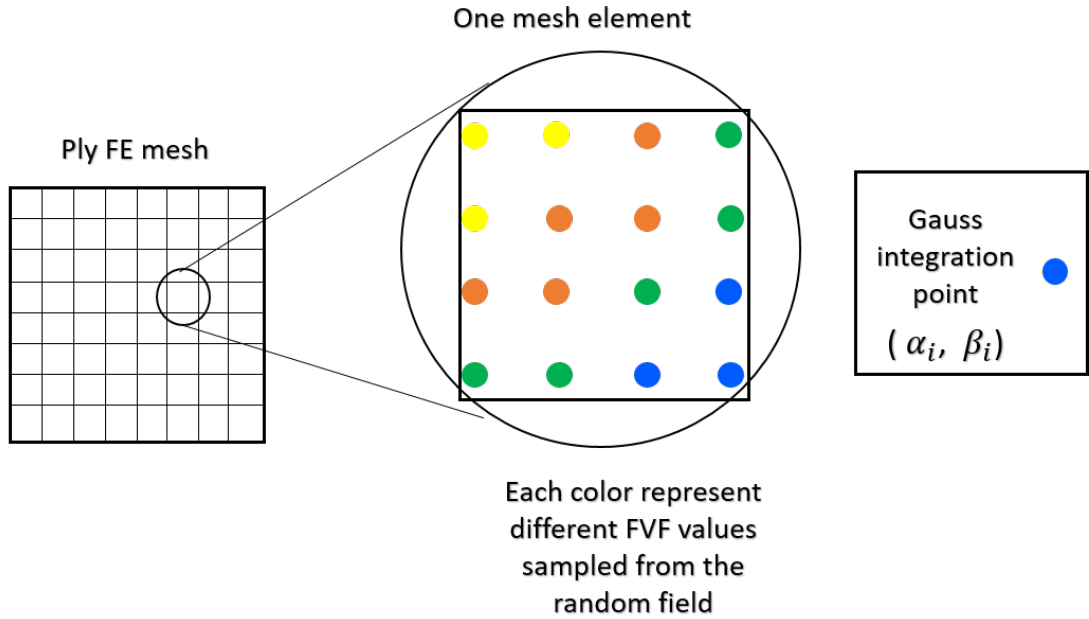


Figure 4.3: The stochastic field is sampled on the Gauss integration points and the values are employed for the computation of the FE matrices

the FE problem. Therefore is considered a non-intrusive procedure. The process is repeated for all layers using their respective random field at each, as they are modelled independently with the LW approach.

4.3 Monte Carlo analysis for uncertainty quantification

In the previous sections it has been stated that, due to its nature, uncertainty can be modelled as a random field whose values, in our case, are related to the stochastic parameter ξ_i . To quantify the effect of uncertainty in the buckling performance of a VSC's plate, a Monte Carlo analysis is proposed.

According to this method, many deterministic simulations are performed, employing in each of them a different random set $\xi_i(\omega)$. As a reminder, ω is a variable associated to each random experiment in the space of random events Ω . The domain Ω has to be sufficiently large (commonly between 10^3 and 10^6 simulations) to allow a clear detection of uncertainty effects on the outputs. Then, these outputs from all simulations are gathered and studied altogether by means of statistical analysis.

Specifically, the stages that are going to be followed in each simulation are the

following:

1. A stochastic field $\Psi_{FVF}(\alpha, \beta; \omega)$ is obtained throughout the computation of a $\xi_i(\omega)$ new value.
2. FE matrices take into account the material properties obtained with the regression equations. The mechanical properties of the mesh elements are defined in each simulation without modifying the model, just modifying inputs, in a non-intrusive way.
3. A simulation is carried out and the different outputs of interest are stored. Stress and strain fields, critical buckling loads and its correspondent deformation modes are some of the outputs which are going to be investigated.
4. The process is repeated until the total number of simulations is reached. Stored data from all simulations is studied at the end of the Monte Carlo analysis.

At the conclusion, a statistical analysis is carried out. The usually employed statistical tools for this matter are histograms and PDFs. The first one corresponds to a graphical representation of data using bars, whose lengths indicate the frequency magnitude of a discrete value. On the other hand, PDFs describe the probability for the different output values.

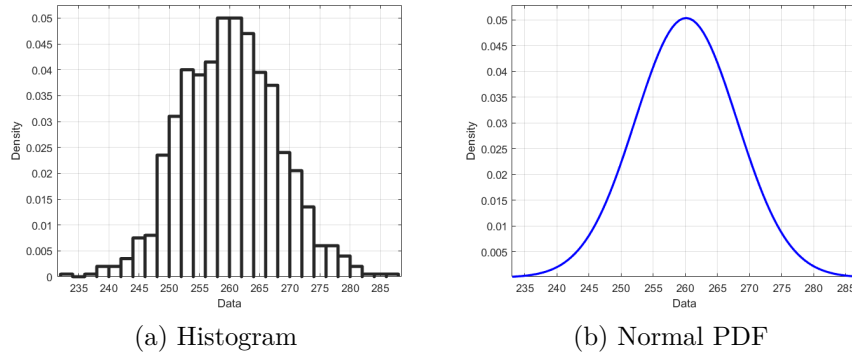


Figure 4.4: Representation of an histogram and PDF of a normal distribution

In this study, due to the Gaussian nature of the stochastic field and the linearity of the problem, the analysis outputs are expected to behave as a normal distribution. Therefore, some parameters of interest obtained from the outcomes are the mean value of the distribution, μ , and its standard deviation, σ .

4.3.1 Polynomial Chaos Expansion

Polynomial chaos expansion (PCE) is a probabilistic method which substitutes a computational model and provides a good approximation of its output by means of orthogonal polynomials. This method is well known due to its ability to generate a good representation of the model output variability according to random inputs. Therefore it has been applied in a broad range of application fields as solid mechanics, fluid flows or thermal sciences [36].

With PCE, an output is defined as a function of the independent random vector \mathbf{X} , whose components are independent and can be described by a PDF, f_X . The PCE metamodel, named \mathcal{M} , is considered to have finite variance, satisfying the following expression:

$$\mathbb{E}[Y^2] = \int_{\mathcal{D}_X} \mathcal{M}^2(\mathbf{x}) f_X(\mathbf{x}) d\mathbf{x} < \infty \quad (4.12)$$

where Y is the model output which can be approximated by a series of multivariate polynomials $\Psi_\alpha(\mathbf{X})$ orthonormal with respect to f_X as follows:

$$Y = \mathcal{M}(\mathbf{X}) = \sum_{\alpha \in \mathbb{N}^M} y_\alpha \Psi_\alpha(\mathbf{X}) \quad (4.13)$$

in which y_α are the PCE coefficients and $\alpha \in \mathbb{N}^M$ corresponds to a multi-index for identifying the multivariate polynomials. The expansion is truncated for its realistic application, approximating the sum by a selected set of values, $\mathcal{A} \subset \mathbb{N}^M$:

$$\mathcal{M}(\mathbf{X}) \approx \mathcal{M}^{PC}(\mathbf{X}) = \sum_{\alpha \in \mathcal{A}} y_\alpha \Psi_\alpha(\mathbf{X}) \quad (4.14)$$

The multivariate polynomials are obtained as a product of univariate orthogonal polynomials in the following way:

$$\Psi_\alpha(\mathbf{x}) \stackrel{\text{def}}{=} \prod_{i=1}^M \phi_{\alpha_i}^{(i)}(x_i) \quad (4.15)$$

where subindex i identifies the input variable. The employed univariate polynomials satisfy:

$$\langle \phi_j^{(i)}(x_i), \phi_k^{(i)}(x_i) \rangle \stackrel{\text{def}}{=} \int_{\mathcal{D}_{X_i}} \phi_j^{(i)}(x_i) \phi_k^{(i)}(x_i) f_{X_i}(x_i) dx_i = \delta_{jk} \quad (4.16)$$

where indexes j and k are respectively the polynomial family and its degree. δ_{jk} is the Kronecker delta which was defined previously in Chapter 2, Equation (2.8). Due to its orthogonal relations, the multivariate polynomials have orthonormal properties too:

$$\langle \Psi_\alpha(\mathbf{x}), \Psi_\beta(\mathbf{x}) \rangle = \delta_{\alpha\beta} \quad (4.17)$$

According to PCE, different orthonormal polynomial families can be employed, depending on the random variable studied. The Askey scheme relates the random variable distributions with the appropriate polynomial family as follows:

Type of variable	Distribution	Orthogonal polynomials	$\psi_k(x)$ basis
Uniform	$1_{]-1,1[}(x)/2$	Legendre $P_k(x)$	$P_k(x)/\sqrt{\frac{1}{2k+1}}$
Gaussian	$\frac{1}{\sqrt{2\pi}}e^{-x^2/2}$	Hermite $H_{e_k}(x)$	$H_{e_k}(x)/\sqrt{k!}$
Gamma	$x^\alpha e^{-x} 1_{\mathbb{R}^+}(x)$	Laguerre $L_k^\alpha(x)$	$L_k^\alpha(x)/\sqrt{\frac{\Gamma(k+\alpha+1)}{k!}}$
Beta	$1_{]-1,1[}(x) \frac{(1-x)^\alpha (1+x)^\beta}{B(\alpha)B(\beta)}$	Jacobi $J_k^{a,b}(x)$	$J_k^{a,b}(x)/\mathfrak{J}_{a,b,k}$
			$\hat{\mathfrak{J}}_{a,b,k}^2 = \frac{2^{a+b+1}}{2k+a+b+1} \frac{\Gamma(k+a+1)\Gamma(k+b+1)}{\Gamma(k+a+b+1)\Gamma(k+1)}$

Table 4.1: Askey scheme relating random variable distributions with its correspondent polynomial family for PCE. Extracted from [37]

Specifically, Hermite polynomials will be employed in this study as the outputs are expected to behave as Gaussian distributions. In the PCE model for Gaussian distributions, the independent term of the expansion corresponds to the mean value of the distribution μ and the sum of the square power of the other coefficients coincides with its variance:

$$y_0 = \mu \quad \text{and} \quad \sum_{i=1} y_i^2 = \sigma^2 \quad (4.18)$$

More information about the application of PCE for uncertainty quantification can be found in [36, 37].

Chapter 5

Numerical results

This chapter presents all the results obtained from the performed FE analyses of VSC plates. The main outputs of the linearized buckling analysis which are going to be considered are the critical buckling loads, from now on referred as F_{cr_i} , together with their correspondent deformation modes and the stress and strain fields.

Firstly, Section 5.1.1 presents a verification of the micro-scale UC-problem process to obtain the homogenized material properties. The correct functioning of this process is verified throughout comparison with results extracted from the literature. Then, a similar process is carried out in Section 5.1.2, to verify the proper behaviour of the employed modeling techniques at the macro-scale. For this purpose, the buckling performance of VSC models is going to be investigated. The first buckling critical load, F_{cr1} , obtained in the study is going to be compared with the one obtained for the same VSC plate employing commercial software Abaqus.

Once this verification stage is concluded, a mesh convergence analysis is shown in Section 5.1.3, from which the final mesh of our model is obtained. In Section 5.2, the outputs for VSC models without defects are presented. Only six F_{cr_i} and their respective deformation modes are going to be included among the outputs. Later, a local field recovery is going to be computed from the global solution. The process is shown for UC located in a certain point of the structure and the local stress components will be plotted. Finally, the uncertainty analysis for the VSC plates is included in Section 5.3. The statistical data gathered from the Monte Carlo analysis outputs is presented and PCE is proposed as a time-saving option for the VSC uncertainty study.

5.1 Model verification

5.1.1 Micro-scale verification

First of all, the process to obtain the global homogenized properties from the UC-problem at the micro-scale is going to be verified. It is a very important aspect to check as these properties will be later taken into account to compute the stiffness properties of the mesh elements in our model. In order to verify this procedure, an example case found in the literature is going to be reproduced and then, the calculated outputs are going to be compared with the results obtained in the example. The example used as a reference is present in the work by A. G. de Miguel [32].

To proceed with the calculation of effective properties from the VSC UC-problem, MUL2-UC program is going to be employed with the help of its manual [38]. Firstly, it is necessary to indicate the material properties of the UC constituents. These fiber reinforcement and epoxy resin material properties are extracted from the literature example, as well as the UC geometry used in this verification study.

The UC geometry consists of a cubic cell as the one shown in Figure 3.2. The inner cylinder corresponds to the fiber reinforcement and the material surrounding it, to the epoxy matrix. For solving the UC-problem, MUL2-UC uses mapping functions to describe the exact geometry of the cross-section of the UC, which can be fully defined by the FVF parameter. This parameter establishes the surface percentage in the cross-section area for each component present on the UC. For example, a FVF value of 0.4 indicates that 40% of the UC cross-section area is occupied by fiber. Figure 5.1 shows the variation of fiber area with the FVF value.

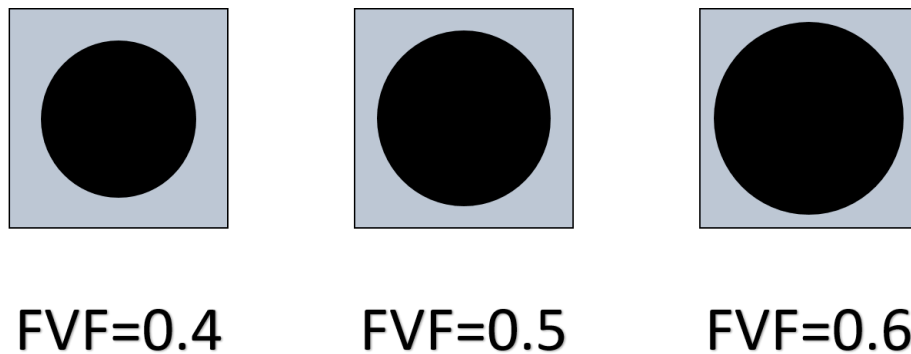


Figure 5.1: FVF parameter fully defines the geometry of the UC cross-section

Once the UC geometry is defined, the next step is introducing the material properties of both constituents as input in the program. These material properties

are listed on Table 5.1, whose values are expressed using the local reference system of the UC. The carbon fiber has orthotropic material properties, while the ones for the matrix are isotropic.

Fiber					
$E_{11}[GPa]$	$E_{22}[GPa]$	$G_{12}[GPa]$	$G_{23}[GPa]$	ν_{12}	ν_{23}
235	14	28	5.6	0.2	0.25
Matrix					
$E[GPa]$			ν		
4.8			0.34		

Table 5.1: Material properties of the fiber and the epoxy matrix, extracted from the example in [32]

In the example used for verification, the FVF value used to define the geometry of the UC is 0.6, therefore the fiber reinforcement occupies 60% of the UC cross-section surface. Then, the order of the HLE polynomial used for modeling the cross-section is decided. This parameter has an influence on the accuracy of the results. 8th-order HLE polynomials are going to be employed to ensure good accuracy in the calculus. All this data is introduced as input into the program, which now has all the needed parameters to proceed with the resolution of the UC-problem applying VAM. At the conclusion of the MSG method computation, the material effective properties which are obtained are listed on Table 5.2. These correspond to the homogenized UC with orthotropic properties, again expressed in its local reference system:

Effective UC material properties					
$E_{11}[GPa]$	$E_{22}[GPa]$	$G_{12}[GPa]$	$G_{23}[GPa]$	ν_{12}	ν_{23}
143.2	9.6	6.1	3.1	0.25	0.35

Table 5.2: Equivalent material properties for the homogenized UC

These obtained homogenized properties of the UC coincide exactly with the ones in the example from [32] in the literature, verifying that no mistakes are done during the computational process. These material properties are the ones that will be introduced into our VSC models in the forthcoming analyses.

5.1.2 Macro-scale verification

A verification process of the VSC models buckling performance at the macro-scale level is now going to be presented. In this work, two VSC plates are going to be investigated. Both of them are composed of four equal thickness plies but with different ply fiber orientations. The first one, from now on referred to as VSC A, has a fiber orientation within the plies described by expression $\theta = [0 \pm < 45, 0 >]_s$. On the other side, the second one, named VSC B, has a fiber orientation defined by expression $\theta = [90 \pm < 0, 45 >]_s$. Both VSCs have globally balanced fiber orientation designs and symmetric structures.

The two VSCs models have the same plate geometry and are composed of the same two material constituents for the matrix and fiber reinforcement. The stiffness matrices of the models mesh elements are computed taking into account the effective properties of the homogenized UCs at the micro-scale level. These were already computed in the previous section and can directly be taken from Table 5.2. These material properties are expressed in the local reference system of the UC and have to be rotated, for each mesh element, to the global reference system through rotation according to its respective fiber orientation angle.

The verification process will consist of carrying out a linearized buckling analysis to the VSC models and then, the analysis results will be verified through comparison with the ones obtained in the same analysis by the commercial software Abaqus. The buckling simulations will have the same boundary conditions and constraints for both VSCs. Figure 5.2 shows a drawing of the plate with the boundary conditions applied in the analysis. These conditions are the following:

1. The VSC plate has one of its edges clamped while the others are left free-to-deform.
2. On the opposite side of the clamped edge, a 1 N load is applied as a compression pressure distributed all over the edge surface.

On the other hand, the geometry of the VSC plates is described with the parameters listed on Table 5.3

VSC plate geometry		
a [m]	b [m]	one ply thickness [mm]
0.254	0.254	0.127

Table 5.3: Geometrical properties of the VSC plate

The buckling simulations are performed with different modeling techniques. In Table 5.4, the resulting F_{cr1} is reported for LW and ESL models, together with the

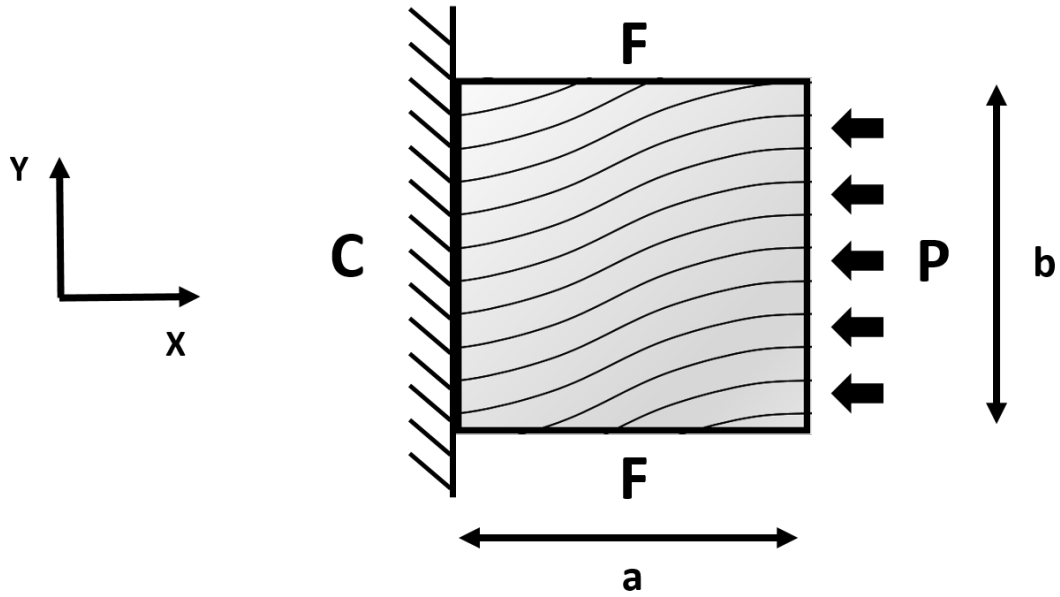


Figure 5.2: Plate with boundary conditions. F stands for free edge, C for clamped and P corresponds to the $1N$ distributed load

results obtained from Abaqus. For ESL, TE is employed with different polynomial degrees. A refined model mesh is used for the FE analysis. The table also includes the total degrees of freedom (DOF) of each model. Later, in Section 5.1.3, a mesh convergence analysis is carried out to find a proper mesh for the simulations which allows to get results with precision and reducing the computational time spent.

VSC A	Abaqus	LW	TE1	TE2	TE3
F_{cr1} [N]	141.9	142.2	114.4	148.8	146.6
VSC B	Abaqus	LW	TE1	TE2	TE3
F_{cr1} [N]	25	25.8	20.9	29.5	29.4
DOF	4056	18360	360	720	1200

Table 5.4: F_{cr1} values obtained by Abaqus and with the LW and ESL models

As it can be observed, the LW model provides a more accurate description of F_{cr1} than TE models, with similar values to the ones obtained by Abaqus, which is the most precise one. However, only LW models are going to be considered in this work as they allow to model uncertainty defects for each VSC ply independently,

at the meso-scale level.

Finally, the deformation shape of the first mode for the investigated models are shown in Figures 5.3 and 5.4. For both VSCs, the deformed shape is the same as for the Abaqus model, leading to the conclusion that the models are able to properly describe the buckling response of the VSC plates.

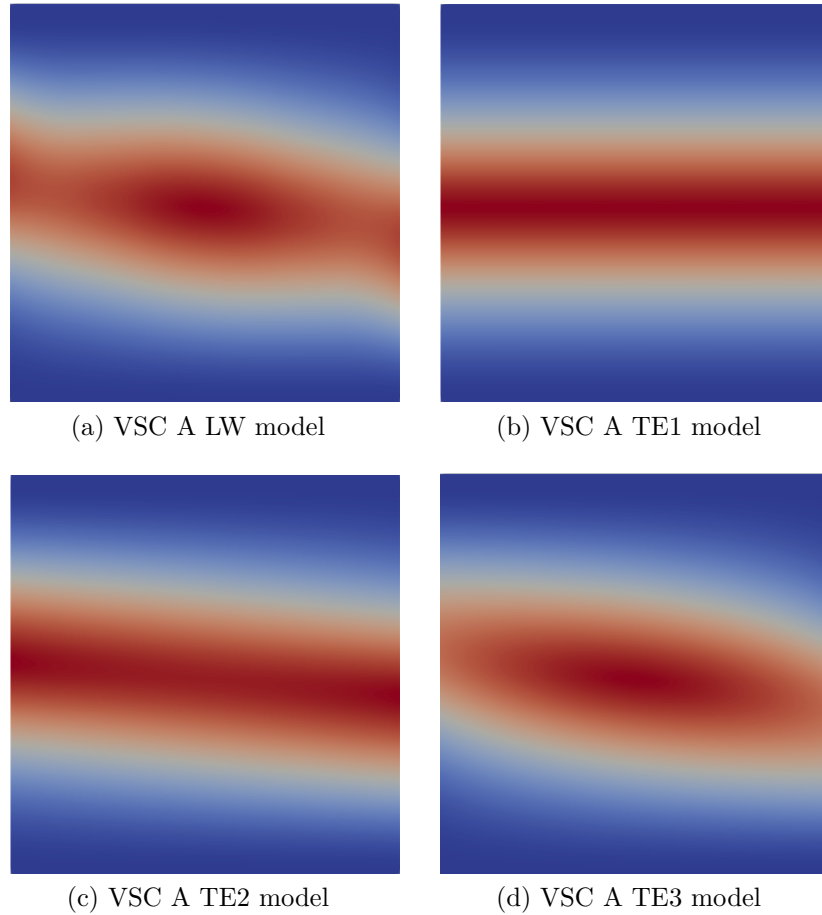


Figure 5.3: Comparison between the first deformation mode obtained with LW model and TE models for VSC A

Once the verification of the model is concluded, the next step is to perform a mesh convergence analysis. It is going to be presented in the next section.

5.1.3 Mesh convergence analysis

To select a proper meshing for the VSC, a mesh convergence analysis is carried out. This analysis consists of repeating the buckling linearized analysis with different

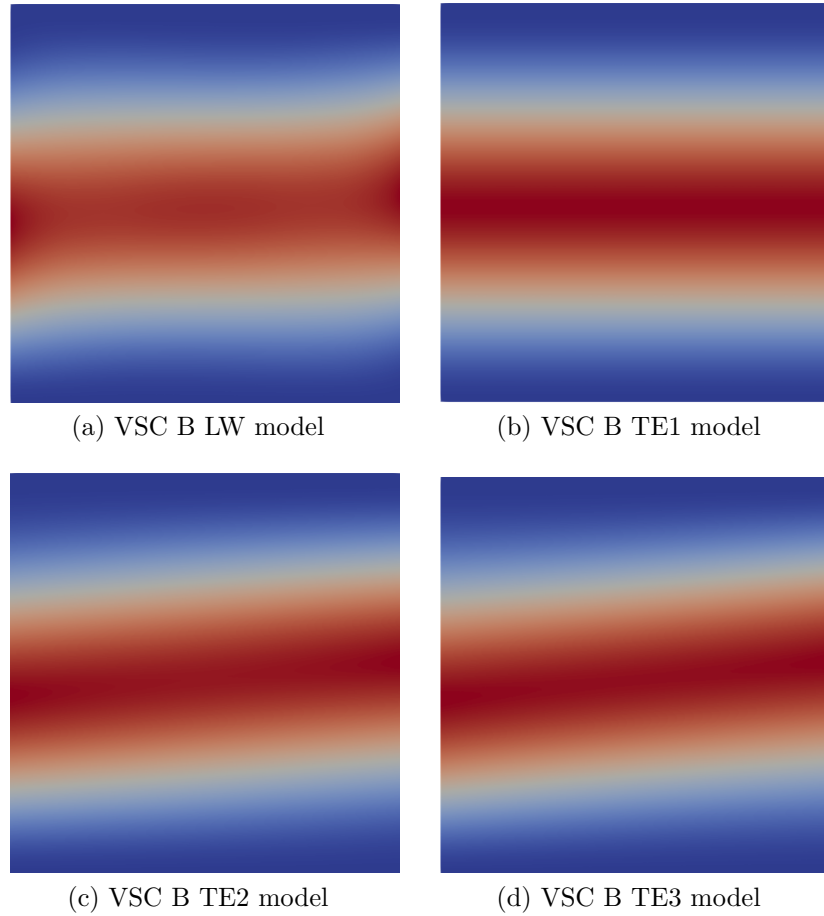


Figure 5.4: Comparison between the first deformation mode obtained with LW model and TE models for VSC B

mesh refinements. It starts with a simple mesh and its refinement is gradually increased with each simulation. The process continues until convergence is reached for the first six F_{cr_i} values. As in the previous section, the material properties assigned to the VSC models are listed in Table 5.2. After each simulation, the obtained values of F_{cr_i} , the elapsed time and the number of degrees of freedom (DOF) will be stored. In this analysis, not only the convergence of F_{cr_i} is going to be relevant, but also the computational cost is an important aspect to take into account when selecting the best mesh for the simulations.

The model geometry and the boundary conditions of the analysis are the same as in the previous Section (see Table 5.3 and Figure 5.2). Only the pristine structure of the plate is studied in the mesh convergence analysis. Uncertainty effects on the micro-scale are not modelled and the FVF value remains constant and equal

to 0.6. The material properties of the elements are oriented according to the fiber orientation within the ply and a LW approach is employed to define the model.

For the sake of brevity, only the mesh convergence analysis of VSC A is here presented. The meshing strategy adopted for the model is based on B4 and L9 Lagrangian elements. B4-elements are employed for describing the behaviour in the longitudinal x -direction, and L9-elements for the cross-section expansion. In this study, it is decided to model the cross-section of each VSC ply with only one element in the z -direction. Therefore, during the analysis, the mesh refinement will only be increased by increasing the element number along the y -direction.

The first part of the mesh convergence analysis studies the convergence of F_{cr_i} when varying the number of B4-elements in the longitudinal x -direction. A prime analysis is performed by setting the number of L9-elements in each ply's cross-section to six. As the studied VSC is composed of four layers, there are a total of 24 L9-elements on the plate's cross-section expansion. Then, the number of B4-elements in the mesh along the x -direction is progressively increased in each simulation until the convergence of F_{cr_i} . The convergence analysis results for the x -direction are presented in Figure 5.5.

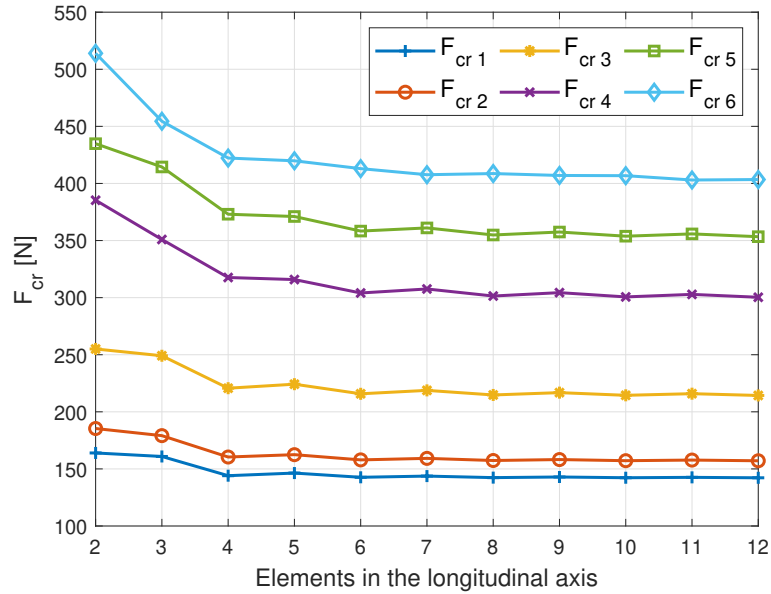


Figure 5.5: Convergence of F_{cr_i} when varying the number of B4-elements along the longitudinal dimension of the VSC plate A

Secondly, the same analysis is again performed for the cross-section expansion. Setting to twelve the total number of B4-elements in the x -direction, and varying the number of L9-elements composing the cross-section. The process starts with

one L9-element in each ply's yz -section. The buckling simulations are performed, gradually increasing by one the number of L9-elements per ply in each step, until the convergence of the F_{cr_i} . Figure 5.6 shows the convergence of F_{cr_i} during the analysis .

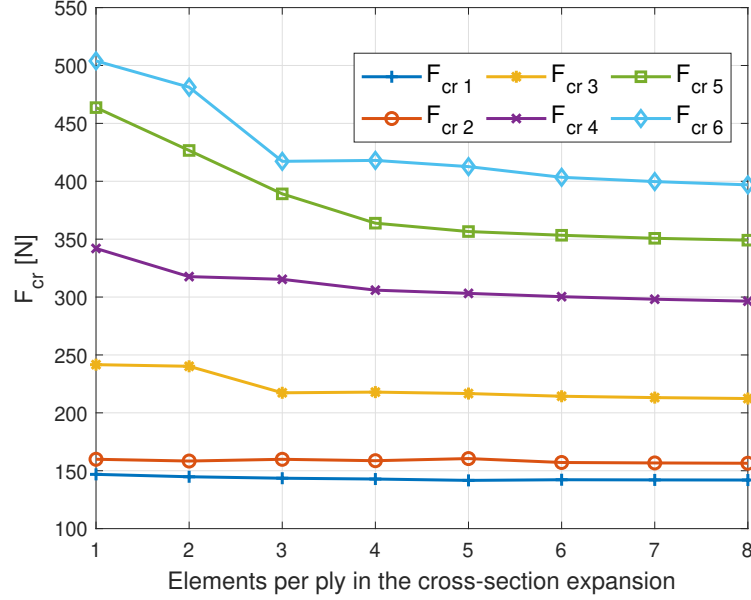


Figure 5.6: F_{cr} convergence analysis varying the quantity of L9-elements in the cross-section of each ply of VSC A

In Figures 5.5 and 5.6, it can be observed that, after some fluctuations, the F_{cr_i} converge to the same values in each figure and for each load. A more refined mesh leads to more accuracy but also increases the computational cost of the model, obtaining larger simulation times. In order to properly select the best meshing for the model, it is important to consider not only the precision but also the computational cost.

Data including the DOF and the elapsed time of each simulation is presented in Table 5.5. As the elapsed time depends on the CPU employed for the analysis, time values are divided by t_{min} , which is the value of the minimum time needed for the most basic simulation performed. This way, time is presented qualitatively.

Taking into account all the gathered information, the numerical mesh which is adopted for modeling the VSC is constituted by twelve B4-elements on the x -direction and six L9-elements on each ply transverse yz -section. This meshing provides good precision without an excessive computational cost. Some details of the final mesh are illustrated in Figure 5.7.

Mesh convergence x -direction				
B4 elements x -direction	L9 elements on each ply cross-section	DOF	Elapsed time t_i/t_{min}	
2	6	3510	1.37	
3	6	4563	1.84	
4	6	5616	2.32	
5	6	6669	2.76	
6	6	7722	3.34	
7	6	8775	3.71	
8	6	9828	4.16	
9	6	10881	4.66	
10	6	11934	5.13	
11	6	12987	5.66	
12	6	14040	6.05	
Mesh convergence yz -plane				
B4 elements x -direction	L9 elements on each ply cross-section	DOF	Elapsed time t_i/t_{min}	
12	1	3240	1	
12	2	5400	1.97	
12	3	7560	3	
12	4	9720	4.05	
12	5	11880	5.05	
12	6	14040	6.05	
12	7	16200	6.92	
12	8	18360	8.03	

Table 5.5: DOF and elapsed time of the performed buckling simulations in the mesh convergence analysis

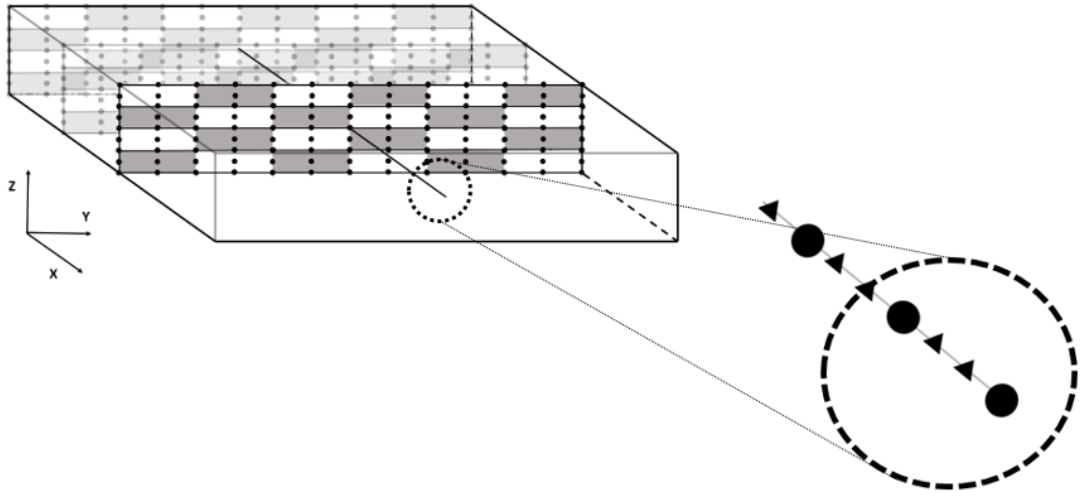


Figure 5.7: Final mesh with six L9-elements per layer and detail of a B4-element in the longitudinal dimension of the VSC plate

Final Mesh		
Total B4-elements	Total L9-elements per ply	DOF
12	6	14040

Table 5.6: Final mesh for the VSC model

5.2 Pristine model analysis

Once the modeling techniques employed in this study have been validated, and prior to the introduction of uncertainty affecting the FVF parameter in the model, the two VSCs are subjected to the analysis defined in the previous sections (see Figure 5.2). Again the material properties are obtained from the UC-problem of Section 5.1.1, and the employed numerical mesh is the one resulting from the mesh convergence analysis of Section 5.1.3. In this section, the uncertainty effects are not included yet in the model and only the pristine structure performance is going to be here studied. Firstly, this section is going to present the global stress and strain fields obtained from the static solution of the problem. Then, the buckling linearized analysis results will be shown. These results include the first six F_{cr_i} and their respective structure deformation modes. At last, a local stress field recovery is going to be performed for both VSCs.

5.2.1 Static solution

The first step of the analysis is to compute the static solution for the defect-free VSCs under investigation. The global stress and strain fields are obtained for all points in the plate structure. However, in this study, it has been decided to show these field values along a specific line along the z -direction, named s . Figure 5.8 shows the location of line s , whose (x, y) coordinates are $(0, 0)$. All field values are represented versus $2z/h$, being h the total thickness of the VSC plate.

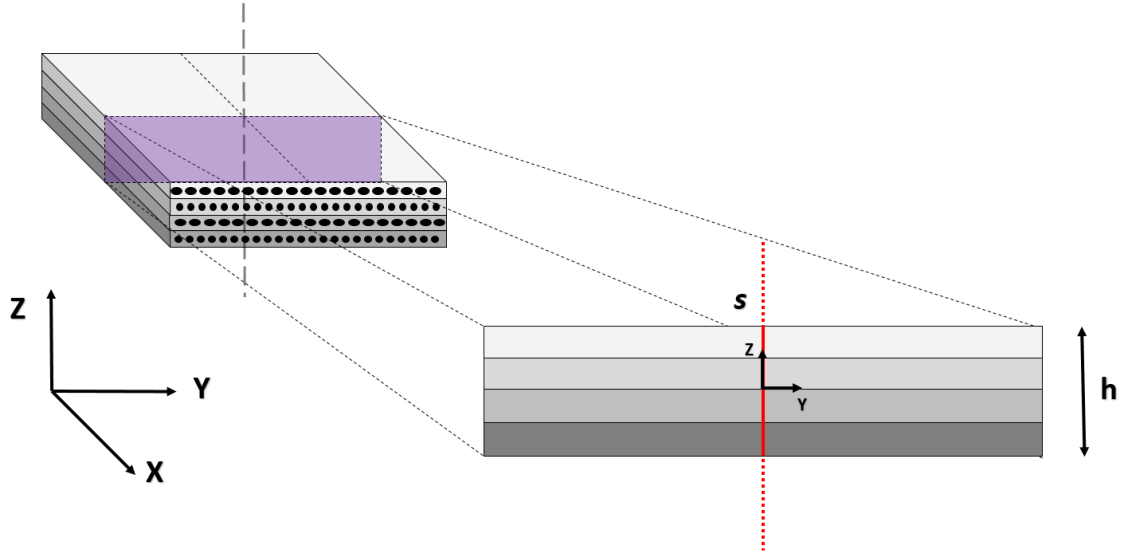
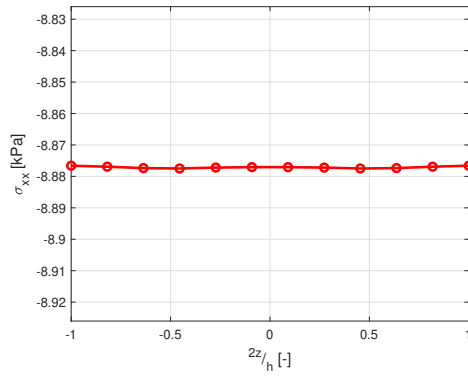
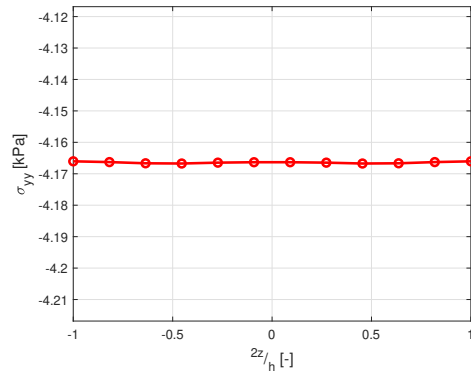


Figure 5.8: Stress and strain fields are presented along line s

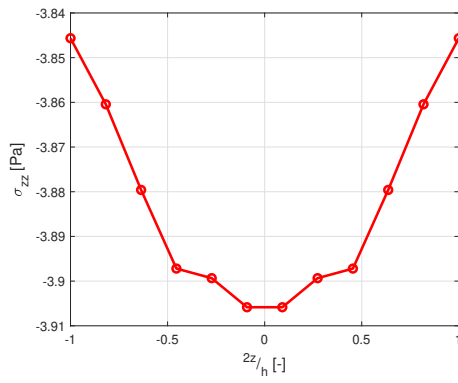
The obtained stress and strain field values for VSC A are respectively plotted in Figure 5.9 and Figure 5.10. On the other hand, the stress and strain field values for VSC B are the ones shown in Figure 5.11 and Figure 5.12.



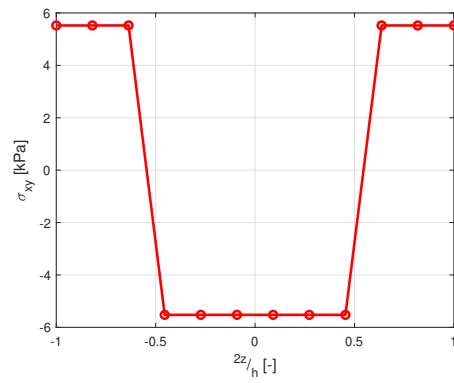
(a) VCS A σ_{xx}



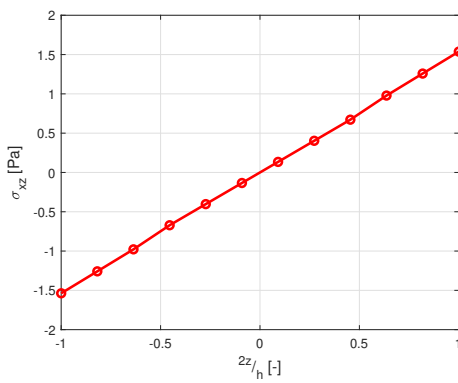
(b) VCS A σ_{yy}



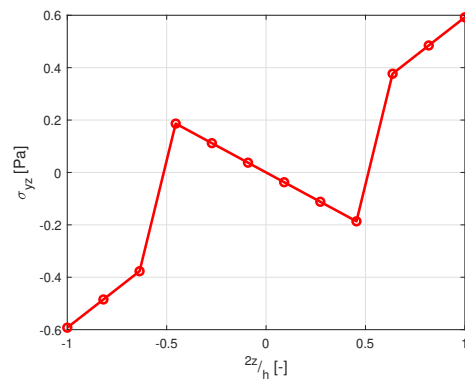
(c) VCS A σ_{zz}



(d) VCS A σ_{xy}

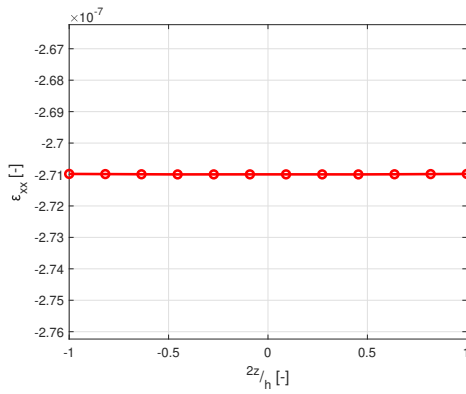


(e) VCS A σ_{xz}

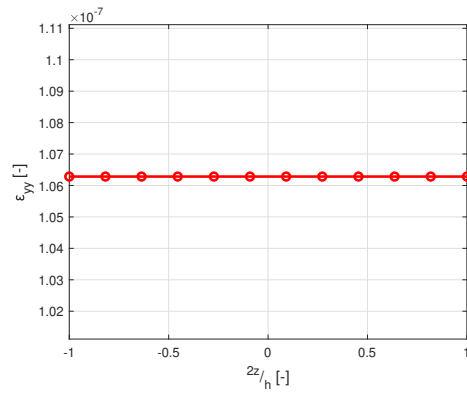


(f) VCS A σ_{yz}

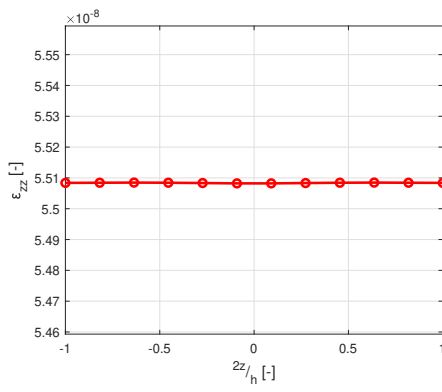
Figure 5.9: Stress tensor representation along line s for VCS A



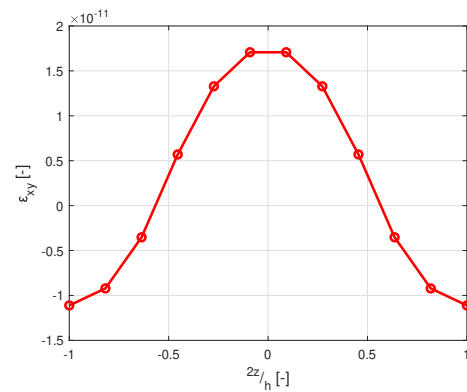
(a) VSC A ε_{xx}



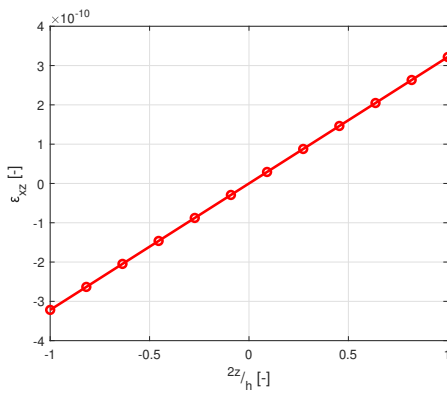
(b) VSC A ε_{yy}



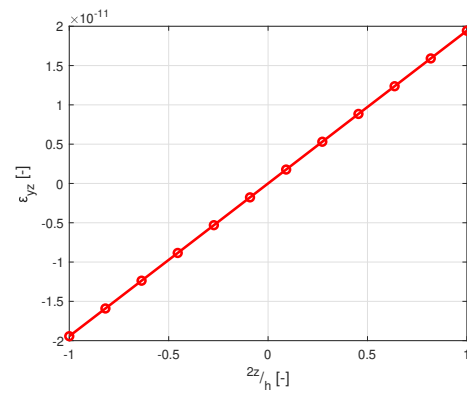
(c) VSC A ε_{zz}



(d) VSC A ε_{xy}



(e) VSC A ε_{xz}



(f) VSC A ε_{yz}

Figure 5.10: Strain tensor representation along line s for VSC A

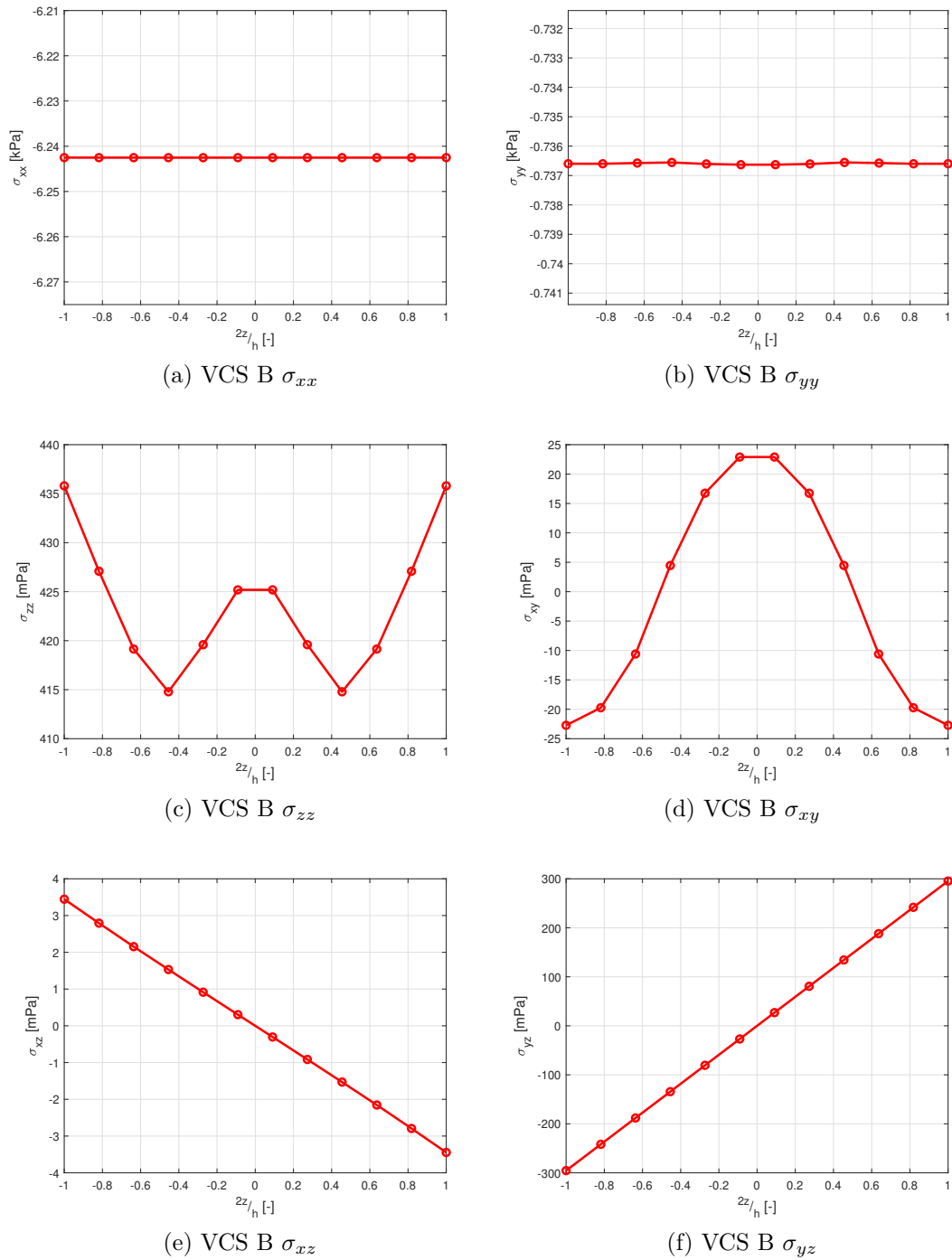
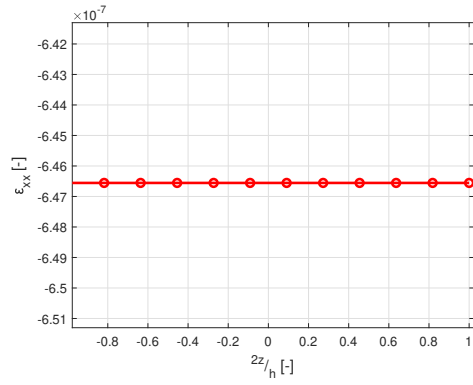
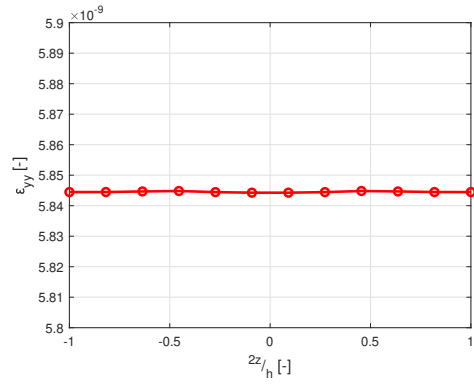


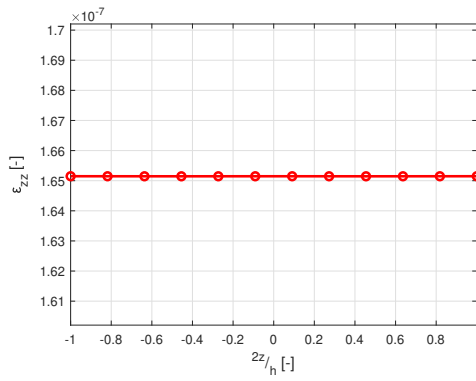
Figure 5.11: Stress tensor representation along line s for VCS B



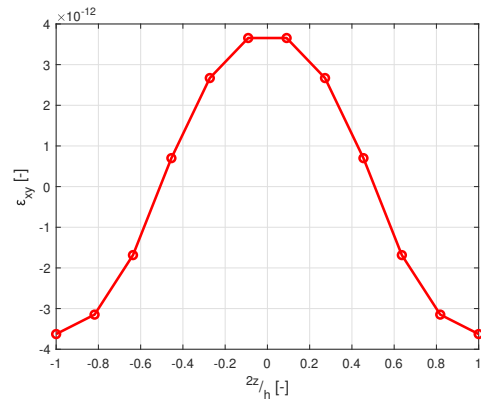
(a) VSC B ε_{xx}



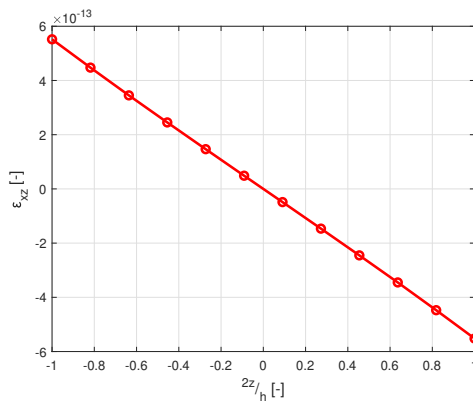
(b) VSC B ε_{yy}



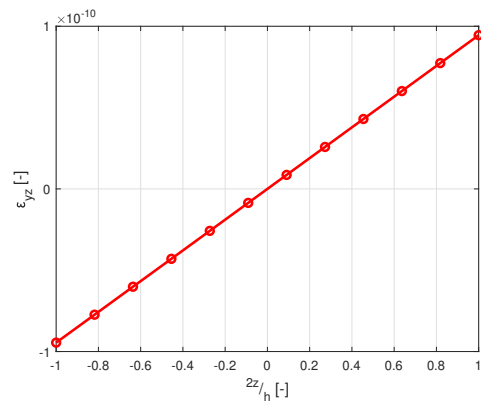
(c) VSC B ε_{zz}



(d) VSC B ε_{xy}



(e) VSC B ε_{xz}



(f) VSC B ε_{yz}

Figure 5.12: Strain tensor representation along line s for VSC B

5.2.2 Buckling analysis

Once the static solution is computed, the next step consists of performing the linearized buckling analysis. The buckling performances of both VSCs pristine models are here analyzed. The outputs which are going to be presented are the first six F_{cr_i} for both VSCs, as well as their respective deformation modes. These last give dimensionless information about the deformed structure shape for each load.

The different F_{cr_i} values obtained for VSC A are listed on Table 5.7 and their correspondent deformation modes are shown in Figure 5.13.

VSC A	1st	2nd	3rd	4th	5th	6th
$F_{cr_i}[N]$	142.2	157.1	214.3	300.3	353.4	403.5

Table 5.7: F_{cr_i} of the pristine model of VSC A

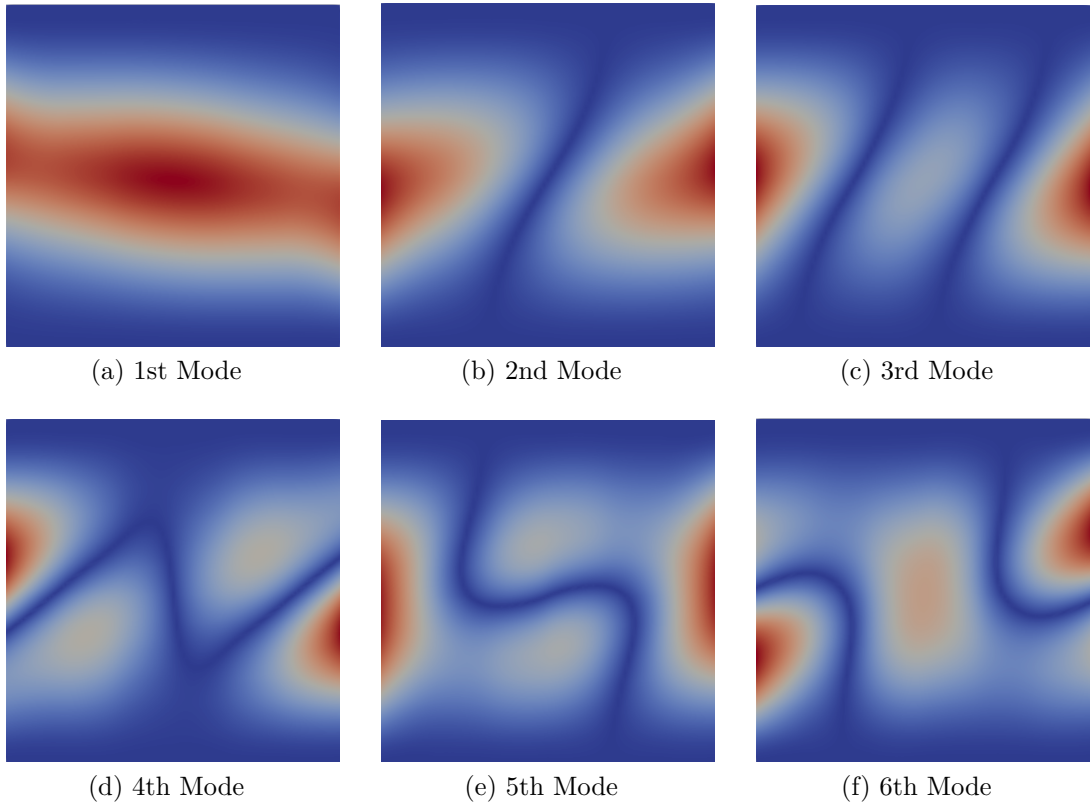


Figure 5.13: Buckling deformation shape modes for VSC A

On the other hand, the same results are presented for VSC B. Its F_{cr_i} values obtained from the simulation are listed in Table 5.8 and the deformation modes, corresponding to these critical loads, are presented in Figure 5.14.

VSC B	1st	2nd	3rd	4th	5th	6th
$F_{cr_i}[N]$	25.8	47.4	59.2	78.4	107.2	127.1

Table 5.8: F_{cr_i} of the pristine model of VSC B

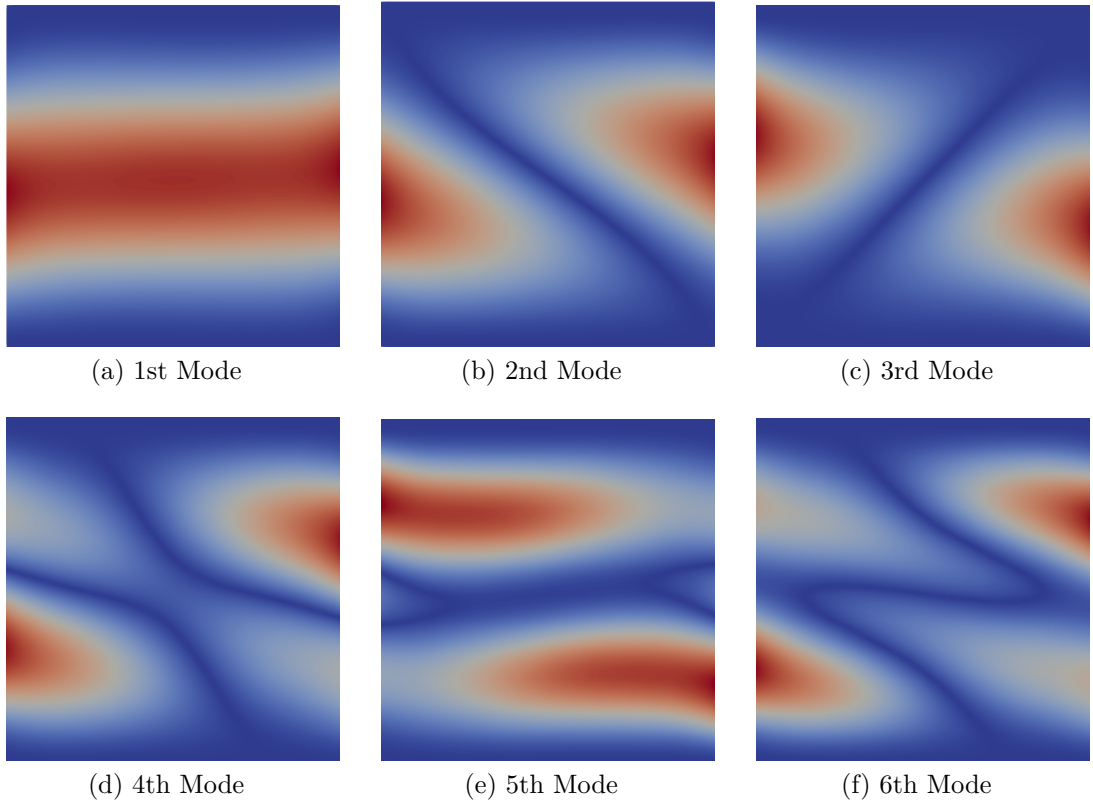


Figure 5.14: Buckling deformation shape modes for VSC B

Observing the results of the two VSCs, one can relate that there are significant differences between the buckling performance of plates A and B. As the loads applied in the analysis are the same for both, this fact can only be due to the different fiber orientations of each VSC. This event demonstrates the great importance of this factor in the mechanical response of the AFP manufactured parts. In a real case, it would be very important to properly design the fiber orientation of the VSC in order to achieve the most advantageous component buckling performance.

In Figure 5.15, a comparison between the F_{cri} values of both VSCs is shown. It is possible to observe how VSC A clearly outperforms VSC B in matters of buckling performance.

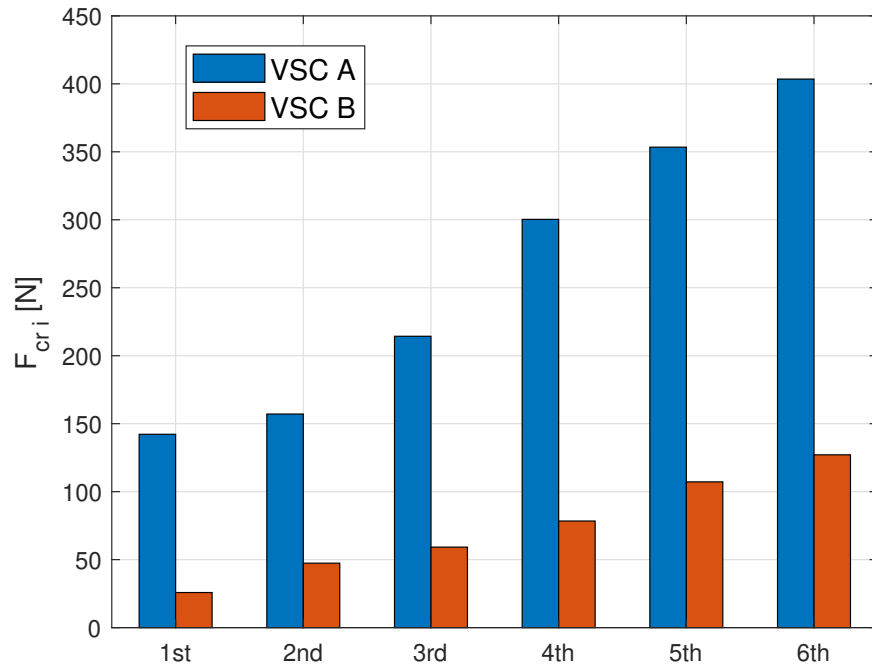


Figure 5.15: F_{cr} comparison between VSC A and B

5.2.3 Micro-scale field recovery

After the static solution of the problem has been calculated, it is possible to proceed with the dehomogenization process of the UC-problem. The micro-scale stress field can be computed from the macro-scale strain field. In this case, the method will be applied to a UC located in point C . This point belongs to the line s , and its dimensionless position coordinates are $2z/h = 0.75$. It corresponds exactly to the middle point of the VSC top layer as indicated in Figure 5.16.

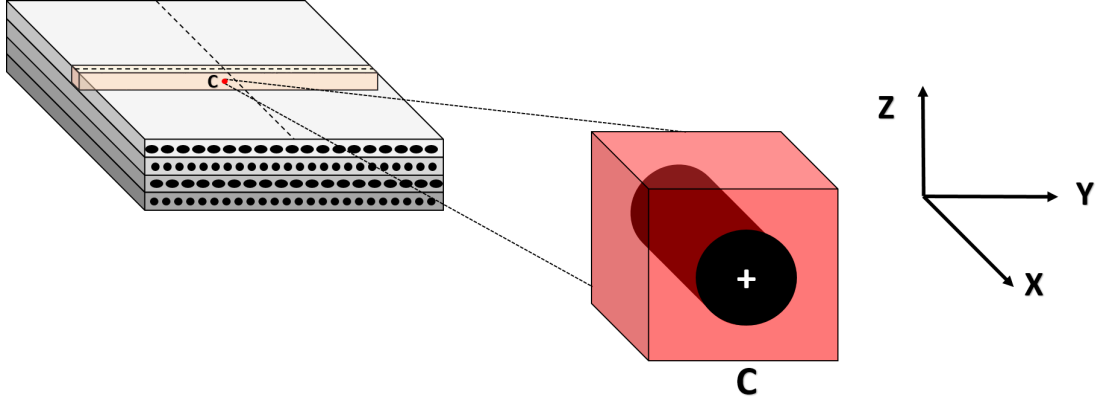


Figure 5.16: The UC under investigation belongs to the top layer of the VSC. It is located in the middle point of the ply.

The global strain tensor components, in the position of point C and expressed in the local reference system of the fiber, are obtained from the static solution of the problem and its values are listed, for both VSCs, in Table 5.9.

	ε_{11}	ε_{22}	ε_{33}	ε_{12}	ε_{13}	ε_{23}
VSC A	$-8.2 \cdot 10^{-8}$	$-8.2 \cdot 10^{-8}$	$5.5 \cdot 10^{-8}$	$-3.8 \cdot 10^{-7}$	$1.7 \cdot 10^{-10}$	$1.6 \cdot 10^{-10}$
VSC B	$-6.5 \cdot 10^{-7}$	$5.8 \cdot 10^{-9}$	$1.6 \cdot 10^{-7}$	$2.4 \cdot 10^{-12}$	$6.6 \cdot 10^{-10}$	$-7 \cdot 10^{-11}$

Table 5.9: Static solution strain field in point C , in the fiber local reference system, for VSCs A and B

Then, the dehomogenization process is applied and the local stress field is computed independently for the two material constituents present in the VSCs: the fiber reinforcement and the epoxy matrix. Figure 5.17 shows the stress distribution over the UC expressed in the local reference system of the cell. All components of the stress field are presented for both VSCs A and B together.

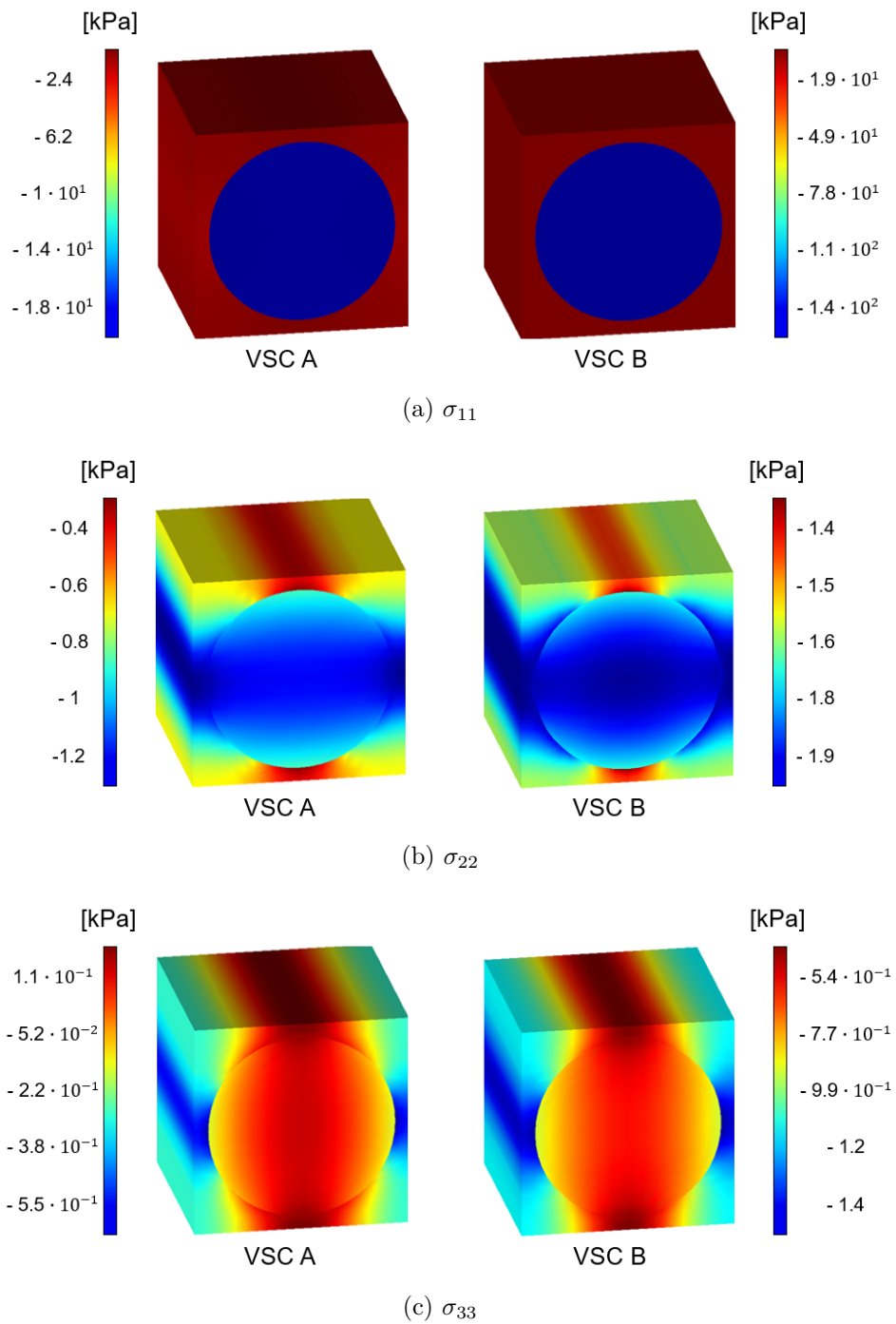
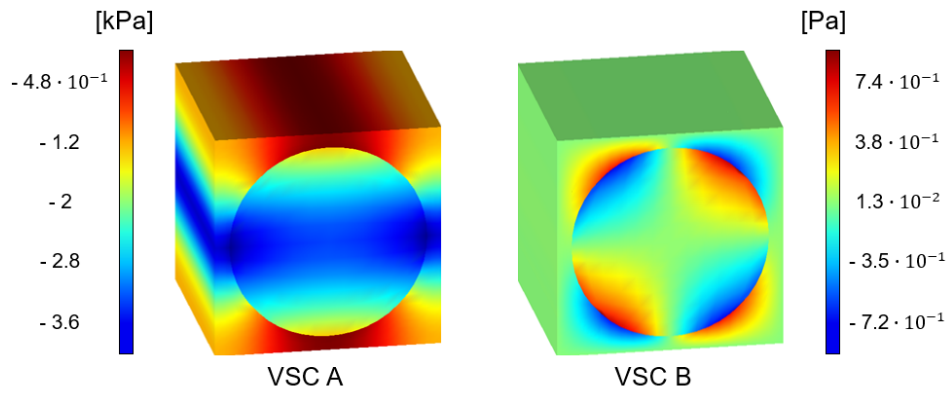
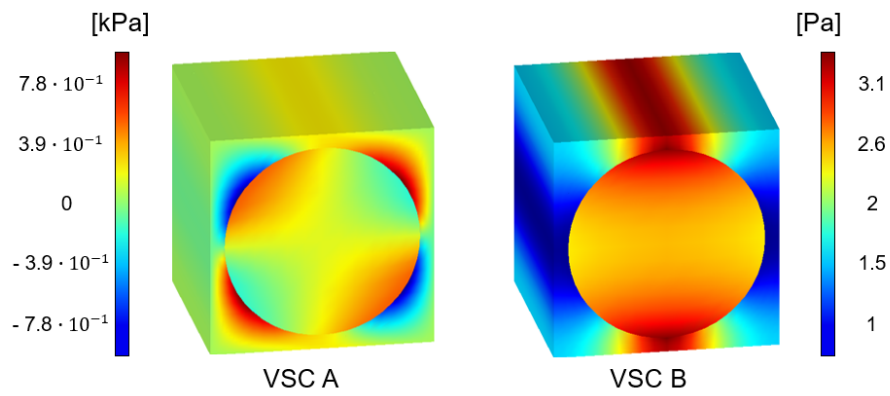


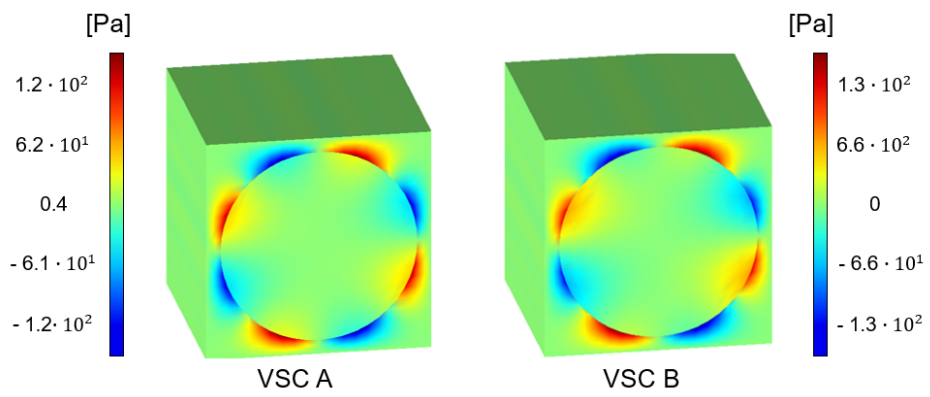
Figure 5.17: UC local stress field recovery



(d) σ_{12}



(e) σ_{13}



(f) σ_{23}

Figure 5.17: UC local stress field recovery

5.3 Uncertainty Analysis

In the previous sections, the mechanical performance of the VSC plates has been studied without taking into account uncertainty effects. All simulations were carried out following a deterministic approach, in which the FVF remained always constant. Now, uncertainty effects are going to be introduced in the study, applying stochastic methods. This section presents a sensitivity study of the VSCs mechanical response to the effects of uncertainty leading to variations in the FVF parameter. In order to be able to quantify the uncertainty effect, many deterministic analyses are performed by means of a Monte Carlo analysis. In each simulation, a different random field determines the FVF parameter for the UC-problem. However, to avoid repeating the MSG method computation for each analysis, polynomial expressions are obtained through a regression analysis of the UC-problem. The polynomials are able to express the material effective properties as a function of the FVF parameter. Therefore, the model material properties can be easily obtained, in a very time-saving process. This process to obtain the material properties of the homogenized UC is considered non-intrusive, as there is no need to change the formulation or redesign the model. This section will firstly present the polynomial expressions from the regression method. Later, the parameters which rule the generation of the stochastic fields are going to be decided. Finally, the results of the static solution and the linearized buckling analysis obtained through the Monte Carlo method are presented and studied.

5.3.1 Material regression functions

The material effective properties are calculated from the homogenization process for the UC-problem in the micro-scale. However, performing the micro-scale analysis in each Monte Carlo simulation will be very time-consuming, leading to excessively demanding analyses. Therefore, it is of our interest to obtain regression functions which directly compute these properties as a function of the uncertainty affected parameter, FVF. These material regression expressions are here obtained by means of a polynomial fitting procedure. The relationships between the dependent, the effective material properties, and the independent variable, the FVF value, are modelled as an n -th degree polynomial. The degree of the polynomial is selected to reduce the fitting error as much as possible. Figure 5.18 contains the plots of the effective material properties vs the FVF value in the fiber local reference system. The graphics include the polynomial fitting curve obtained by the regression analysis. These equations will be sampled in the Gauss point of the structure to obtain the material properties of the mesh elements, used for the computation of the stiffness matrices of the model.

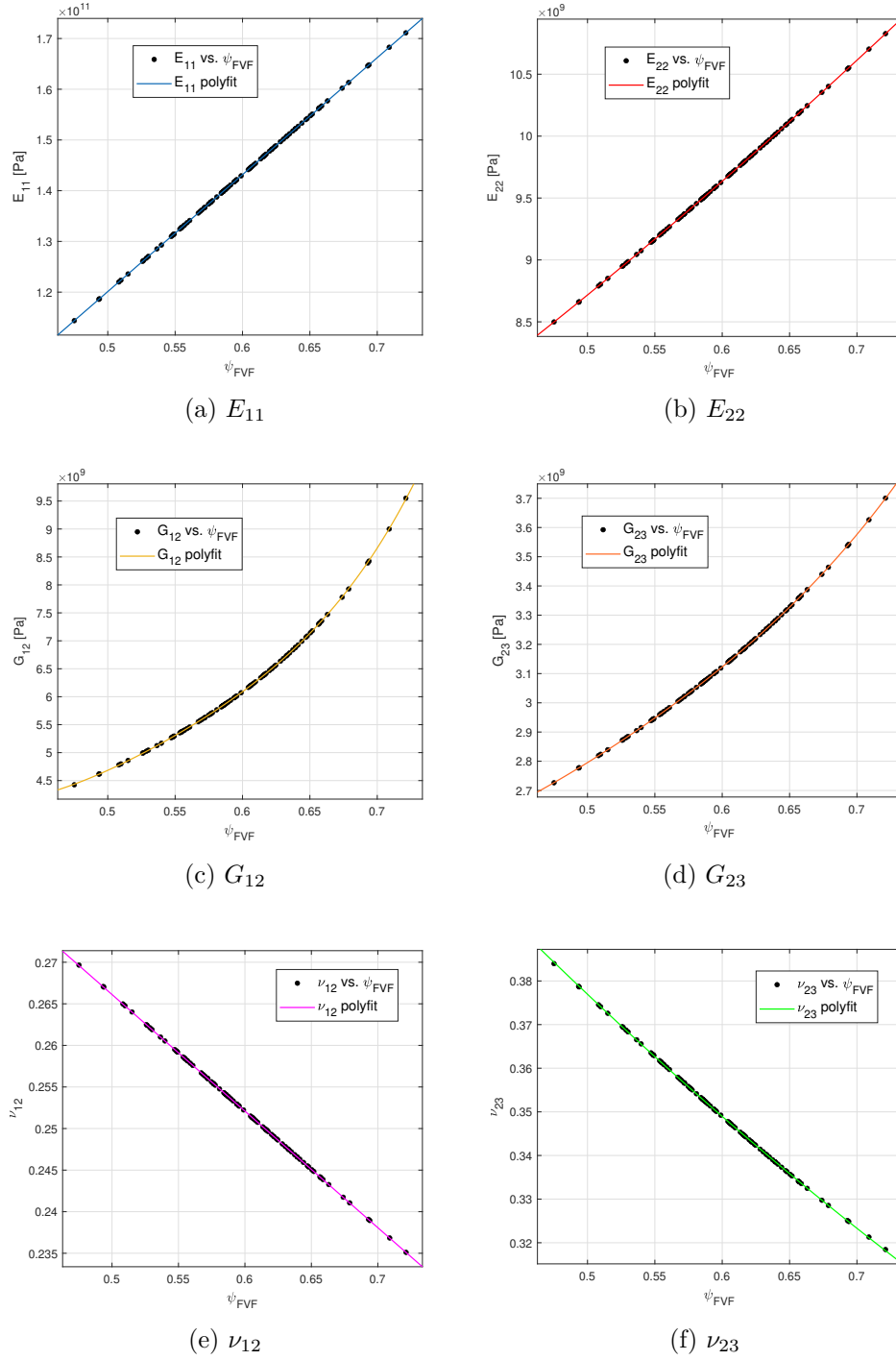


Figure 5.18: UC homogenized material properties as a function of ψ_{FVF} and polynomial fitting functions

5.3.2 Problem definition

The uncertainty-affected buckling analysis performed in this section has the same boundary conditions as the ones presented in Section 5.1.2, shown in Figure 5.2. The VSC plates geometry are described with the parameters of Table 5.3. Again both VSC plates only differ in the ply fiber orientation. To introduce uncertainty in the model, it is necessary to set the parameters which rule the generation of the random fields. Among these, it is necessary to define the field mean value, μ or $\bar{\Psi}_{FVF}$, and the standard deviation, σ . The nominal value assigned to $\bar{\Psi}_{FVF}$ is 0.6 and the standard deviation value is set to $\sigma = 0.05$. These values are decided based on the literature works (see [19]).

On the other hand, a total of $K = 10$ terms on the KLE are employed for the random field generation to ensure a proper convergence of the integral problem eigenvalues. Then, the dimensionless correlation lengths are set to $\bar{l}_x = \bar{l}_y = 1$. With these conditions and applying LHS for sampling the random ξ_i inputs, the random fields are fully defined. Figure 5.19 shows two examples of generated random fields with the above-mentioned parameters.

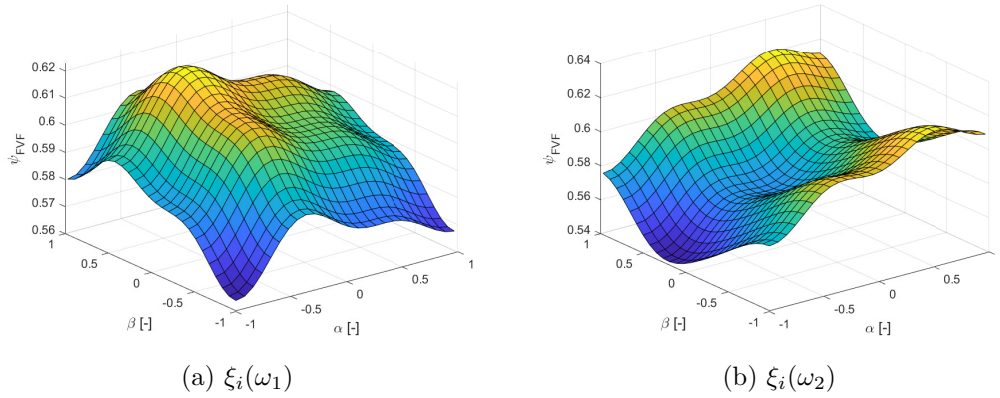


Figure 5.19: Stochastic fields with $(\bar{\psi}_{FVF}, \sigma) = (0.6, 0.05)$.

Finally, it is decided to perform a Monte Carlo analysis with $N = 10^3$ simulations for each VSC. The results which are going to be gathered in each simulation are the static solution stress and strain fields, and the F_{cr_i} from the linearized buckling analysis.

5.3.3 Stress and strain fields

At the conclusion of the Monte Carlo analysis, the stress and strain field values of the static solution are gathered. Here, the values of these fields are presented for the points belonging to the line s , which is the same as Section 5.1.2 (see Figure 5.8). Statistics are employed to present the gathered data. For each component of the strain and stress tensor, the following statistical data is shown:

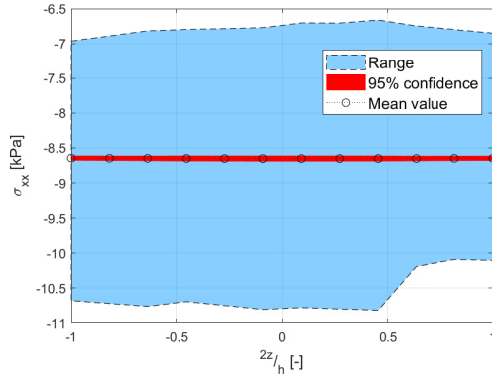
1. Mean value from the Monte Carlo simulations
2. 95% Confidence interval
3. Total range of values

Again the stress and strain components are plotted versus $2z/h$. The stress value representation obtained for VSCs A and B are presented respectively in Figure 5.20 and Figure 5.22. On the other hand, the strain field components for the two VSCs are shown in Figure 5.21 for VSC A, and Figure 5.23 for VSC B. All field components are expressed in the global reference system.

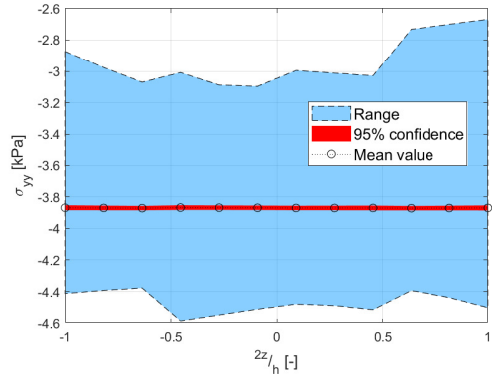
Finally, x , y and z stress components are presented in Table 5.10 for points belonging to line s . The data shows the mean value and, in parenthesis, the standard deviation.

$\frac{2z}{h}$ [-]	-1	-0.64	-0.27	0.27	0.64	1
VSC A σ_{xx} [kPa]	-8.645 (0.499)	-8.649 (0.531)	-8.651 (0.587)	-8.651 (0.589)	-8.650 (0.531)	-8.647 (0.498)
VSC A σ_{yy} [kPa]	-3.867 (0.223)	-3.870 (0.191)	-3.867 (0.197)	-3.869 (0.200)	-3.870 (0.191)	-3.868 (0.225)
VSC A σ_{zz} [Pa]	-6.611 (1.312)	-6.629 (0.863)	-6.634 (0.566)	-6.650 (0.582)	-6.664 (0.866)	-6.666 (1.316)
VSC B σ_{xx} [kPa]	-6.192 (0.240)	-6.195 (0.242)	-6.222 (0.271)	-6.204 (0.251)	-6.216 (0.236)	-6.217 (0.240)
VSC B σ_{yy} [kPa]	-0.704 (0.189)	-0.707 (0.162)	-0.707 (0.143)	-0.714 (0.142)	-0.715 (0.156)	-0.718 (0.182)
VSC B σ_{zz} [kPa]	0.441 (1.772)	0.401 (1.159)	0.411 (0.622)	0.382 (0.621)	0.321 (1.177)	0.317 (1.790)

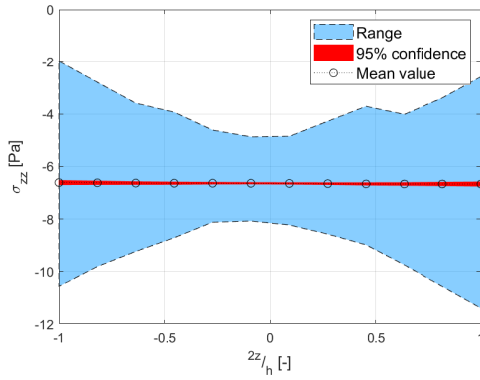
Table 5.10: Mean value and standard deviation (in parenthesis) for the stress field values along line s



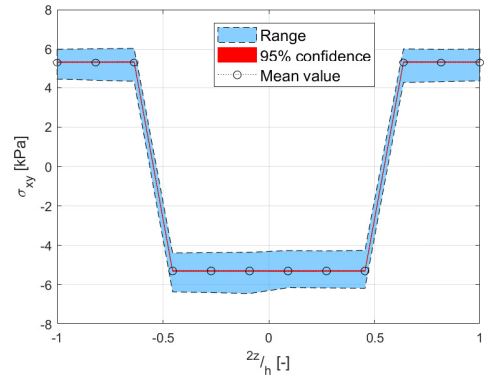
(a) VSC A σ_{xx}



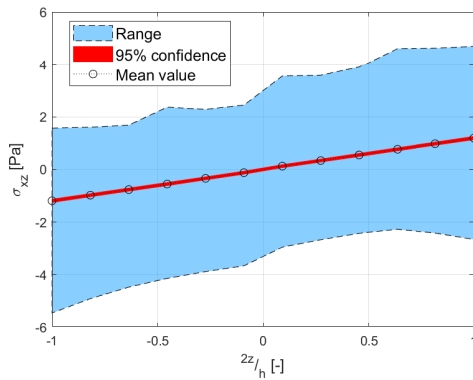
(b) VSC A σ_{yy}



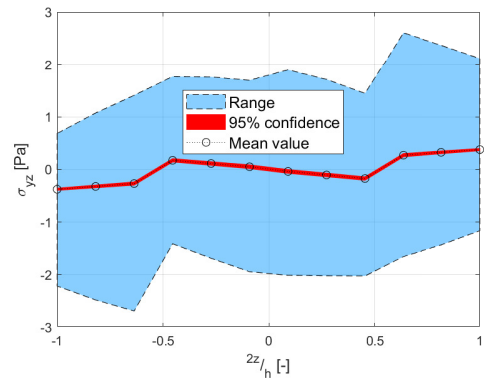
(c) VSC A σ_{zz}



(d) VSC A σ_{xy}



(e) VSC A σ_{xz}



(f) VSC A σ_{yz}

Figure 5.20: Stress tensor representation along line s for VSC A

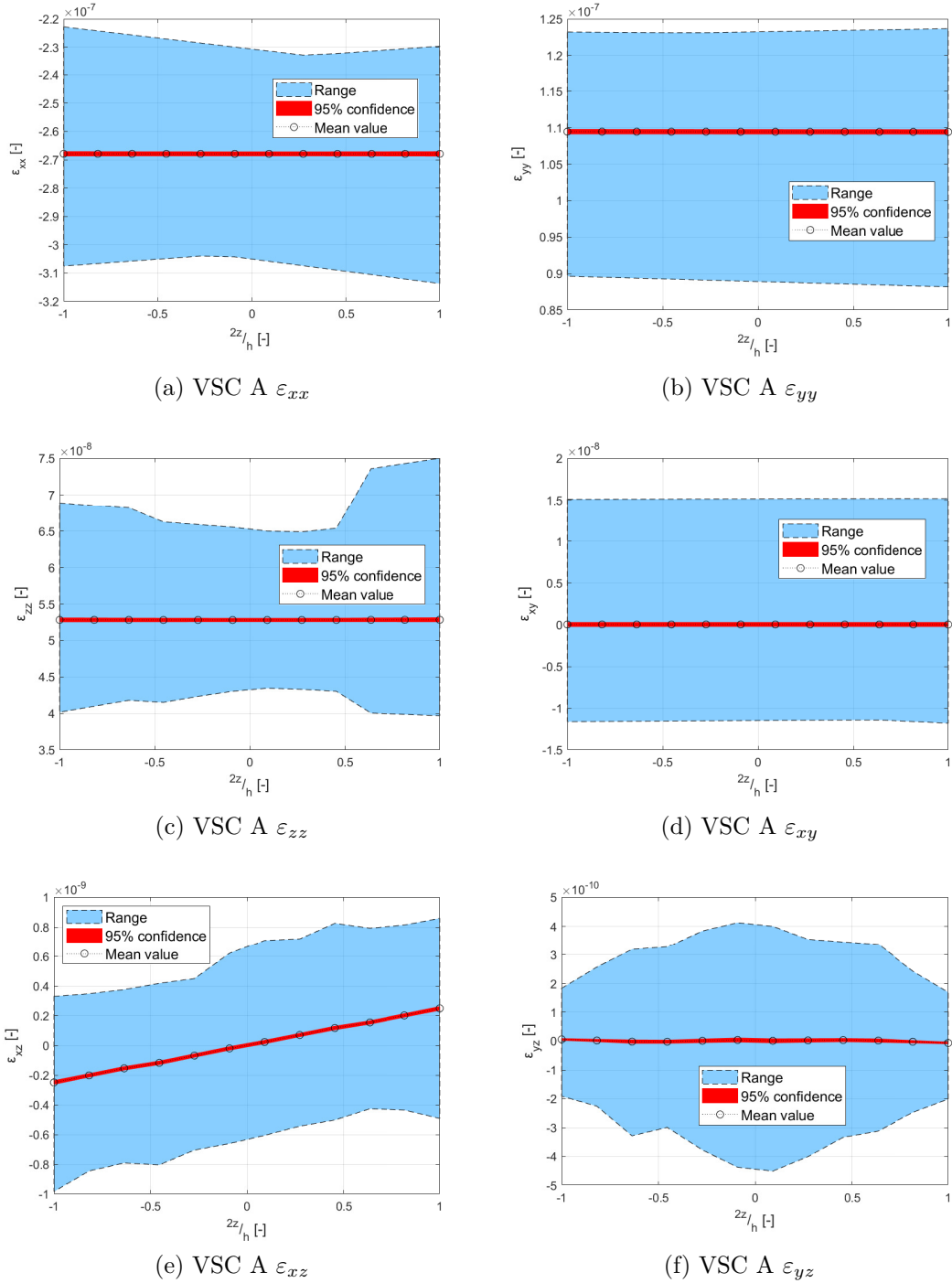


Figure 5.21: Strain tensor representation along line s for VSC A

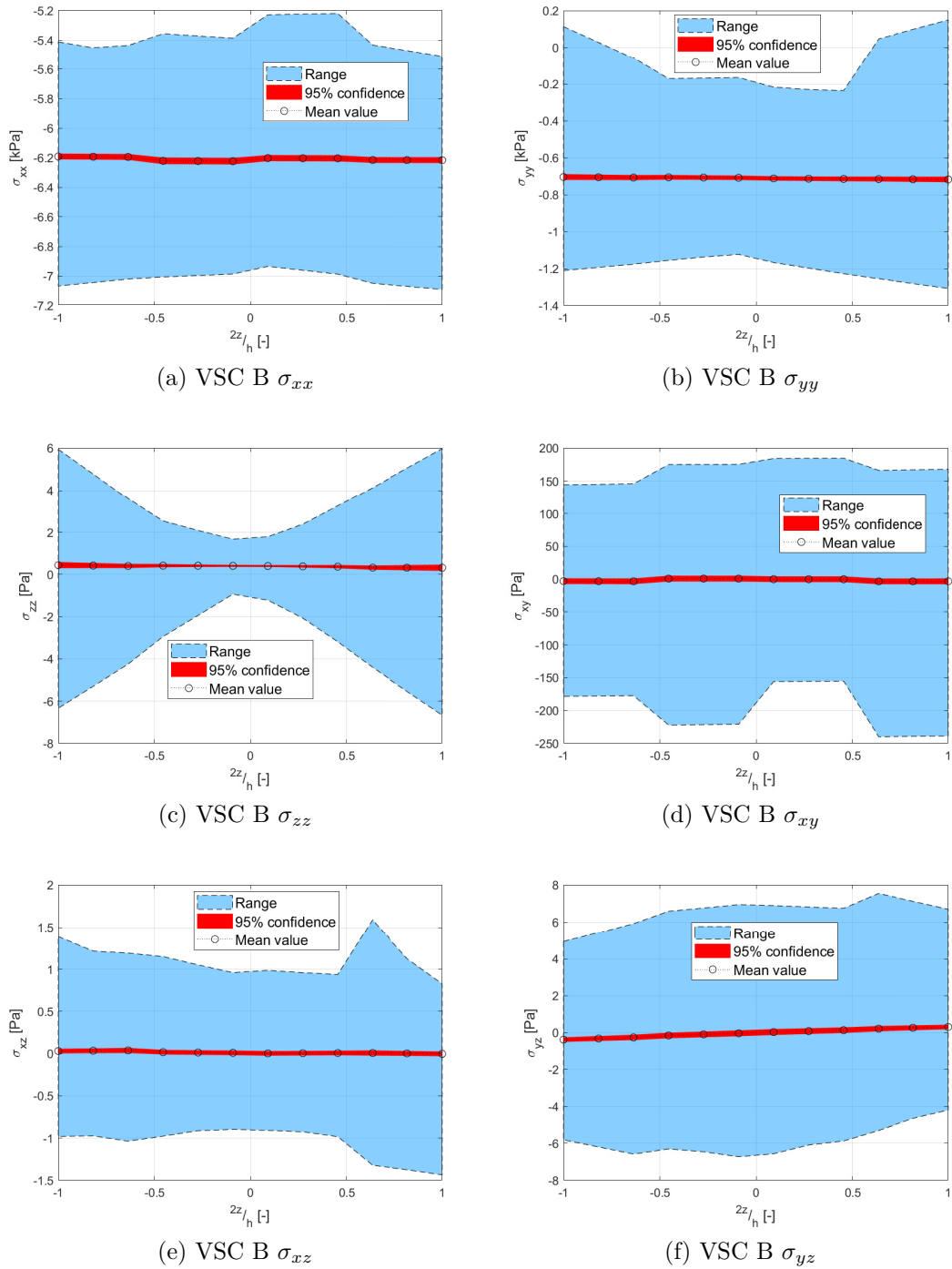


Figure 5.22: Stress tensor representation along line s for VSC B

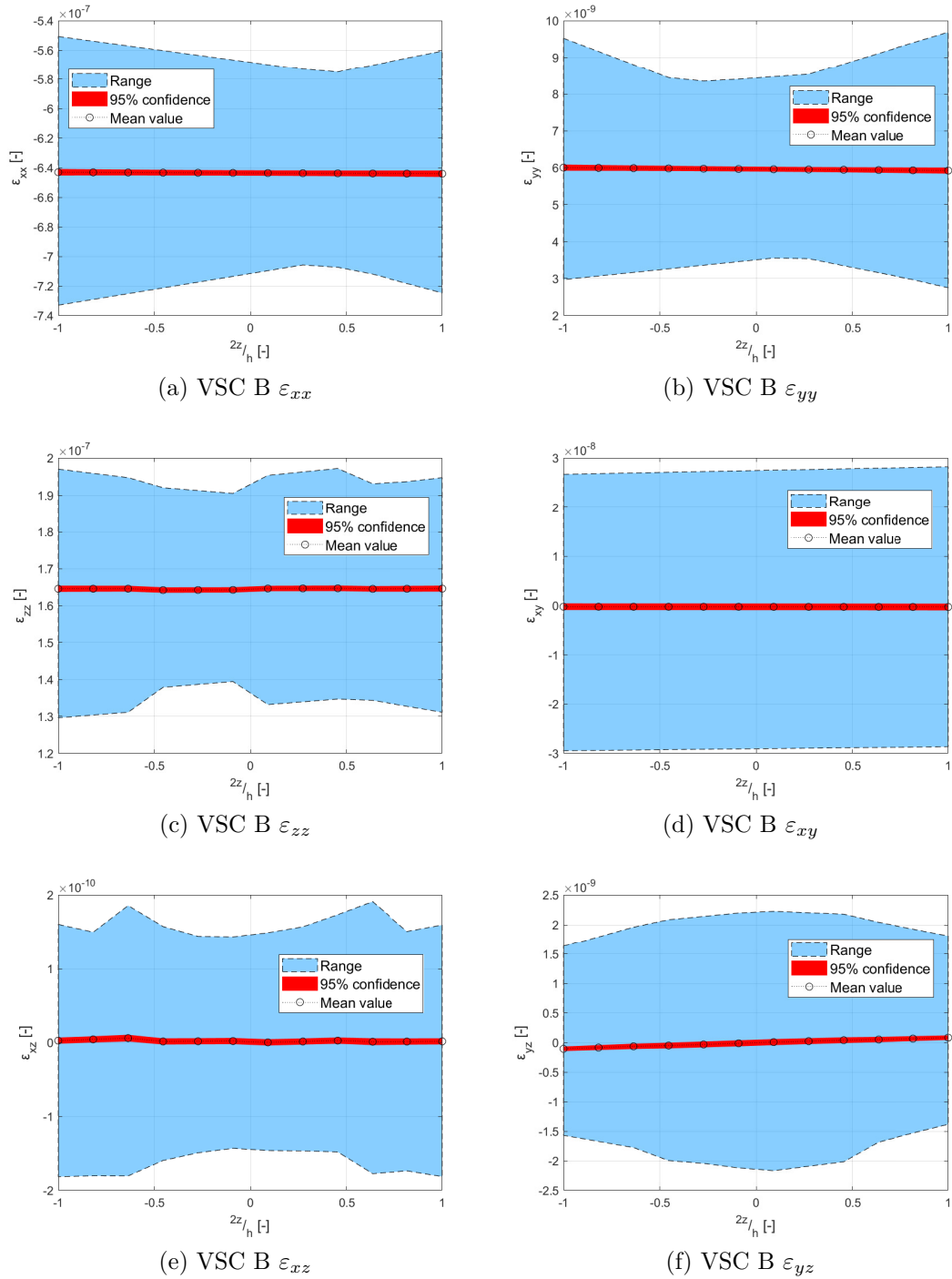


Figure 5.23: Strain tensor representation along line s for VSC B

5.3.4 Buckling critical loads

The buckling performance of the VSCs affected by uncertainty effects is here presented. From the Monte Carlo, the first six F_{cr_i} are obtained in each simulation, and statistical data is calculated from the outputs of the analysis. The mean value, standard deviation and the coefficient of variation (COV) are the statistical data computed from these Monte Carlo results. Then, histograms are employed for obtaining the F_{cr_i} graphical representations. Table 5.11 contains the statistical data referred to the results of VSC A. The histograms which describe the distribution of the loads for this VSC are shown in Figure 5.24. The results for VSC B are presented following the same procedure. Table 5.12 contains its gathered data from the Monte Carlo analysis and Figure 5.25 shows the histograms which describe the loads' distributions.

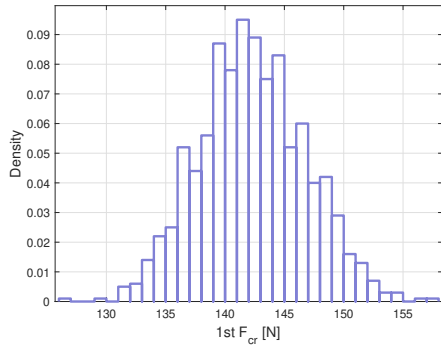
VSC A	Pristine [N]	Monte Carlo mean [N]	Standard deviation [N]	COV $\%(\frac{\sigma}{\mu} \cdot 100)$
F_{cr1}	142.2	142.3	4.5	3.2
F_{cr2}	157.1	157.4	4.8	3
F_{cr3}	214.3	215	6.7	3.1
F_{cr4}	300.5	300.8	9.2	3
F_{cr5}	353.4	354.3	11.9	3.3
F_{cr6}	403.5	404.1	12.8	3.2

Table 5.11: Monte Carlo analysis results for VSC A

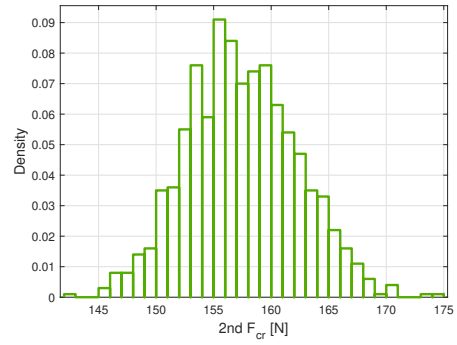
VSC B	Pristine [N]	Monte Carlo mean [N]	Standard deviation [N]	COV $(\frac{\sigma}{\mu} \cdot 100)$
F_{cr1}	25.8	25.9	0.7	2.7
F_{cr2}	47.5	47.4	1.2	2.5
F_{cr3}	59.2	59.2	1.6	2.7
F_{cr4}	78.4	78.3	1.8	2.3
F_{cr5}	107.3	107.3	2.9	2.7
F_{cr6}	127.1	127	3	2.4

Table 5.12: Monte Carlo analysis results for VSC B

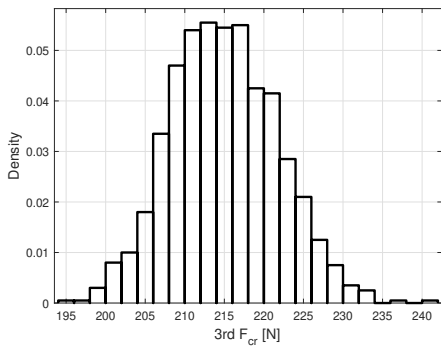
The COV values obtained for both VSCs are similar for all F_{cr_i} . This fact is due to the linearity of the buckling analysis which maintains the proportionality between the standard deviation and the mean values of the loads. Again, due to the linearity of the problem and the Gaussian nature of the stochastic fields under investigation, the F_{cr_i} show normal distributions too.



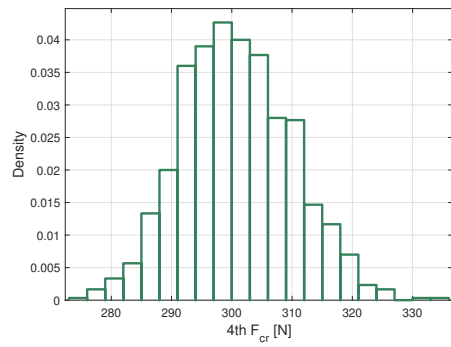
(a) VSC A F_{cr1}



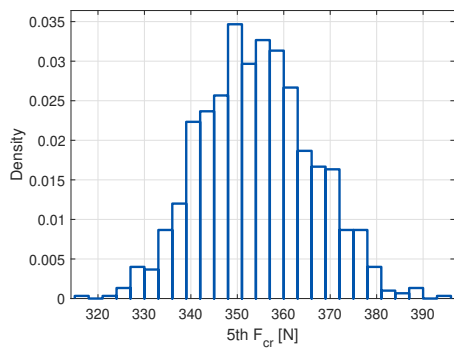
(b) VSC A F_{cr2}



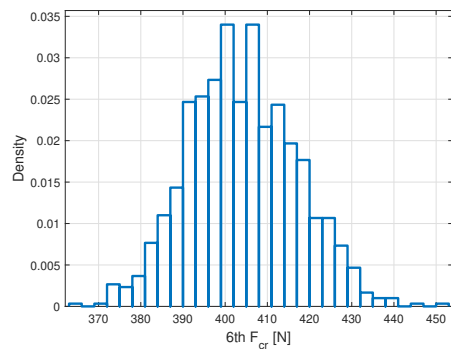
(c) VSC A F_{cr3}



(d) VSC A F_{cr4}



(e) VSC A F_{cr5}



(f) VSC A F_{cr6}

Figure 5.24: Histograms of the F_{cr} for VSC A

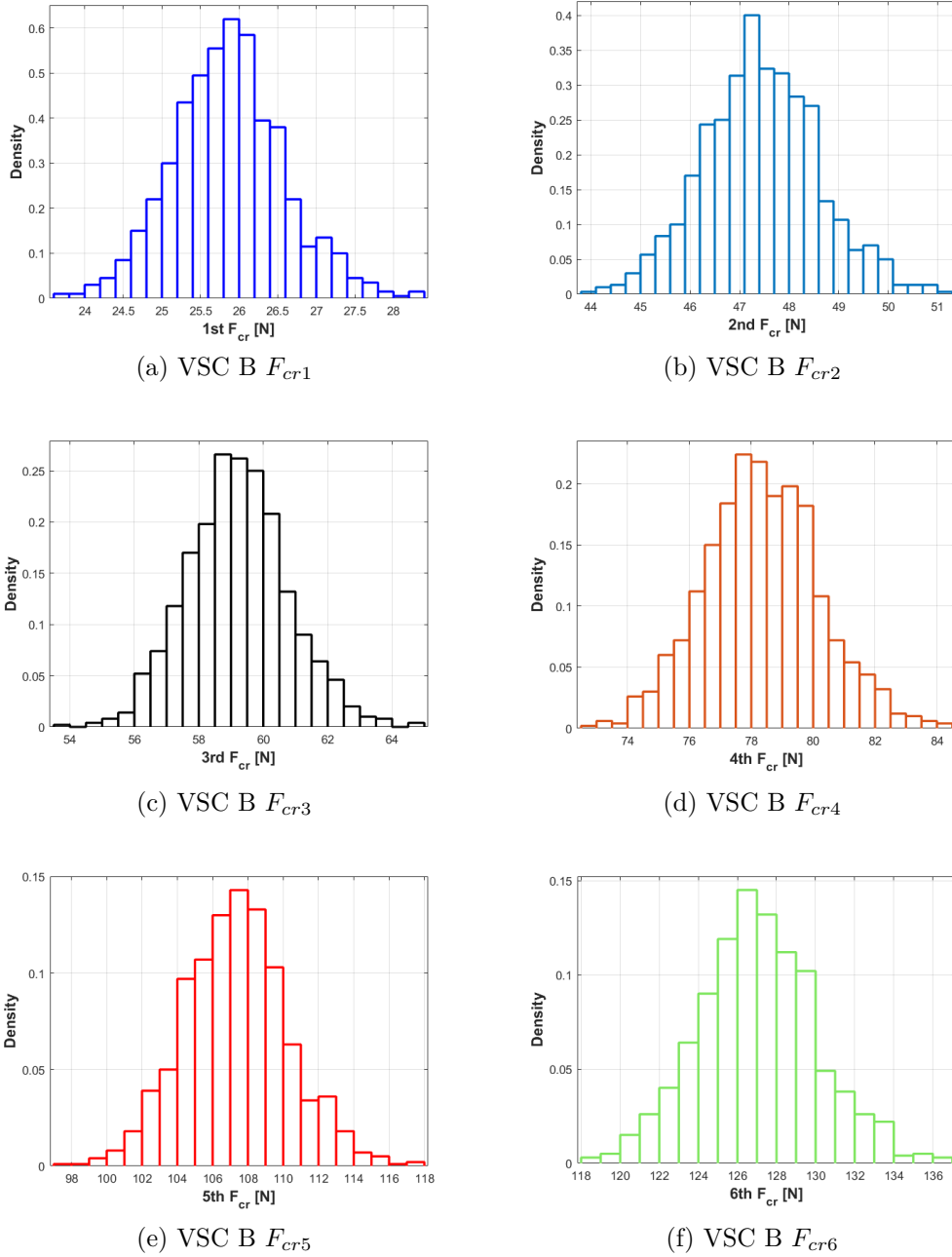


Figure 5.25: Histograms of the F_{cr} for VSC B

5.3.5 Mode classification

Once the results of the critical loads have been obtained, there is an important detail that must be analyzed. It consists of the superposition between different load distributions for VSC A, which can be observed in Figure 5.26. This event could occur due to a mode interchange between the different F_{cr_i} .

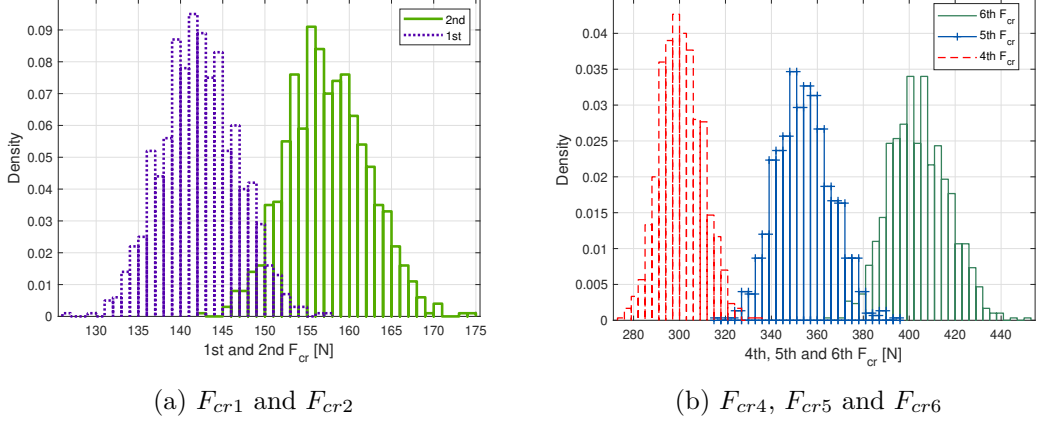


Figure 5.26: Superposing F_{cr_i} distributions for VSC A .

It is of our interest to understand if these superposing distributions correspond to the mode swapping phenomena or it is simply due to the uncertainty effect which generate wide ranges of values of F_{cr_i} that overlap with each other. To shed some light on the event, a Modal Assurance Criterion's (MAC) matrix is calculated for each simulation. MAC matrices are computed in the following way:

$$\text{MAC}_{j,k}^{(i)} = \frac{|\phi_{i,j}^T \phi_{\text{pris},k}|^2}{(\phi_{i,j}^T \phi_{i,j}) (\phi_{\text{pris},k}^T \phi_{\text{pris},k})} \quad (5.1)$$

In this expression, i is an index indicating the current Monte Carlo simulation. The other terms, $\phi_{\text{pris},k}$ and $\phi_{i,j}$ are eigenfunctions of the j and k modes which correspond respectively to the pristine structure and the one affected by uncertainty. Due to the eigenfunctions properties, the product of this operation gives information about the modes in the following way:

- If there is no mode swapping, the diagonal terms of the MAC matrix are nearly a unit (5.27a).
- If mode swapping occurs between two modes, their respective diagonal terms of the matrix become zeros and their non-diagonal terms get significant values instead (5.27b).

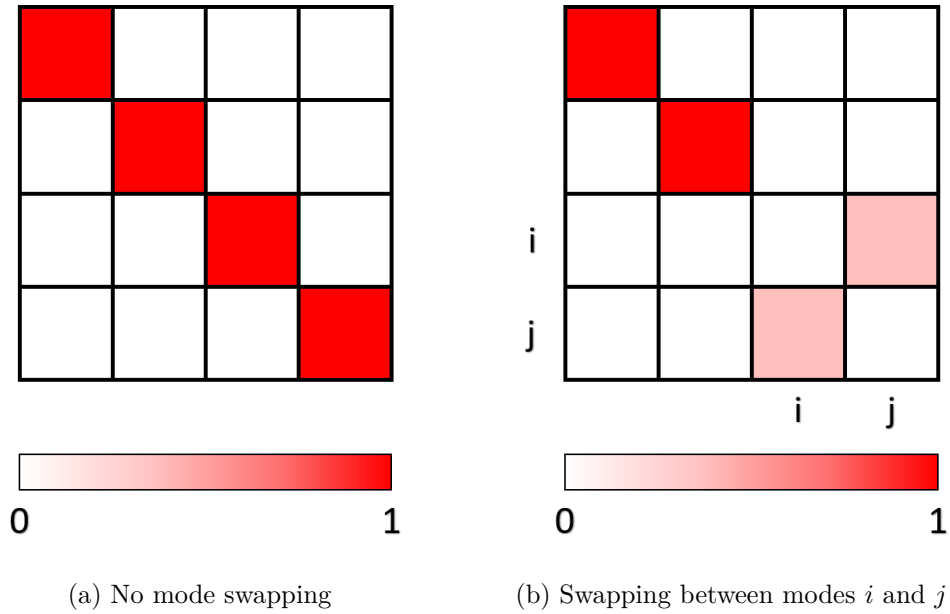


Figure 5.27: MAC matrices give information about mode swapping

More information about MAC matrices can be found in [39]. For VSC A, a MAC matrix has been computed for each simulation. The data gathered from all simulations is presented in Figure 5.28, which indicates the mean value of each MAC coefficient and its standard deviation. The mean value of the diagonal terms is approximately one for each mode. Therefore, no mode swapping is detected between any of the deformation modes of the structure.

On the other hand, VSC B does not present any superposing load distribution. However, for the sake of completion, the MAC matrix for VSC B is shown in Figure 5.29. It can be observed that the diagonal terms of its MAC matrix are nearly a unit as well. With MAC statistical data, the possibility of mode swapping is discarded.

5.3.6 Buckling Loads Correlation

In this section, the correlation between the F_{cr_i} is going to be investigated. The aim of this study is to verify if uncertainty in the FVF parameter affects the loads in the same way, increasing or decreasing all their values together at the same time, or if it may oppositely affect some of them. As an example, Figure 5.30 shows these two possible cases under investigation for VSC A F_{cr1} and F_{cr2} :

- Figure 5.30a presents the case in which all loads are affected in the same

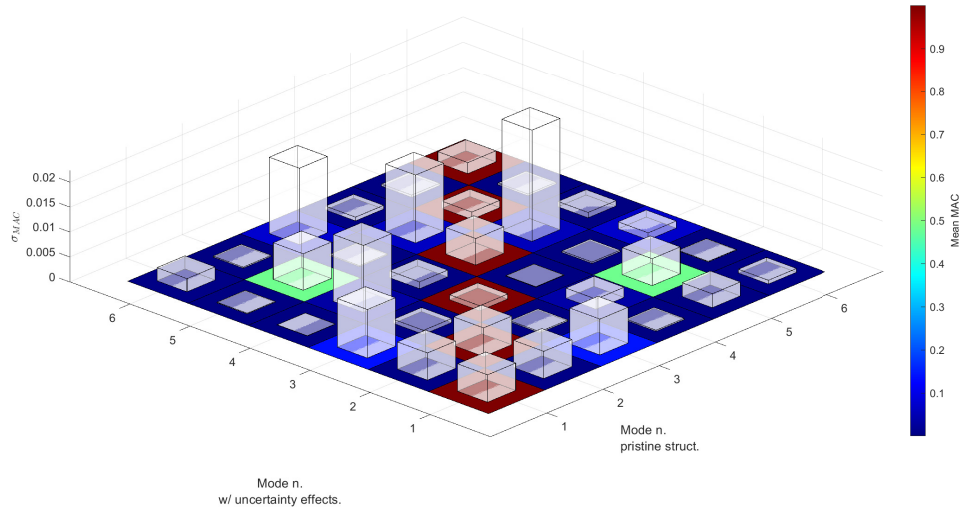


Figure 5.28: MAC matrix statistical data: mean value and standard deviation for VSC A

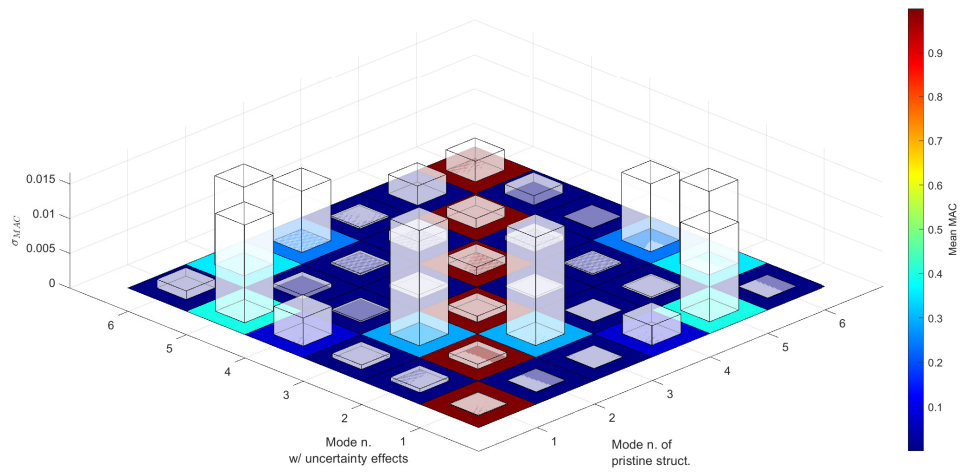


Figure 5.29: MAC matrix statistical data: mean value and standard deviation for VSC B

way. For both F_{cr_i} , the obtained values belong to the range area closer to the maximum value.

- Figure 5.30b presents the opposite case, in which the loads are affected the other way round. For F_{cr1} , the obtained value belongs to the right tail of its distribution, while the F_{cr2} value is closer to its range minimum.

In this case, a correlation study could help. The correlation coefficient, r , gives information about whether the variables tend to move in tandem or have an inverse relationship. The value of r ranges between $(-1, 1)$ and has the following meaning:

- $r > 0$ indicates that when one load increases, there is a positive increase on the other too.
- $r < 0$ indicates that when one load increases, the other one decreases.
- $r = 0$ indicates no correlation between the loads.

For each simulation, the correlation coefficient is computed for all F_{cr_i} in relation to F_{cr1} in the following way:

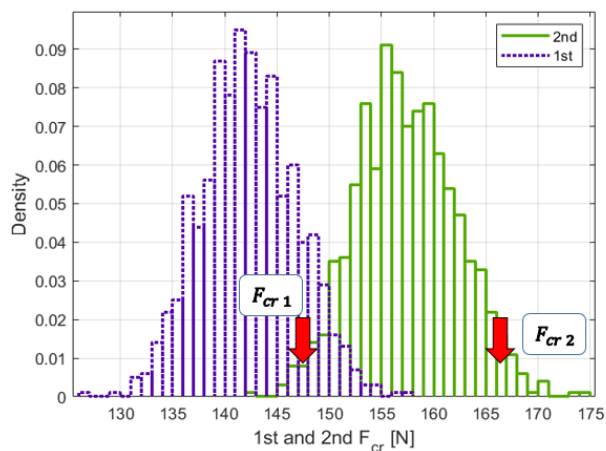
$$r_i = \frac{N (\sum F_{cr1} F_{cri}) - (\sum F_{cr1}) (\sum F_{cri})}{\sqrt{[N \sum F_{cr1}^2 - (\sum F_{cr1})^2] [N \sum F_{cri}^2 - (\sum F_{cri})^2]}} \quad (5.2)$$

where N is the number of simulations. The r -coefficients are computed for VSC A and B and are listed in Table 5.13.

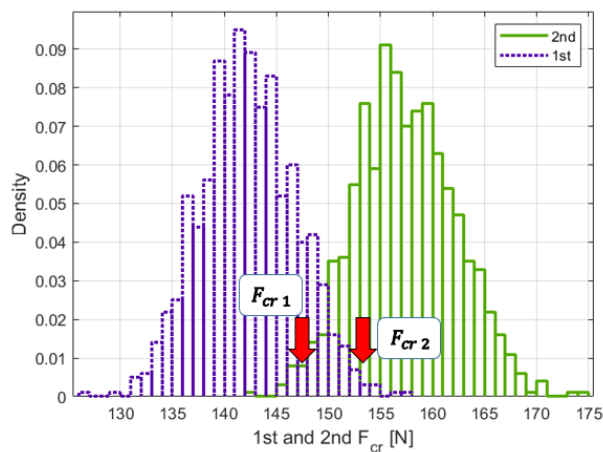
F_{cr_i} correlation with F_{cr1}	F_{cr1}	F_{cr2}	F_{cr3}	F_{cr4}	F_{cr5}	F_{cr6}
r -coefficient VSC A	1	0.9815	0.9455	0.957	0.9786	0.9641
r -coefficient VSC B	1	0.9851	0.9746	0.9757	0.9896	0.9819

Table 5.13: Correlation coefficients in relation to F_{cr1}

These correlation coefficients are positive and nearly a unit. This fact indicates that when F_{cr1} increases, the other critical loads do so and almost linearly. Therefore, when a F_{cr1} is obtained in the right side area of its distribution plot, the obtained values of the other F_{cr_i} are also close to the right tail of their respective distributions and vice-versa. It can be stated that uncertainty affects all F_{cr_i} with the same trend.



(a) F_{cr1} and F_{cr2} are affected the same way by uncertainty effects



(b) F_{cr1} and F_{cr2} are affected the opposite way by uncertainty effects

Case A	Min [N]	Max [N]
F_{cr1}	126.8	157.2
F_{cr2}	142.2	174.9

(c) F_{cr1} and F_{cr2} range of values

Figure 5.30: Uncertainty affecting F_{cr1} and F_{cr2} in the same way (a) and in the opposite way (b). The range limits for both loads are listed in (c)

5.3.7 Polynomial chaos expansion

PCE is employed for uncertainty quantification in the study of Monte Carlo F_{cr} distributions. The PCE models are obtained on a basis of Hermite polynomials and their output is here represented with a normal probability plot. PCE data for the first and second degree's models is here presented. The outputs of the surrogate model for VSC A are listed in Table 5.14. Then, the same data for VSC B is shown in Table 5.15.

VSC A	Monte Carlo		1st degree PCE		2nd degree PCE	
	Mean [N]	COV ($\frac{\sigma}{\mu} \cdot 100$)	Mean [N]	COV ($\frac{\sigma}{\mu} \cdot 100$)	Mean [N]	COV ($\frac{\sigma}{\mu} \cdot 100$)
F_{cr1}	142.3	3.2	142.1	3.2	142.1	3.1
F_{cr2}	157.4	3	157.2	3.1	157.2	3
F_{cr3}	215	3.1	214.6	3.1	214.6	3.1
F_{cr4}	300.8	3	300.3	3.1	300.3	3.1
F_{cr5}	354.3	3.3	353.7	3.4	353.7	3.4
F_{cr6}	404.1	3.2	403.4	3.2	403.4	3.2

Table 5.14: PCE statistical data for VSC A

VSC B	Monte Carlo		PCE mean (1st degree)		PCE mean (2nd degree)	
	Mean [N]	COV ($\frac{\sigma}{\mu} \cdot 100$)	Mean [N]	COV ($\frac{\sigma}{\mu} \cdot 100$)	Mean [N]	COV ($\frac{\sigma}{\mu} \cdot 100$)
F_{cr1}	25.9	2.7	25.9	2.8	25.9	2.8
F_{cr2}	47.4	2.5	47.5	2.5	47.5	2.5
F_{cr3}	59.2	2.7	59.2	2.7	59.2	2.7
F_{cr4}	78.3	2.3	78.4	2.4	78.4	2.4
F_{cr5}	107.3	2.7	107.4	2.8	107.4	2.8
F_{cr6}	127.1	2.4	127.2	2.4	127.2	2.4

Table 5.15: PCE statistical data for VSC B

The PCE surrogate models show a great ability to capture the sensitivity of F_{cr_i} to the FVF variation and reproduce the same results as the Monte Carlo analysis. It can be observed that the polynomial degree of the PCE expansion has no significant effect on the surrogate's output. Figure 5.31 contains the plots of the Monte Carlo output distributions with the normal probability plot obtained by PCE for F_{cr1} .

PCE has shown to be a reliable surrogate model for our study. It can be very advantageous to employ it in order to save time in the analysis. For this purpose, it is going to be investigated how many Monte Carlo simulations are needed to have enough information to describe the PCE. This study is only going to be presented

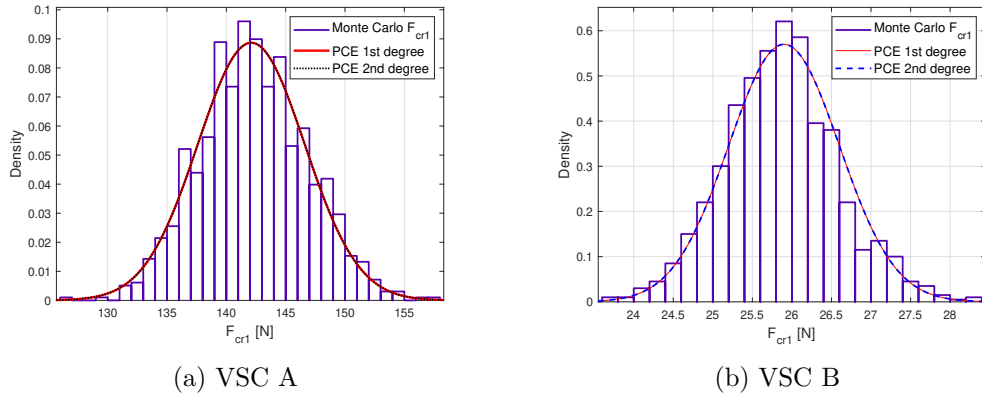
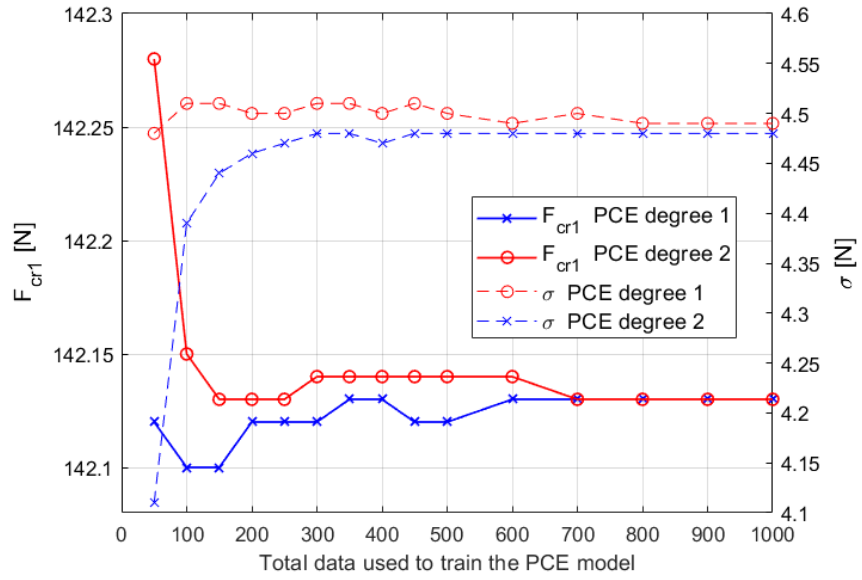


Figure 5.31: F_{cr1} distributions obtained from the Monte Carlo analysis and the PCE models

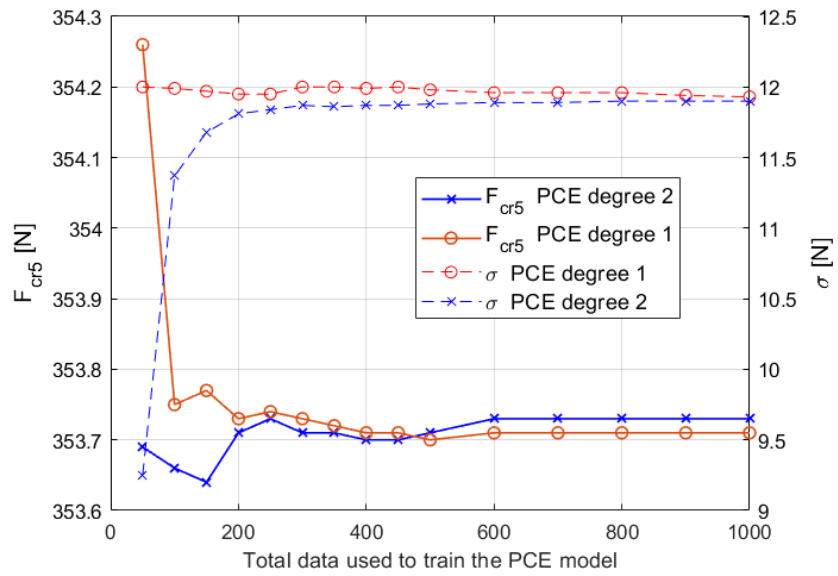
for one of the VSCs. Figure 5.32 presents the convergence of the PCE data in relation to the number of simulations employed to train the surrogate model for VSC A. Only the convergence of F_{cr1} and F_{cr5} are investigated as these are the loads with larger COV values. The graphs display the convergence of the mean value and the standard deviation which are obtained with the PCE models for first and second-degree expansions. It is important to notice the two axes employed in each graph and the difference of scales from one graph to another.

As it can be observed, after a certain number of Monte Carlo simulations, the PCE is already capable to describe the model and to compute the mean and standard deviation of the loads. Employing only 300 Monte Carlo simulations, it is possible to get accurate results, saving the computational time of 700 Monte Carlo simulations. Table 5.16 shows the time required to obtain the results through both ways. Again, as time is dependent on the employed CPU, it is presented in a qualitative way, dividing all values by the total time needed for the 1000 simulations, t_{all} . Therefore, PCE allows one to save 70% of the time needed to compute all the simulations. This is a significant difference, which definitively makes PCE a very interesting option for the sensitivity study. Finally, Figure 5.33 presents a graphical representation of the elapsed time if:

1. All Monte Carlo simulations are performed and no PCE is employed.
2. Only the Monte Carlo simulations needed by the PCE are performed and the PCE model is responsible for calculating the load distributions.



(a) F_{cr1} PCE convergence



(b) F_{cr5} PCE convergence

Figure 5.32: PCE convergence analysis

	Elapsed time t_i/t_{all} [-]
1000 Monte Carlo simulations	1
300 Monte Carlo simulations	0.3
PCE computational time	0.000003

Table 5.16: Qualitative computational times

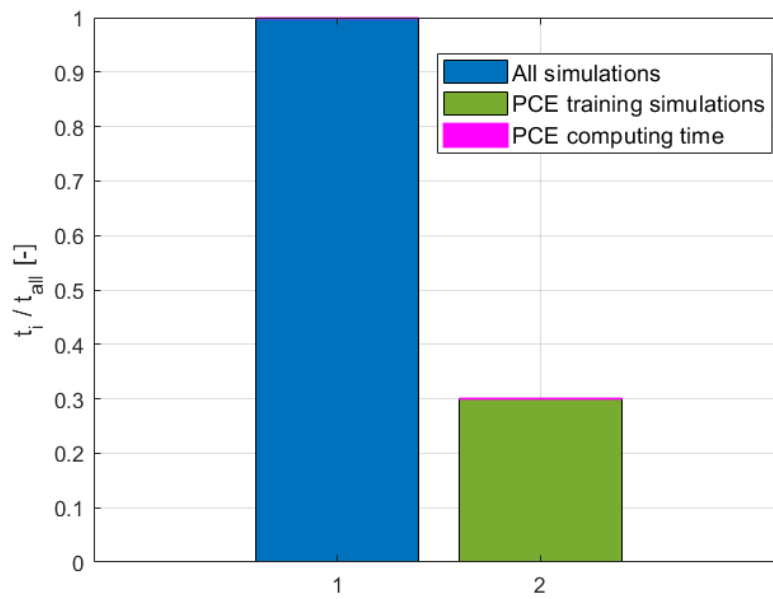


Figure 5.33: Time employed to perform all Monte Carlo simulations (1) vs total time for performing 300 simulations and for the PCE calculations (2)

Chapter 6

Conclusions

The aim of this study was to perform multi-scale sensitivity analysis of Variable Stiffness Composites (VSCs). In this work, the mechanical performance at a macro-scale level of two VSCs subjected to linearized buckling analyses is investigated when uncertainty effects introduce variability into the fiber volume fraction (FVF) parameter at the micro-scale level.

For this purpose, finite element (FE) models altogether with Carrera Unified Formulation (CUF) based theories were employed as the instrument of analysis. All laminates were described independently with a layer-wise (LW) approach, which allowed the introduction of uncertainty in each layer separately. Uncertainty was modeled as a stochastic field expanded within the plies through Karhunen-Loève expansion (KLE), and Latin Hypercube Sampling (LHS) was implemented to ensure a proper FVF field generation. The meso-scale material properties assigned to the FE mesh elements were obtained applying the mechanics of the structure genome (MSG). Solving the Unit Cell (UC) problem, which depends on the FVF parameter, provides the effective material properties of the homogenized UC.

The mechanical behavior of the VSCs models and the procedures employed in the analysis were properly verified by comparison with literature results and data obtained with commercial software Abaqus.

The first results were obtained for the pristine structure and shown the stress and strain fields obtained from the static solution, at a macro-scale level, through the thickness of the laminated plate. A micro-scale field recovery process was presented for a cell located in a point of the structure. Later, the buckling analysis results were shown, again for the defect-free model.

Then, uncertainty effects were introduced in the model, and the sensitivity analysis was performed by means of a Monte Carlo analysis. Among the obtained results of this analysis, one can find the stress and strain fields from the static solution at the macro-scale level. These are presented with a 95% confidence interval which indicates the most probable values to be obtained. The main focus relies on

the buckling critical loads obtained from the linearized buckling analysis. The loads present Gaussian distributions and the mean value and standard deviation are reported for the first six critical loads. coefficient of variation (COV) parameter is employed as a measure of the data dispersion due to the variation of the micro-scale parameter.

The buckling critical loads and their respective deformation modes were provided, and a possible mode swapping phenomena was studied and discarded applying Modal Assurance Criterion (MAC). Later, Polynomial Chaos Expansion (PCE) was applied in order to generate surrogate models which provide a reliable representation of the behavior of the VSCs.

At the conclusion of the multi-scale sensitivity analysis, it can be affirmed that:

- The design of the composites' fiber orientation have a very significant effect on the mechanical performance of VSCs.
- The generation of the stochastic fields based on KLE and applying LHS have turned out to be an adequate procedure to model uncertainty.
- The utilization of LW models is compulsory in order to be able to model the defects for each layer independently.
- Uncertainty effects in the FVF parameter affects all the critical buckling loads in the same way. They are strongly correlated, almost in a linear way, with r correlation coefficients close to +1.
- Critical buckling loads are sensitive to the FVF variation in the following way: normally, the stochastic FVF fields have an average COV parameter of around 6-7% and the load distributions barely reach a COV of 2-3%.
- The application of PCE can save up to 70% of the Monte Carlo simulations needed for the VSCs studied in this work, leading to a less time-consuming analysis.

Finally, as a continuation of this work, it is proposed to model more defects which can be introduced in the analysis as, for example, void formation. Other possible further work will consist of analysing a combination of uncertainty with other defects already modeled in the literature for VSC plates. In the field of multi-scale sensitivity, further analysis could proceed with the study of uncertainty effects in the micro-scale fields which can be obtained through the recovery process of the UC-problem.

Bibliography

- [1] S. Prabhakar. «A Methodology for Finite Element Analysis of Curvilinear Fiber Laminates with Defects, Fabricated by Automated Fiber Placement Technique». PhD thesis. McGill University, Montreal, Dec. 2011 (cit. on pp. 1, 2, 5).
- [2] F. Heinecke and C. Willberg. «Manufacturing-Induced Imperfections in Composite Parts Manufactured via Automated Fiber Placement». In: *Journal of Composites Science* 3.2 (2019). ISSN: 2504-477X. DOI: 10.3390/jcs3020056. URL: <https://www.mdpi.com/2504-477X/3/2/56> (cit. on pp. 1–4).
- [3] A. Blom, C.s Lopes, P. Kromwijk, Z. Gurdal, and P. Camanho. «A Theoretical Model to Study the Influence of Tow-drop Areas on the Stiffness and Strength of Variable-stiffness Laminates». In: *Journal of Composite Materials - J COMPOS MATER* 43 (Jan. 2009), pp. 403–425. DOI: 10.1177/0021998308097675 (cit. on pp. 1, 5, 6).
- [4] M. Arian Nik, K. Fayazbakhsh, D. Pasini, and L. Lessard. «Optimization of variable stiffness composites with embedded defects induced by Automated Fiber Placement». In: *Composite Structures* 107 (2014), pp. 160–166. ISSN: 0263-8223. DOI: <https://doi.org/10.1016/j.compstruct.2013.07.059>. URL: <http://www.sciencedirect.com/science/article/pii/S0263822313003978> (cit. on pp. 5–7).
- [5] A.Pagani and A.R.Sanchez-Majano. «Influence of fiber misalignments on buckling performance of variable stiffness composites using layerwise models and random fields». In: *Mechanics of Advanced Materials and Structures* (2020), pp. 1–16. DOI: 10.1080/15376494.2020.1771485 (cit. on pp. 5–7, 9, 21).
- [6] K. Fayazbakhsh, M. Arian Nik, D. Pasini, and L. Lessard. «Defect layer method to capture effect of gaps and overlaps in variable stiffness laminates made by Automated Fiber Placement». In: *Composite Structures* 97 (2013), pp. 245–251. ISSN: 0263-8223. DOI: <https://doi.org/10.1016/j.compstruct.2012.10.031>. URL: <http://www.sciencedirect.com/science/article/pii/S0263822312005272> (cit. on pp. 5, 7).

- [7] X. Zhou, X. Ruan, and P.D. Gosling. «Robust design optimization of variable angle tow composite plates for maximum buckling load in the presence of uncertainties». In: *Composite Structures* 223 (2019), p. 110985. ISSN: 0263-8223. DOI: <https://doi.org/10.1016/j.compstruct.2019.110985>. URL: <http://www.sciencedirect.com/science/article/pii/S0263822319305306> (cit. on pp. 6, 8, 9).
- [8] A. Noevere and C. Collier. «Mapping Manufacturing Data for Stress Analysis of Automated Fiber Placement Structures». In: *2018 AIAA/ASCE/AHS/ASC Structures, Structural Dynamics, and Materials Conference*. DOI: 10.2514/6.2018-0228. eprint: <https://arc.aiaa.org/doi/pdf/10.2514/6.2018-0228>. URL: <https://arc.aiaa.org/doi/abs/10.2514/6.2018-0228> (cit. on p. 6).
- [9] D.S. Cairns, L.B. Ilcewicz, and T. Walker. «Response of Automated Tow Placed Laminates to Stress Concentrations». In: *Third NASA Advanced Composites Technology Conference (ACT)*. Long Beach, CA, USA, June 1993, pp. 1–15 (cit. on p. 6).
- [10] O. Falcó, C.S. Lopes, F. Naya, F. Sket, P. Maimí, and J.A. Mayugo. «Modelling and simulation of tow-drop effects arising from the manufacturing of steered-fibre composites». In: *Composites Part A: Applied Science and Manufacturing* 93 (2017), pp. 59–71. ISSN: 1359-835X. DOI: <https://doi.org/10.1016/j.compositesa.2016.11.015>. URL: <http://www.sciencedirect.com/science/article/pii/S1359835X16303967> (cit. on p. 7).
- [11] A. Pagani and A.R. Sanchez-Majano. «Stochastic stress analysis and failure onset of variable angle tow laminates affected by spatial fibre variations». In: *Composites Part C: Open Access* 4 (2021), p. 100091. ISSN: 2666-6820. DOI: <https://doi.org/10.1016/j.jcomc.2020.100091>. URL: <http://www.sciencedirect.com/science/article/pii/S2666682020300918> (cit. on pp. 7, 18).
- [12] C. T. Herakovich. «Mechanics of composites: A historical review». In: *Mechanics Research Communications* 41 (2012), pp. 1–20. ISSN: 0093-6413. DOI: <https://doi.org/10.1016/j.mechrescom.2012.01.006>. URL: <https://www.sciencedirect.com/science/article/pii/S0093641312000080> (cit. on pp. 7, 8).
- [13] Z. Hashin and W.B. Rosen. «The Elastic Moduli of Fibre-Reinforced Materials». In: *Journal of Applied Mechanics* 31 (1964), pp. 223–232. URL: <http://dx.doi.org/10.1115/1.3629590> (cit. on p. 7).
- [14] J. Aboudy. «Micromechanical Analysis of Composites by the Method of Cells». In: *Applied mechanics reviews* 42 (1989), pp. 193–221. ISSN: 0003-6900. URL: <https://doi.org/10.1115/1.3152428> (cit. on p. 8).

- [15] M. Paley and J. Aboudi. «Micromechanical analysis of composites by the generalized cells model». In: *Mechanics of Materials* 14.2 (1992), pp. 127–139. ISSN: 0167-6636. DOI: [https://doi.org/10.1016/0167-6636\(92\)90010-B](https://doi.org/10.1016/0167-6636(92)90010-B). URL: <https://www.sciencedirect.com/science/article/pii/S016766369290010B> (cit. on p. 8).
- [16] J. Aboudi, M.-J. Pindera, Mem. ASME, and S. M. Arnold. «Linear Thermoelastic Higher-Order Theory for Periodic Multiphase Materials». In: *Applied mechanics reviews* 68.5 (2001), pp. 697–707. ISSN: 0021-8936. DOI: <https://doi.org/10.1115/1.1381005> (cit. on p. 8).
- [17] T. O. Williams. «A three-dimensional, higher-order, elasticity-based micromechanics model». In: *International Journal of Solids and Structures* 42.3 (2005), pp. 971–1007. ISSN: 0020-7683. DOI: <https://doi.org/10.1016/j.ijstr.2004.06.056>. URL: <https://www.sciencedirect.com/science/article/pii/S0020768304003749> (cit. on p. 8).
- [18] C.T. Sun and R.S. Vaidya. «Prediction of composite properties from a representative volume element». In: *Composites Science and Technology* 56.2 (1996), pp. 171–179. ISSN: 0266-3538. DOI: [https://doi.org/10.1016/0266-3538\(95\)00141-7](https://doi.org/10.1016/0266-3538(95)00141-7). URL: <https://www.sciencedirect.com/science/article/pii/S0266353895001417> (cit. on p. 8).
- [19] T. A. M. Guimarães, H. L. Silva, D. A. Rade, and C. E. S. Cesnik. «Aeroelastic Stability of Conventional and Tow-Steered Composite Plates Under Stochastic Fiber Volume». In: *AIAA Journal* 58.6 (2020), pp. 2748–2759. DOI: 10.2514/1.J059106. URL: <https://doi.org/10.2514/1.J059106> (cit. on pp. 8, 9, 36, 37, 68).
- [20] C. Scarth, S. Adhikari, P. Higino Cabral, G. H.C. Silva, and A. Pereira do Prado. «Random field simulation over curved surfaces: Applications to computational structural mechanics». In: *Computer Methods in Applied Mechanics and Engineering* 345 (2019), pp. 283–301. ISSN: 0045-7825. DOI: <https://doi.org/10.1016/j.cma.2018.10.026>. URL: <http://www.sciencedirect.com/science/article/pii/S0045782518305309> (cit. on p. 9).
- [21] X. Zhou and P.D. Gosling. «Towards an understanding of variations in the buckling of tailored variable angle tow composite plates». In: *Composite Structures* 203 (2018), pp. 797–809. ISSN: 0263-8223. DOI: <https://doi.org/10.1016/j.compstruct.2018.07.061>. URL: <http://www.sciencedirect.com/science/article/pii/S0263822318307001> (cit. on p. 9).

- [22] E. Carrera, M. Cinefra, M. Petrolo, and E. Zappino. *Finite Element Analysis of Structures through Unified Formulation*. The Atrium, Southern Gate, Chichester, West Sussex, PO198SQ, United Kingdom: John Wiley & Sons Ltd, 2014 (cit. on pp. 11, 12, 18).
- [23] E. Carrera, M. Filippi, and E. Zappino. «Laminated beam analysis by polynomial, trigonometric, exponential and zig-zag theories». In: *European Journal of Mechanics - A/Solids* 41 (2013), pp. 58–69. ISSN: 0997-7538. DOI: <https://doi.org/10.1016/j.euromechsol.2013.02.006>. URL: <http://www.sciencedirect.com/science/article/pii/S0997753813000272> (cit. on p. 11).
- [24] A. Pagani, A.G. de Miguel, M. Petrolo, and E. Carrera. «Analysis of laminated beams via Unified Formulation and Legendre polynomial expansions». In: *Composite Structures* 156 (2016). 70th Anniversary of Professor J. N. Reddy, pp. 78–92. ISSN: 0263-8223. DOI: <https://doi.org/10.1016/j.compstruct.2016.01.095>. URL: <http://www.sciencedirect.com/science/article/pii/S0263822316001185> (cit. on pp. 12, 14).
- [25] A. García de Miguel. «Hierarchical component-wise models for enhanced stress analysis and health monitoring of composites structures». PhD thesis. Politecnico di Torino, Feb. 2019 (cit. on pp. 13, 14, 26, 31, 33).
- [26] J.N. Reddy. *Mechanics of Laminated Composite Plates and Shells: Theory and Analysis*. Boca Raton, Florida, USA: CRC Press, 2004 (cit. on p. 17).
- [27] E. Carrera and M. Filippi. «Variable Kinematic One-Dimensional Finite Elements for the Analysis of Rotors Made of Composite Materials». In: *Journal of Engineering for Gas Turbines and Power* 136 (2014). DOI: 10.1115/1.4027192 (cit. on p. 17).
- [28] L. Demasi, G. Biagini, F. Vannucci, E. Santarpia, and R. Cavallaro. «Equivalent Single Layer, Zig-Zag, and Layer Wise theories for variable angle tow composites based on the Generalized Unified Formulation». In: *Composite Structures* 177 (2017), pp. 54–79. ISSN: 0263-8223. DOI: <https://doi.org/10.1016/j.compstruct.2017.06.033>. URL: <https://www.sciencedirect.com/science/article/pii/S0263822317314356> (cit. on p. 18).
- [29] A. Viglietti, E. Zappino, and E. Carrera. «Analysis of variable angle tow composites structures using variable kinematic models». In: *Composites Part B: Engineering* 171 (2019), pp. 272–283. ISSN: 1359-8368. DOI: <https://doi.org/10.1016/j.compositesb.2019.03.072>. URL: <https://www.sciencedirect.com/science/article/pii/S1359836818318316> (cit. on p. 18).

- [30] A. Viglietti, E. Zappino, and E. Carrera. «Free vibration analysis of variable angle-tow composite wing structures». In: *Aerospace Science and Technology* 92 (2019), pp. 114–125. ISSN: 1270-9638. DOI: <https://doi.org/10.1016/j.ast.2019.05.068>. URL: <https://www.sciencedirect.com/science/article/pii/S1270963819304730> (cit. on p. 18).
- [31] B. Wu, A. Pagani, W. Q. Chen, and E. Carrera. «Geometrically nonlinear refined shell theories by Carrera Unified Formulation». In: *Mechanics of Advanced Materials and Structures* 0.0 (2019), pp. 1–21. DOI: 10.1080/15376494.2019.1702237. URL: <https://doi.org/10.1080/15376494.2019.1702237> (cit. on p. 22).
- [32] A. G. de Miguel, A. Pagani, W. Yu, and E. Carrera. «Micromechanics modeling of unit cells using CUF beam models and the Mechanics of Structure Genome». In: *32nd Technical Conference of the American Society for Composites (ASC)*. Purdue University, West Lafayette, Indiana, USA, Oct. 2017. URL: <http://hdl.handle.net/11583/2694008> (cit. on pp. 33, 45, 46).
- [33] P.D. Spanos and B.A. Zeldin. «Monte Carlo treatment of random fields: a broad perspective». In: *Applied Mechanics Reviews* 51.3 (1998), pp. 219–237. DOI: 10.1115/1.3098999 (cit. on p. 36).
- [34] R.G. Ghanem and P.D. Spanos. «Stochastic Finite Elements: A Spectral Approach.» In: 1991, pp. 1–214. DOI: 10.1007/978-1-4612-3094-6 (cit. on p. 38).
- [35] G. Giunta. «Deterministic and Stochastic Hierarchical Analysis of Failure and Vibration of Composite Plates and Shells». PhD thesis. Politecnico di Torino, 2007 (cit. on p. 39).
- [36] T. Crestaux, O. Le Maître, and J. Martinez. «Polynomial chaos expansion for sensitivity analysis». In: *Reliability Engineering and System Safety* 94.7 (2009), pp. 1161–1172. ISSN: 0951-8320. DOI: <https://doi.org/10.1016/j.res.2008.10.008> (cit. on pp. 42, 43).
- [37] S. Marelli, N. Lüthena, and B. Sudret. *UQlab user manual polynomial chaos expansions*. UQlab (cit. on p. 43).
- [38] *MUL2-UC: Micromechanics code: beam modeling of periodically heterogeneous composites*. A.G. de Miguel - MUL2. 2017 (cit. on p. 45).
- [39] M. Pastor, M. Binda, and T. Harčarik. «Modal Assurance Criterion». In: *Procedia Engineering* 48 (2012). Modelling of Mechanical and Mechatronics Systems, pp. 543–548. ISSN: 1877-7058. DOI: <https://doi.org/10.1016/j.proeng.2012.09.551>. URL: <https://www.sciencedirect.com/science/article/pii/S1877705812046140> (cit. on p. 78).